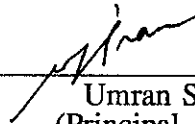


**MODELING OF VERY LOW FREQUENCY WAVE
PROPAGATION AND SCATTERING WITHIN THE
EARTH-IONOSPHERE WAVEGUIDE IN THE PRESENCE
OF LOWER IONOSPHERIC DISTURBANCES**

By
William LeRoy Poulsen
November 1991

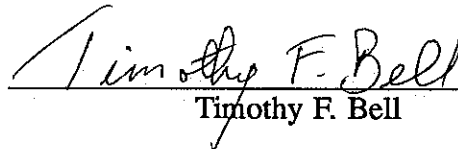
© Copyright 1991 by William LeRoy Poulsen
All Rights Reserved

I certify that I have read this thesis and that in my opinion it is fully adequate, in scope and in quality, as a dissertation for the degree of Doctor of Philosophy.



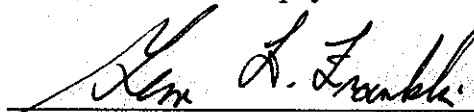
Umran S. Inan
(Principal Advisor)

I certify that I have read this thesis and that in my opinion it is fully adequate, in scope and in quality, as a dissertation for the degree of Doctor of Philosophy.



Timothy F. Bell

I certify that I have read this thesis and that in my opinion it is fully adequate, in scope and in quality, as a dissertation for the degree of Doctor of Philosophy.



Gene F. Franklin

Approved for the University Committee on Graduate Studies:

Abstract

A method has been developed for three-dimensional modeling of the effects of localized disturbances in the lower ionosphere on VLF waves propagating in the Earth-ionosphere waveguide. These disturbances include those produced by energetic electron precipitation from the magnetosphere induced by lightning. The model has been used to investigate the effects of various geophysical parameters on both the propagation properties of the wave energy within the waveguide and on the scattering properties of the disturbance. The model has also been used to examine the overall effects of typical ionospheric disturbances, of finite extent and occurring in the region between the transmitter and receiver, on the amplitude and phase of VLF signals. Results of the model indicate that the field strength pattern of a VLF wave propagating along the Earth-ionosphere waveguide can be strongly affected by changes in the ambient ionosphere and differences in the surface conductivity of the Earth. The model also shows that the signal scattering ability of the type of disturbance modeled is generally insensitive to differences in the conductivity of the ground underneath it; however, the scattering ability of the disturbance is very sensitive to differences in the altitude profile of electron density within the disturbed region. Analysis shows that for typical disturbances, most of the wave energy is scattered into a narrow ($\pm 20^\circ$) angular range about the forward scattering direction. This result implies that for typical path lengths, the effects of disturbances located at transverse distances > 200 km from the propagation path can generally be neglected. Using typical values of geophysical parameters, predictions of the model are shown to be consistent with experimental data on subionospheric VLF wave amplitude and phase changes that occur in response to transient disturbances in the lower ionosphere caused by electron precipitation which is induced by lightning discharges.

Acknowledgements

As I conclude my work towards a Ph.D. with the completion of this dissertation, I would like to thank my advisor Professor Umran Inan and my associate advisor Dr. Tim Bell for all the advice, help, counsel, and instruction that I have received throughout the many years I was at Stanford. Umran's encouragement and unflagging enthusiasm for the research at hand has been an example to me, and Tim's insight into the physics behind the most complex of equations was as helpful as were his quiet comments of encouragement during some of those late evenings spent in Durand. I would also like to express my appreciation to Professor Gene F. Franklin for chairing my oral defense committee and for cheerfully reading and commenting on this dissertation despite his very busy schedule.

I also appreciate the many educational conversations I have had with Professor Helliwell, Vikas Sonwalkar, and especially Don Carpenter; the assistance of Jerry Yarbrough even in the face of disintegrating tapes; the practical education and philosophy from Bill Trabucco; and the helpfulness of Kim Fletcher and Jenny Xu in matters both mundane and stressful.

I have also benefitted from my association with the truly diverse and "multicultural" group of fellow students that Umran and Professor Helliwell have somehow managed to bring into the VLF group. The various conversations I have had on topics both related to our research and about almost every other issue in today's world have been what I enjoyed most about working with this group. My thanks go to Hoc Ngo, Tom Wolf, Dave Shafer, Luis Sa, Tom Mielke, Juan Rodriguez, Jane Oh, Wai-Yeung Yip, Chris Elkins, Jasna Djurovic, Chris Regan, Sean Lev-Tov, Noam Eisen, Yuri Taranenko, and

Sasha Draganov. In particular, I would like to thank Bill Burgess, my officemate for all these many years. I think we must have discussed everything.

I would also like to mention and thank Tony Fraser-Smith for his wit and encouragement and listening ear. To him I'd like to say, "¡Hola! ¿Qué tal?" one last time.

Thanks also go to Kathy Smead and Brenda Hansen who have not only willingly listened but actively sought to elicit any "dirt" from me over the years, and many thanks for the moral support, encouragement, and laughter of many other friends too numerous to mention, both student and non-student, living both near and far, with whom I have had the privilege of associating and whose friendship and fellowship I continue to enjoy.

I would be remiss if I failed to acknowledge all my wonderful roommates, and in particular, all the many denizens, great and small, who have had the privilege of living for any length of time at 19-Y Manzanita Park and made this segment of my life one of the most memorable.

Finally, I would like to thank a former denizen and roommate Dave Cannon, who put up with living in a trailer for so many years and who helped create the better figures in this dissertation; my brother Kenny and my sisters Nancy, Judy, Doris, and Tammy, who pestered me and encouraged me nearly my entire life; another denizen and former roommate(s) John and Becky (and Ben) Jackson who have been my family away from home; and my mother and father, Maclovia and Larry Poulsen, who have helped me become what I am and about whom I cannot say enough.

Stanford University
November 1991

William L. (Lee) Poulsen

Financial support for this research and my studies at Stanford was provided by the Office of Naval Research under grant number N00014-87-K-0299 and a National Science Foundation Fellowship.

Contents

Abstract	iv
Acknowledgements	v
List of Tables	xi
List of Figures	xii
1 Introduction	1
1.1 Motivation	1
1.2 Description of the Problem	5
1.3 Review of Previous Work	12
1.4 Chapter Descriptions and Contributions of the Research	19
2 Overview of VLF Waveguide Theory	22
2.1 Theoretical Considerations	23
2.1.1 Ray Theory	24
2.1.2 Mode Theory	26
2.2 Overview of Waveguide Mode Theory	27
2.2.1 Inhomogeneous Waveguides	30

2.3	Determination of the Mode Refractive Index S_n (VLF Waveguide Mode Theory)	31
2.3.1	Numerical Solutions of the Mode Equation: MODEFNDR . . .	34
2.4	Examples	36
2.4.1	Ideal (Perfectly Conducting) Waveguide Boundaries	36
2.4.2	“Real” Waveguide Boundaries	38
2.4.3	Field Strength versus Altitude	40
2.4.4	Initial Excitation versus Mode Number	43
3	Two-dimensional Modeling Method	49
3.1	Simple Two-dimensional Modeling	49
3.2	2-D Homogeneous Propagation Example	53
3.3	Mode Conversion	56
3.3.1	The NOSC “Long Wave Propagation Capability” Program . . .	58
3.3.2	The Ground Parameters	61
3.3.3	The Ionospheric Parameters	61
3.4	2-D Multiple Slab (Mode Conversion) Example	62
3.5	2-D Modeling in the Presence of an Ionospheric Disturbance	62
4	Three-dimensional Modeling Method	67
4.1	Formulation of the Method	67
4.1.1	Modal Electric Field Scattered by an Ionospheric Disturbance . .	68
4.1.2	Relationship between the Direct Modal Field e_n^o and the Scattered Modal Field e_n^s	73
4.2	The Scattering Disturbance Model	74

4.3	Properties of the Modeled Scatterers	77
4.3.1	Insensitivity of the Scattering to Surface Conductivity Variations under the Disturbance Region	77
4.3.2	Beamwidth of Density Enhancement Scatterers	83
5	Single Mode 3-D Scattering Model	89
5.1	Methodology	89
5.2	Results	91
5.3	Discussion and Comparison	97
5.4	Summary and Conclusions	105
6	Multiple Mode Scattering Model	107
6.1	Introduction	107
6.2	The Model	108
6.2.1	Cylindrical Spreading on a Spherical Surface and the LWPC Code	111
6.2.2	Simplifying Computational Approximations	112
6.2.3	The Methodology	115
6.3	Example of the Use of the 3-D Multiple Mode Model	116
6.4	Some Results Obtained with the Multiple Mode Model	119
6.4.1	The Effect of Disturbed Density Profile Variation on Received Signal Perturbations	121
6.4.2	Dependence of Perturbations in the Received Signal on the Re- ceiver Location	129
6.4.3	Dependence of the Signal Strength versus Distance Pattern on the “Ambient” Ionospheric Density Profile	131
6.5	Conclusions	135

7	Summary & Suggestions for Future Work	136
7.1	Summary and Contributions	136
7.2	Suggestions for Future Work	140
7.2.1	Areas of Possible Further Study	141
7.2.2	Improvements to the Model	142
A		144
A.1	Approximate Analytic Expression for the Scattered Field	144
	Bibliography	147

List of Tables

1.1	List of important VLF transmitters	9
2.1	Relative initial excitation levels and attenuation rates for the first 24 modes of a 25 kHz signal above a sea-water surface for an ambient nighttime lower ionosphere.	46

List of Figures

1.1	Depiction of the cause of Trimpi events.	2
1.2	Typical daytime and nighttime electron and daytime ion density profiles versus altitude.	6
1.3	Electron density versus altitude for a typical nighttime lower ionosphere.	8
1.4	(a) Schematic representation of a VLF signal propagating under an ambi- ent ionosphere. (b) Received amplitude of a 48.5 kHz signal transmitted at a constant amplitude.	11
1.5	(a) Schematic depiction of a perturbed ionosphere. (b) Representative electron density profile within the disturbed region. (c) Typical Trimpi event seen on a 48.5 kHz signal at the receiver.	13
2.1	Geometry of the Earth-ionosphere VLF waveguide problem.	22
2.2	Possible discrete ray paths that complete an integral number of "hops" between the transmitter and the receiver.	25
2.3	Two superposed plane waves propagating in a flat, infinitely wide wave- guide with parallel, sharply-defined boundaries.	27
2.4	A flat, infinitely wide waveguide with sharply defined boundaries showing the reflection angles and geometry of the mode or resonance condition. .	33

2.5	(a) Representation of the Earth-ionosphere waveguide as a waveguide with flat, parallel, sharply-defined, and isotropic boundaries. (b) The first 20 mode, or eigenangle, solutions for a 25 kHz signal propagating in the waveguide shown in Figure 2.5a assuming a boundary separation of 85 km.	37
2.6	(a) Representation of the actual Earth-ionosphere waveguide including Earth curvature and the smoothly varying electron density of the ionospheric 'boundary'. (b) The first 24 mode or eigenangle solutions for a 25 kHz signal propagating in the Earth-ionosphere waveguide with the typical nighttime ambient ionosphere represented by Figure 1.3 and a sea-water Earth surface.	39
2.7	(a) Relative magnitude versus altitude of the three rectangular coordinate components of the modal electric field of mode QTM ₂ for the example depicted in Figure 2.6. (b) The three components of the modal magnetic field corresponding to the electric field magnitudes shown in Figure 2.7a.	41
2.8	(a) Relative magnitude versus altitude of the three components of the modal electric field of mode TM ₂ for the 'ideal' case depicted in Figure 2.6. (b) The corresponding magnetic field components for the 'ideal' case.	42
2.9	(a) Component electric field structure versus altitude of mode QTM ₇ for the conditions depicted in Figure 2.6. (b) The corresponding magnetic field structure of mode QTM ₇ . (c) The component electric field structure of mode QTE ₇ . (d) The corresponding magnetic field structure of mode QTE ₇ .	45
2.10	(a) Relative initial excitation level (in dB) of the first 24 modes for the example depicted in Figure 2.6. (b) The initial attenuation rate (in dB/Mm) for these same 24 modes.	48
3.1	Geometry of the 2-D VLF Earth-ionosphere waveguide propagation problem.	52

3.2	2-D calculation of vertical electric field strength versus distance for two different homogeneous ground conductivities.	54
3.3	2-D calculation of vertical electric field strength versus distance at two different frequencies.	55
3.4	2-D calculation of the total vertical electric field strength versus distance for three different receiver elevations.	57
3.5	Explanatory illustration of mode conversion.	59
3.6	(a) Electric field strength along the NSS to Stanford path. (b) Phase of the signal versus path distance.	63
3.7	(a) Schematic illustration of the 2-D method for modeling waveguide propagation in the presence of a disturbance along the waveguide. (b) Profiles of electron density versus altitude of the ambient ionosphere and within the disturbance region used to calculate Figures 3.7c and d. (c) Amplitude of the total vertical electric field as a function of distance under ambient conditions and in the presence of the disturbance. (d) Corresponding phase of the signal.	66
4.1	(a) Side view representation of the Earth-ionosphere waveguide between a transmitter and receiver separated by a distance d along the surface of the Earth. (b) A plan view, seen from above, of the situation depicted in Figure 4.1a showing the three-dimensional configuration of the problem	69
4.2	Phasor diagram illustrating the relationship between the total signal modal field e_n , the direct, or unperturbed, signal modal field e_n^o , and the scattered signal modal field e_n^s	73
4.3	Ionospheric profiles used for examples and comparisons in this work. . .	76
4.4	Eigenangles for different surface conductivities.	78
4.5	" ΔS^2 " versus mode number.	80

4.6	Eigenangle solutions for different conductivities and for 15 and 50 kHz signals.	81
4.7	Eigenangle solutions for ice cap surface conditions.	82
4.8	(a) Schematic description of the scattering geometry and the definition of angle ψ . (b) Scattered modal signal strength versus angle ψ for a 25 kHz signal and a disturbance 200 km in diameter.	84
4.9	Scatter 'radiation' patterns for 15 and 50 kHz signals.	85
4.10	Scattered radiation patterns for different disturbed density profiles. . . .	86
4.11	Scattered modal strength versus ψ for disturbances of different sizes. . .	88
5.1	Plot of the ambient electron density distribution with altitude and three different ionospheric disturbance profiles used in the calculations.	92
5.2	Contour plots of the calculated ΔA and $\Delta\phi$ seen at the receiver produced by a circularly symmetric disturbance region with a horizontal Gaussian distribution.	94
5.3	Two-dimensional 'cut' along the y direction of Figure 5.2 taken at a fixed value along the x axis ($x_T/d = 0.25$ in this case).	95
5.4	Plot showing the dependence of the magnitude and phase of the scattered signal e_n^s on distance (in wavelengths) away from the GCP.	96
5.5	(a) Plots of ΔA and $\Delta\phi$ similar to those shown in Figure 5.4 except the two-dimensional 'cut' is taken along the x direction of Figure 5.2, along the GCP (i.e., for a fixed value along the y axis of $y_o = 0$). (b) Plots of ΔA and $\Delta\phi$ versus y similar to those shown in Figure 5.4 except that the effective radius was fixed at $a = 5 \lambda$ and the three curves shown represent the changes produced by the three density profiles of Figure 5.1	99
5.6	Figure 11a of <i>Inan and Carpenter</i> (1987) showing a comparison of measured simultaneous amplitude (ΔA) and phase ($\Delta\phi$) perturbation sizes on the NPM signal observed at Palmer Station, Antarctica.	101

5.7	(a) A plot of calculated values of $ \Delta A $ versus $ \Delta \phi $ for a range of patch radii a from 3.75λ to 10λ , and a regularly spaced grid of patch locations (x_o, y_o) . (b) A plot similar to Figure 5.7a except that disturbance density profile III of Figure 5.1 was used in the calculations instead of profile I.	102
6.1	Plot of the electron density distribution versus altitude at the center of a disturbance produced by an LEP event.	109
6.2	A depiction of the methodology used to calculate the total perturbed value of the electric field observed at the receiver.	110
6.3	The 'incident sector' and 'scattered sector' within which lie all propagation paths from the transmitter to each infinitesimal area element and from each area element to the receiver, respectively.	114
6.4	Amplitude and phase plots of a signal propagating along the three great circle paths shown for one particular example of a disturbed situation. .	118
6.5	Phasor diagrams of the relative signal strength and phase of each mode of the propagating signal located at the points indicated by an arrow along the three propagation paths.	120
6.6	(a) Reproduction of four of the five disturbed electron density profiles from Figure 4.3. (b) Change in the received amplitude and phase caused by a lower ionospheric disturbance for each of the four disturbed density profiles shown in Figure 6.6a.	122
6.7	Change in the received amplitude and phase caused by a lower ionospheric disturbance versus four disturbed density profiles for the same conditions as in Figure 6.6 except that $\sigma = 10^{-3}$ S/m.	123
6.8	Eigenangle solutions for $f = 25$ kHz and $\sigma = 4$ S/m for vertical electron density profiles III and IV of Figure 6.6a.	124
6.9	Component vertical electric field structure of modes QTM ₇ and QTE ₇ of a 25 kHz signal for $\sigma = 4$ S/m and ionospheric electron density profiles III and IV of Figure 6.6a.	127

6.10	Plots of $\sigma_{ionosphere}$ versus altitude corresponding to the density profiles shown in Figure 4.3 for a 25 kHz wave.	128
6.11	(a) Undisturbed electric field strength versus propagation path distance of a 25 kHz signal over a homogeneous $\sigma = 10^{-3}$ S/m surface. (b) Change in the received amplitude of Figure 6.11a versus receiver location due to a 3-D disturbance with effective radius $a = 50$ km centered directly over the GCP at a distance 3000 km away from the transmitter. (c) Change in the received phase corresponding to Figure 6.11b.	130
6.12	(a) Electron density versus altitude for two different "ambient" ionospheres. (b) Eigenangle solutions of a 25 kHz signal for both "ambient" profiles of Figure 6.12a and a sea-water surface. (c) Electric field strength versus distance corresponding to both sets of mode solutions shown in Figure 6.12b for homogeneous waveguide conditions.	134

Chapter 1

Introduction

This research addresses the topic of three-dimensional numerical modeling of very low frequency (VLF) wave propagation in the Earth-ionosphere waveguide, and the scattering effect on these waves of transient, localized disturbances in the lower ionosphere. The model developed here significantly enhances the capabilities of existing two-dimensional VLF propagation models which are used in various applications involving VLF navigation and communication. The development of a 3-D model was primarily motivated by the need to investigate effects of localized ionospheric disturbances due to lightning discharges as discussed in section 1.1 below. However, this model is general enough to be used in other applications involving disturbances of finite horizontal extent. In this chapter, we introduce the motivation for the work, give a simple description of the general problem addressed, provide a brief background on VLF propagation in the Earth-ionosphere waveguide, and review previous work done in this area. A brief outline of each chapter and a list of the specific contributions of this research are separately provided in section 1.4.

1.1 Motivation

The primary motivation for this research is depicted in Figure 1.1 [Inan *et al.*, 1988c]. The phenomenon investigated here involves the transient appearance of a disturbance of finite-extent in the lower region of the nighttime ionosphere (known as the “D region”) consisting of a localized enhancement of the ambient plasma density. Such ionospheric

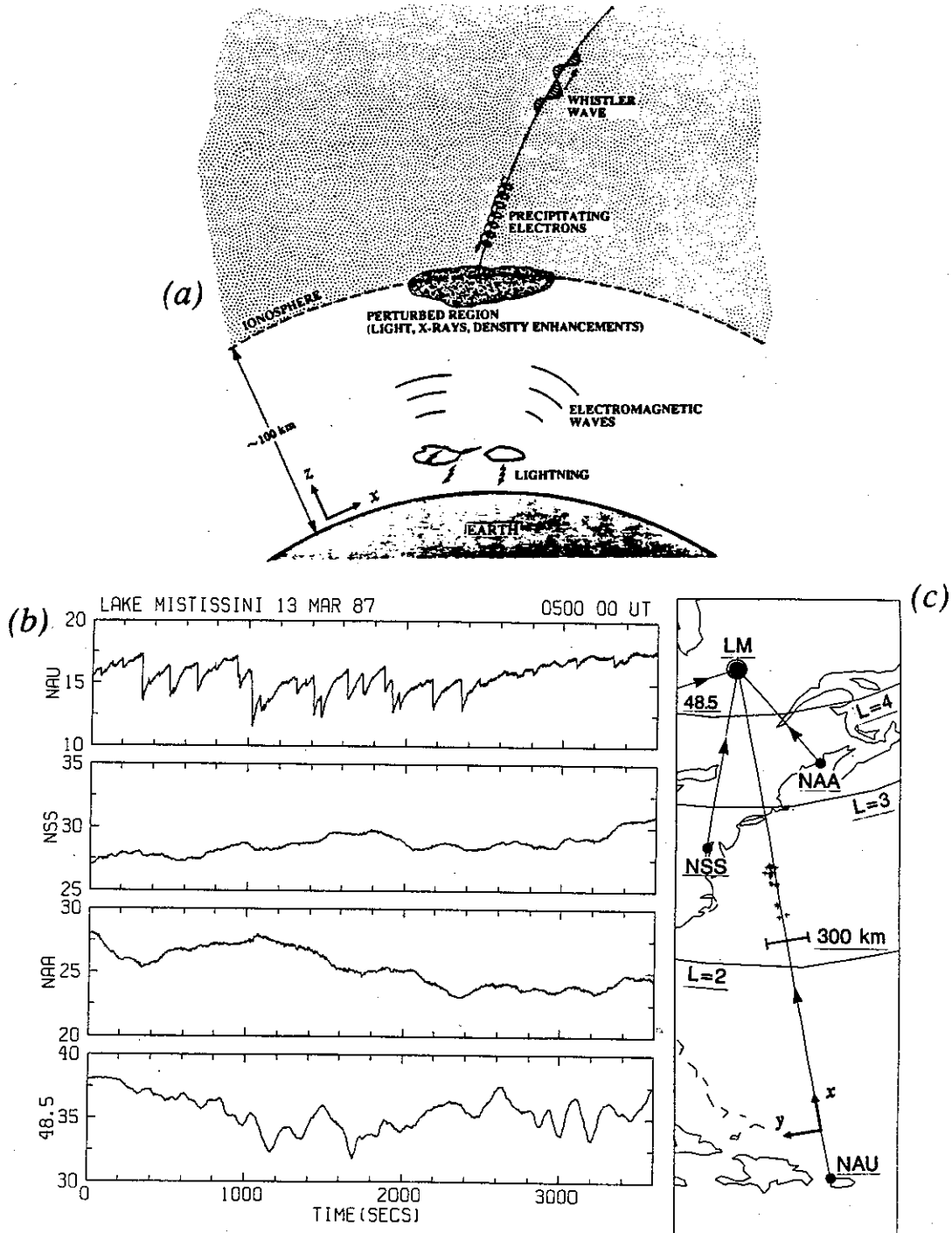


Figure 1.1: (a) Illustration of lightning-induced electron precipitation and the associated ionospheric disturbance (typically, enhanced secondary ionization generated by precipitating energetic electrons). (b) Amplitudes of four different VLF signals measured at Lake Mistissini (LM), Quebec. The signal amplitudes are plotted in arbitrary linear units. The data points plotted were averaged over ~ 1 s. (c) The great circle propagation paths of the four signals. The locations of cloud-to-ground lightning flashes detected during the period in Figure 1.1b are shown on the map as pluses ('+').

disturbances are assumed to be caused by bursts of precipitating energetic (>50 keV) radiation belt electrons that generate secondary ionization at D region altitudes. The precipitation of these electrons is in turn believed to be induced by whistler wave energy, generated by lightning discharges. This wave energy enters the ionosphere, propagates up along the Earth's magnetic field lines within the ionosphere and up to the magnetosphere, and interacts with stably trapped energetic (>50 keV) electrons in the geomagnetic equatorial region of the radiation belts causing the electrons to become un-trapped and to precipitate into the upper atmosphere [Helliwell *et al.*, 1973; Lohrey and Kaiser, 1979; Voss *et al.*, 1984; Carpenter and LaBelle, 1982; Carpenter *et al.*, 1984, 1985; Inan *et al.*, 1985; Inan and Carpenter, 1986, 1987; Tolstoy *et al.*, 1986]. (See also Tolstoy, 1983; Cotton, 1989; Wolf, 1990; Adams, 1990.)

The first evidence of precipitation of energetic electrons by whistler waves from lightning was in the form of associated perturbations in the amplitude of VLF signals propagating in the Earth-ionosphere waveguide [Helliwell *et al.*, 1973] and subsequently, in the phase of such VLF signals [Lohrey and Kaiser, 1979]. In recent years, the resulting characteristic perturbations of subionospheric VLF signals, referred to as "Trimpi" events, or as lightning-induced electron precipitation (LEP) events, have been extensively used to investigate the occurrence statistics and geographic distribution of this phenomenon [Carpenter and Inan, 1987; Inan *et al.*, 1988a, b], their association with magnetospheric whistler waves [Carpenter and LaBelle, 1982; Inan and Carpenter, 1986] and lightning discharges [Inan *et al.*, 1988c], as well as their association with patches of secondary ionization [Dowden and Adams, 1988, 1989a; Poulsen *et al.*, 1990].

The VLF group of the Space, Telecommunications, and Radioscience (STAR) Laboratory at Stanford University has set up an extensive network of receiving stations that continuously monitor both the amplitude and the phase of various VLF transmitter signals during local nighttime hours, and characteristic signatures of lightning-induced ionospheric disturbances are regularly observed in the amplitude and/or phase of these signals. For example, the first panel of Figure 1.1b which illustrates the basic nature of the VLF perturbations, shows a particular sequence of events in the amplitude of the 28.5 kHz NAU signal originating in Aguadilla, Puerto Rico and observed at Lake Mistissini.

The 'events' are characterized as rapid (~ 1 s) changes in the amplitude, followed by slow recoveries (~ 10 – 100 s) to the ambient level. Notice that this same type of signature is not seen on the lower panels, which show the amplitude of several other signals, also observed at Lake Mistissini, from transmitters located at several different places in North America. The geography of the transmitter-receiver paths is shown in Figure 1.1c. Also indicated in Figure 1.1c by the small '+' symbols are the locations of a number of cloud-to-ground lightning discharges observed by the SUNY-Albany (State University of New York at Albany) lightning detection network [Orville *et al.*, 1983, 1987] which occurred during the same period of time indicated in Figure 1.1b.

The characteristic amplitude perturbations observed on the NAU signal are believed to be the signatures of ionospheric disturbances caused by the lightning discharges occurring on or near the great circle path (GCP) of propagation between the transmitter and receiver. That the ionospheric disturbance regions associated with these discharges are localized is consistent with the fact that they are seen only on one transmitter signal (NAU) at Lake Mistissini, but not on any of the others [Inan *et al.*, 1988c]. Because these particular events seen on the NAU signal are believed to be caused by disturbances produced by precipitating electrons rather than being produced directly by the lightning energy, the disturbances need not have been located directly over the lightning discharge. However, if the discharge energy entered the ionosphere directly overhead, or did not propagate very far before doing so, the locations of the lightning discharges, which happen to be within 150 km of the GCP from NAU to Lake Mistissini, may represent the locations of the disturbances which caused the perturbations seen in the NAU signal amplitude shown in Figure 1.1b. (Evidence that some disturbances may be located far (~ 400 – 1100 km) from the location of the lightning discharges leading to their formation can be found in Yip *et al.*, [1991]. Evidence that some disturbances may have been caused directly by the upward coupling of the lightning discharge energy are described in Inan *et al.*, 1988c]. Disturbances may also be caused by electrons precipitating in the region geomagnetically conjugate to where the lightning discharge energy entered the ionosphere [Burgess and Inan, 1990].)

The motivation for this work was to develop a complete 3-D model that quantitatively accounts for the signal amplitude and phase changes described, given (i) electrical properties (e.g., conductivity) of the ambient as well as the disturbed ionosphere and the ground, and (ii) location, size, and shape of the disturbances. The ionospheric disturbance is typically modeled in terms of a density enhancement as a function of altitude, which in turn is determined by the flux and energy spectra of precipitating electrons. A quantitative model is thus needed in order to interpret the observed amplitude and phase changes in terms of the characteristics of the precipitation. Also, since the signal along a particular path can be affected by localized disturbances located directly over the GCP, as well as completely off the path, a three-dimensional model is needed.

Throughout this dissertation the three dimensions will be defined as follows (see Figure 1.1): x is the direction of propagation (i.e., the distance along the GCP); z is the vertical direction (i.e., altitude); and y is the direction perpendicular to the plane of propagation (i.e., perpendicular to the x - z plane).

1.2 Description of the Problem

One of the properties of electromagnetic waves is that they can be channeled or guided between partially conducting boundaries commonly referred to as a waveguide, such that the wave energy moves away from the energy source (the transmitter, in this case) along this waveguide structure. The cross-sectional dimensions of a waveguide are usually of the same order of magnitude as the wavelength of the signal being guided. In the case of VLF or LF waves (which have wavelengths between approximately 5 and 50 km or so) the space between the Earth's surface and the lower ionosphere (i.e. the atmosphere), forms a waveguide that is 85 km (60 km) in height at nighttime (daytime). (Officially, the "very low frequency" or VLF band is 3–30 kHz which corresponds to wavelengths in free space of 100–10 km, while the "low frequency" or LF band consists of 30–300 kHz which corresponds to free-space wavelengths of 10–1 km. In this report, we will refer to the frequencies of interest as "VLF" frequencies, even though some of the frequencies considered extend into the LF band.)

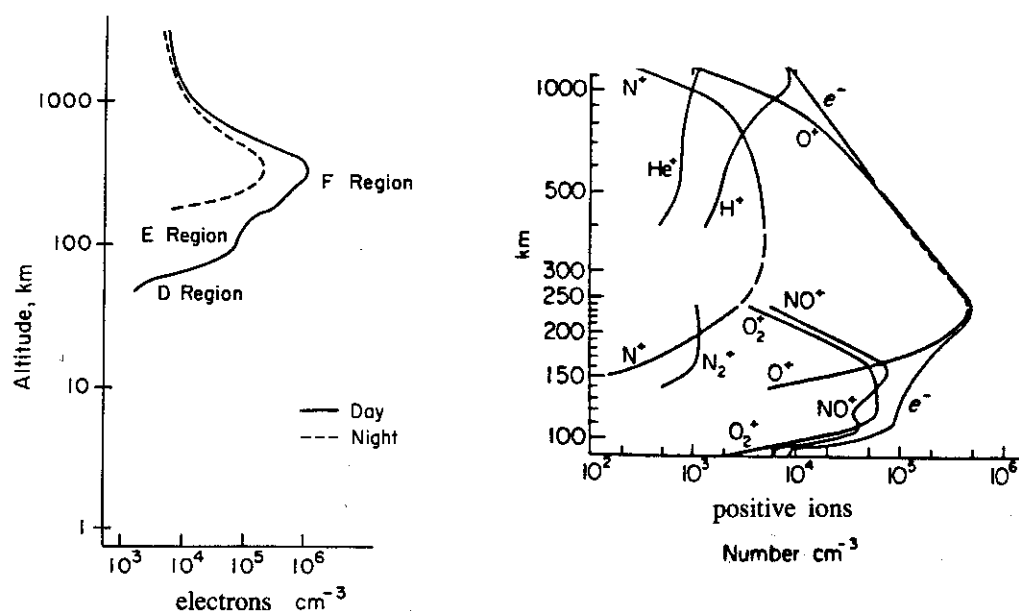


Figure 1.2: Typical daytime and nighttime ionospheric electron and daytime ion density profiles versus altitude (from *Kelley and Heelis* [1989]).

The ionosphere has been defined to be that part of the atmosphere above about 50 km in altitude in which free electrons exist in sufficient numbers to have an important effect on the propagation of radio waves [*Davies*, 1966; *Ratcliffe*, 1972]. It is created and maintained by a dynamic equilibrium between the production of ions and free electrons in the upper atmosphere, and a number of processes including: a) the attachment of charged particles to nearby neutral molecules, b) the recombination of electrons and ions, and c) diffusion caused by the decrease in density of the atmosphere with altitude (which, among other things, changes the various collision frequencies). The ions and free electrons are produced by the ionization of atoms and molecules caused by the absorption of solar and cosmic electromagnetic radiation which increases in intensity with altitude. The net result is that the electron (and ion) density within the ionosphere varies with altitude, and also from day to night (due to the lack of solar radiation during local nighttime). Figure 1.2 shows typical profiles of electron and ion density versus altitude [*Kelley and Heelis*, 1989].

There is no distinct upper boundary to the ionosphere. However, the density of atmospheric constituents decrease steadily with increasing altitude and above roughly 1000 km the effect of collisions becomes negligible and the behavior of the charged particles become dominated by the Earth's magnetic field [Ratcliffe, 1972; Park and Carpenter, 1978]. This region of the Earth's upper atmosphere is commonly referred to as the 'magnetosphere'.

The ionosphere is further subdivided into the *D*, *E*, and *F* layers with the following characteristics [Davies, 1966]:

D region 50–90 km altitude

E region 90–140 km

F region >140 km.

In this research the effects of interest occur in the lowest, or *D* region, layer of the ionosphere between ~50 and 100 km. The electron density increases rapidly enough in the lower ionosphere that it reflects most of the VLF wave energy that impinges upon it. Figure 1.3 shows a plot of the electron density as a function of altitude for a typical nighttime lower ionosphere.

Both natural and man-made VLF signals propagate within the Earth-ionosphere waveguide. The natural VLF signals, which are excited by lightning discharges, are known as "sferics", are of impulsive nature and constitute the major impediment to VLF navigation and communication as intense impulsive noise. Man-made signals are produced by a number of VLF transmitters located throughout the world. Despite their relatively small usable bandwidths (~20 to 150 Hz) and low transmitting antenna radiation efficiencies (~10 to 20%), VLF signals are extensively used for global communication and navigation because waves at these frequencies have relatively low attenuation versus distance and remain relatively stable with time [Davies, 1966]. Also, VLF waves can be guided for very long distances between the Earth and the ionosphere (~5,000 to 20,000 km) making these frequencies particularly attractive for navigational beacons and time signals. Table 1.1 [Cotton, 1989; Inan *et al.*, 1984; Parrot, 1990] lists a number of important VLF communication and navigation transmitters in various parts of the world.

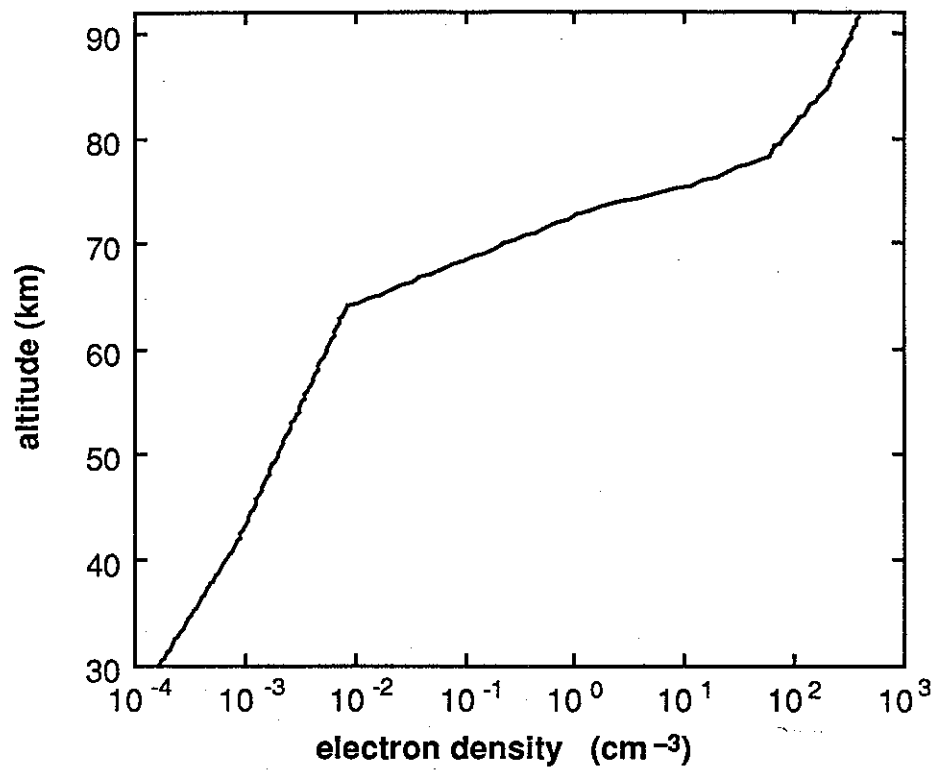


Figure 1.3: Electron density versus altitude for a typical nighttime lower ionosphere.

Table 1.1: List of important VLF transmitters

Transmitters	Latitude	Longitude	Radiated Power (kW)	Frequency (kHz)
<i>Communication Transmitters</i>				
NAA (Cutler, Maine)	44° 39' N	67° 17' W	1000	24.0
NLK (Jim Creek, Washington)	48° 12' N	121° 55' W	850	24.8
NPM (Lualualei, Hawaii)	21° 25' N	158° 09' W	300	23.4
NSS (Annapolis, Maryland)	38° 59' N	76° 27' W	265	21.4
NAU (Aguadilla, Puerto Rico)	18° 25' N	67° 09' W		28.5
"48.5" (Silver Creek, Nebraska)	41° 30' N	97° 36' W		48.5
NWC (N. W. Cape, Australia)	21° 49' S	114° 10' E	1000	22.3
GBR (Rugby, Great Britain)	52° 20' N	00° 20' W	300	16.0
UMS (Gorki, USSR)	56° N	44° E	~1000	16.2
RPS (Eastern Siberia, USSR)	43° N	135° E	~1000	17.1
<i>Navigation Transmitters</i>				
Omega A (Norway)	66° 25' N	13° 08' E	10	10.2–13.6
Omega B (Liberia)	06° 18' N	10° 00' W	10	10.2–13.6
Omega C (Hawaii)	21° 24' N	157° 49' W	10	10.2–13.6
Omega D (North Dakota)	46° 21' N	98° 29' W	10	10.2–13.6
Omega E (La Réunion)	20° 58' S	55° 17' E	10	10.2–13.6
Omega F (Argentina)	43° 03' S	65° 11' W	10	10.2–13.6
Omega G (Trinidad)	10° 42' N	61° 38' W	10	10.2–13.6
Omega H (Japan)	34° 36' N	129° 27' E	10	10.2–13.6
Komsomolskamur (USSR)	50° 34' N	136° 58' E	10–500	11.9–15.6
Novosibirsk (USSR)	55° 04' N	80° 58' E	10–500	11.9–15.6
Krasnodar (USSR)	45° 02' N	38° 39' E	10–500	11.9–15.6
<i>Experimental Transmitter</i>				
Siple (Antarctica)	75° 56' S	84° 14' W	~3	1–10

Now suppose that we have a transmitter sending out a VLF signal with constant amplitude, and a receiver, some distance away, receiving this signal. The wave energy will propagate in the Earth-ionosphere waveguide, interacting with the two boundaries in a manner depending on the electrical properties of those two boundaries. (See Figure 1.4*a*.) Some of the properties of the ionosphere pertinent to VLF propagation include the local electron and ion densities, the local particle collision frequencies, and the local magnetic field. Some pertinent properties of the Earth's surface include the ground or water conductivity (σ), relative permittivity (ϵ_r), and elevation above sea level.

Because these properties remain relatively constant over a period of seconds or minutes, the amplitude and phase of the signals measured at a receiver remain fairly constant over such time scales. Figure 1.4*a* shows a schematic representation of a signal propagating along the Earth-ionosphere waveguide. Figure 1.4*b* is a typical example of the amplitude of a 48.5 kHz signal received several thousand kilometers away showing relatively small changes in overall amplitude versus time. It should be noted, however, that there are diurnal changes in the density of the lower ionosphere, and therefore, due to this and other factors, a constant amplitude transmitted signal often exhibits slow changes in amplitude or phase on time scales of the order of tens of minutes or longer [Davies, 1966].

When sudden (<1 s) changes in one or the other of the two waveguide boundaries occur, the amplitude and the phase of the signal as observed at receivers beyond the disturbance (or distortion) also exhibit sudden (<1 s) changes. Such disturbances may be on or near the great circle path (GCP) of propagation between the source and the receiver. The receiver may then detect a rapid change in either the amplitude or phase of the signal (or both) with respect to the relatively constant values prior to appearance of the disturbance.

Energetic electrons dislodged from the radiation belts (by wave energy from a lightning discharge, for example) precipitate into the atmosphere in the form of short (<1 s) bursts, causing secondary ionization and thereby rapidly (<1 s) enhancing the electron density in a localized region of the lower ionosphere. Such a disturbance could in turn perturb the amplitude and/or phase of the VLF signal measured at the receiver if the

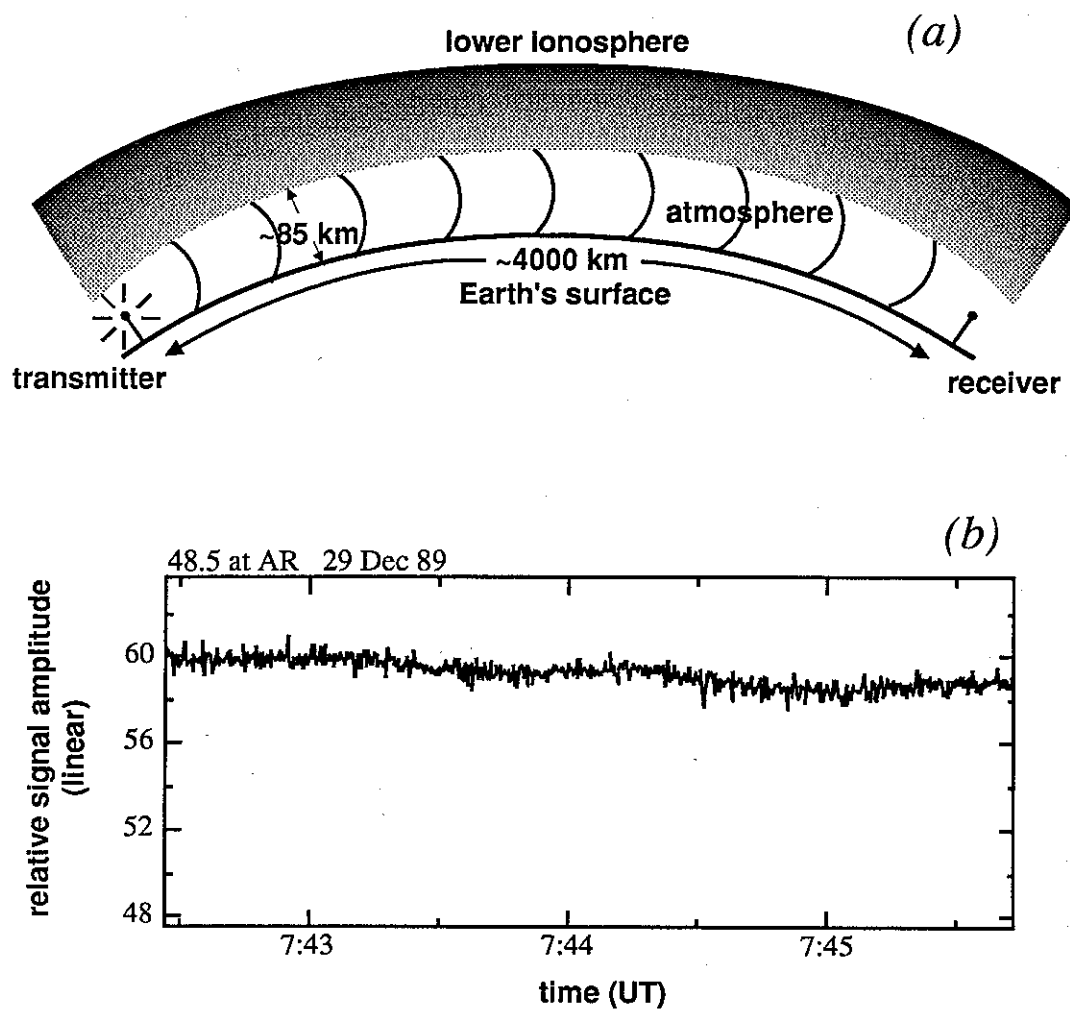


Figure 1.4: (a) Schematic representation of a VLF signal propagating under an ambient ionosphere. (b) Typical example of the received amplitude of a 48.5 kHz signal transmitted at a constant amplitude.

disturbance was located on or near the propagation path. Figure 1.5a schematically illustrates this type of a disturbance in the Earth-ionosphere waveguide and Figure 1.5b shows a representative electron density versus altitude profile at the center of such a disturbance. Figure 1.5c shows sudden (<1 s) amplitude change of ~ 2 dB recorded on the 48.5 kHz signal just after the portion of the record that was shown in Figure 1.4b. The sudden amplitude change recovers back to the ambient over a time of ~ 100 s. This characteristic temporal signature, commonly known as a “Trimp event”, consisting of a rapid (<1 s) change followed by a relatively slow (10–100 s) recovery, is typical of subionospheric VLF signal responses to lightning-induced ionospheric disturbances of the type shown in Figures 1.5a and 1.5b. As the newly generated secondary ionization gradually recombines with ions or attaches to neutral atoms or molecules [Dingle, 1977], the disturbance gradually disappears. The electron density returns to its prior, ambient condition, and thus, the measured signal also gradually returns to its prior, unperturbed level (as indicated by the arrows in Figures 1.5b and 1.5c).

The purpose of this research was to develop a three-dimensional model of the effect that a localized disturbance (of finite transverse extent), in the lower ionosphere’s electron density, has on VLF waves propagating in the Earth-ionosphere waveguide; especially its effect on the amplitude and phase measured at ground-based receivers. The model developed is built on extensive past work that led to a full-wave, numerical, two-dimensional VLF/LF Earth-ionosphere waveguide propagation program, known as the Long-Wave Propagation Capability (LWPC) [Ferguson *et al.*, 1989], developed by the Naval Ocean Systems Center (NOSC), and on the VLF diffraction theory developed by Wait [1964a, b, c]. This model can be easily extended to model disturbances involving changes in other properties of the lower ionosphere boundary, such as for example the electron or ion collision frequency or temperature.

1.3 Review of Previous Work

The first major effort at a detailed numerical study of the influence of localized density enhancements produced by lightning-induced electron precipitation on subionospherically

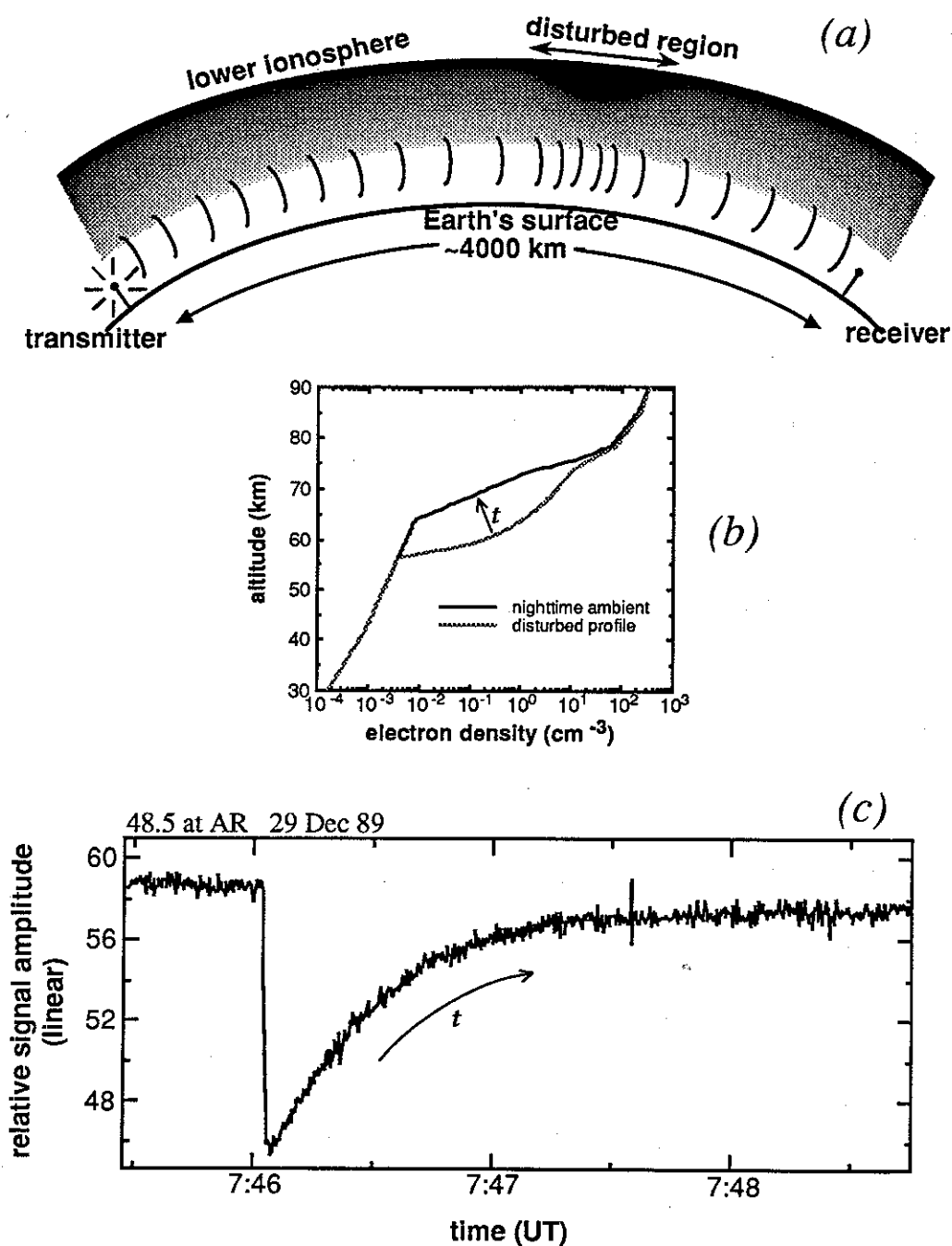


Figure 1.5: (a) Schematic depiction of a perturbed ionosphere. (b) Representative electron density profile within the disturbed region. (c) A typical VLF signature (commonly referred to as a "Trimp event") of a lightning-induced ionospheric disturbance observed on the 48.5 kHz signal at Arecibo.

propagating VLF waves was that of *Tolstoy* [1983; *Tolstoy et al.*, 1982, 1986]. That study employed a full-wave 2-D waveguide mode propagation model (a precursor to the LWPC program used in our research) to investigate the effects on the received signal amplitude and phase of disturbances in the form of 2-D “strips” (infinite in transverse extent) located on a great circle path (GCP). The *Tolstoy* study used the *Rees* [1963] model to calculate the disturbed electron density profiles for the disturbances, using monoenergetic precipitating electrons with energies ranging from 50–150 keV and energy fluxes in the range of 10^{-7} to 10^{-3} erg cm $^{-2}$ s $^{-1}$. Calculations were made for several transmitter–receiver paths where the transmitters were located in North America (NPM, NLK, NSS, and NAA; see Table 1.1) and the receivers were located in Antarctica (Palmer Station–65° S, 64° W; Eights Station–75° S, 77° W; and Siple Station–76° S, 84° W). The results were compared to Trimpi events observed at the receiving stations and found to be generally consistent with the measured data. However, because it was a two-dimensional model, it necessarily could not account for the effects of disturbances of finite extent nor of disturbances located off the GCP, and in some instances gave results that were much larger than that seen in the measured data.

A simplified single waveguide mode analysis of the effects of typical disturbances on subionospheric VLF signals was put forth by *Inan et al.* [1985] and *Inan and Carpenter* [1987]. These authors used quantitative estimates of precipitating electron fluxes induced by lightning as provided by theory [*Chang and Inan*, 1985] and measurement [*Voss et al.*, 1984] to determine the amount of secondary ionization to be produced at nighttime *D* region altitudes. The resulting effects on the subionospheric VLF signal were then represented as simple changes in reflection height leading to amplitude and phase changes evaluated using simple analytical expressions [*Inan and Carpenter*, 1987]. It was argued that such analyses would be applicable to cases of propagation over long all-sea-based paths where the signal at the receiver would be constituted by a single dominant waveguide mode. Theoretically computed ratios of expected amplitude and phase changes were compared with those measured at Palmer Station, Antarctica on a 12,000 km path from Hawaii (NPM transmitter in Table 1.1) and a ~2400 km path from Argentina (Omega F transmitter from Table 1.1). While there was general agreement between the data and theory, ratios of measured amplitude changes to phase changes were found to be

somewhat larger than the theory predictions, probably due to effects of additional modes. *Inan and Carpenter* [1987] also noted the need for a more general 3-D model that could account for effects of disturbances located off the great circle path.

Cotton [1989] developed a full-wave 2-D mode propagation program, independent of the NOSC programs, tailored to model VLF waveguide propagation frequencies below 10 kHz in the Antarctic (sea-water, ice shelf, and ice cap; highly vertical magnetic field) terrain. It used a flat-earth approximation and a sharply bounded ionosphere. The model was used to make detailed calculations of the amplitude, phase, arrival bearing, and signal elevation for VLF wave propagation for a number of Antarctic signal paths. The ionospheric disturbances were modeled as simple reductions in the undisturbed VLF reflection height. Such depressions were assumed to have a gaussian variation with horizontal distance along the GCP from the center of the disturbance, and the depth of the depression was obtained by converting calculated ionospheric ionization enhancement to an equivalent reduction in VLF ionospheric reflection height for a sharply bounded ionosphere.

The other major effort in this area was the study done by *Adams* [1990; *Dowden and Adams*, 1988, 1989a, 1989b, 1990]. The main thrust of that work was the measurement at Dunedin, New Zealand of characteristic VLF perturbations of the type shown in Figure 1.5 at the two carrier frequencies (200 Hz apart) utilized for the minimum shift keying (MSK) modulation of the NWC (Australia; see Table 1.1) VLF transmitter, and made by two receivers spaced less than a wavelength apart. The information obtained was used to calculate the group delay of the scattered signal relative to the direct signal and the arrival bearing of the scattered wave compared to that of the direct signal. The results of using this information to determine the disturbance location were compared to the theoretical results calculated using *Wait's* [1964a] 3-D diffraction formulation for the case of a single mode and for the case of two interfering modes. Their results suggest that a number of the disturbances causing the observed events could not be explained by either a 2-D model, such as those described above, or by *Wait's* 3-D WKB formulation; implying that these disturbances consisted of localized regions where sharp variations from the ambient conditions occurred due to the LEP-generated ionization. *Dowden*

and Adams modeled the ionospheric disturbance as a depression (in 3-D) in the VLF ionospheric reflection height having a gaussian variation with horizontal radial distance from the center of the disturbance.

A substantial amount of experimental work has recently been done with respect to subionospheric VLF signatures of lightning-induced ionospheric disturbances (i.e., Trimpi events) and related phenomena. Observations of this effect were first reported by *Helliwell et al.* [1973] as sudden changes in the amplitude of VLF transmissions. Characteristic perturbations in the phase of VLF transmissions were first reported by *Lohrey and Kaiser* [1979]. Further study on the correlation of whistlers with VLF signal changes was done by *Carpenter and La Belle* [1982]. Perturbations have been observed at frequencies as high as 780 kHz [*Carpenter et al.*, 1984] and as low as 2.5 kHz [*Carpenter et al.*, 1985]. A one-to-one correlation between ground-based measurements of VLF sferics and whistlers and energetic electron precipitation measured by low-altitude satellite was first reported by *Voss et al.* [1984]. More evidence of phase perturbations on VLF signals produced by lightning-induced electron precipitation bursts was reported by *Inan et al.* [1985], and analysis of events which added support to the mechanism as described in section 1.1 was made [*Inan and Carpenter*, 1986]. Simultaneous amplitude and phase perturbations were observed and analyzed using a single mode waveguide theory by *Inan and Carpenter* [1987]. Evidence of VLF signal perturbations caused by >1 MeV electron precipitation at $L \leq 1.8$ was reported by *Inan et al.* [1988a]. Events have also been observed at latitudes as high as $L \geq 4$ [*Hurren et al.*, 1986]. More recently, studies have been made of the geographic distribution of event occurrence [*Inan et al.* 1988b], their path-dependent properties [*Wolf and Inan*, 1990], the possibility of direct coupling between the associated lightning discharge and the disturbance itself [*Inan et al.*, 1988c], simultaneous phase and amplitude perturbations that were interpreted in terms of scattering of the signal from localized ionospheric disturbances that lie off the propagation path [*Dowden and Adams*, 1989a], simultaneous disturbance of conjugate regions of the ionosphere associated with the same lightning discharge [*Burgess and Inan*, 1990], "imaging" of the spatial distribution and occurrence of lower ionospheric disturbances [*Inan et al.*, 1990], and the spatial relationship between the propagation path of a disturbed signal and the location of the associated lightning discharge [*Inan et al.*, 1988c; *Yip et al.*, 1991]. A comprehensive

study of events on multiple VLF/LF signal paths observed at both Stanford, California and at Palmer Station, Antarctica study revealed a number of new properties that appear to be characteristic of particular signal paths and which none of the existing models could fully explain [Wolf 1990; Wolf and Inan, 1990].

Other causes of lower ionospheric disturbances and their effects on subionospherically propagating VLF waves have also been reported. Some of these include the effects of high altitude nuclear detonations [Jean and Crombie, 1963; Field and Engel, 1965], solar x-ray flares [Chilton *et al.*, 1965; Crombie, 1965], substorms and solar particle bursts [Potemra and Rosenberg, 1973; Kikuchi and Evans, 1983], stellar x-rays from x-ray stars [Svennesson *et al.*, 1972, 1979], and patches of the lower ionosphere heated by beams of high frequency (HF) transmissions [Barr *et al.*, 1984, 1985].

Before the work of Tolstoy [1983], a number of preliminary efforts were made (primarily by J. R. Wait) to theoretically model the effects of lower ionospheric perturbations on VLF wave propagation. Wait [1961] first described a 2-D model of the effects of a "localized" depression in the ionospheric reflection height on VLF waves propagating under it. Wait [1962] described a 2-D model of VLF mode propagation along a part of the Earth-ionosphere waveguide where the ionospheric reflection height changes smoothly. In Wait [1964a], a 3-D formulation of the diffraction effects of a disturbed region which is rectangular in the horizontal (x - y) plane on the propagation of VLF waves was presented. Rather than changes in the ionospheric reflection height, changes in the modal refractive index $S(x, y)$ were used to represent the disturbed region of the ionosphere. Wait [1964b] expanded on the analysis of Wait [1964a] and presented an explanation of the formulation used. The formulation in that paper, and simplified in Wait [1964c] for the case of a cylindrically symmetric ionospheric disturbance, are used as the basis for the 3-D model described in this dissertation. Crombie [1964] also presented a 3-D model of the changes in amplitude and phase of a received VLF signal due to a small, localized, depression in the ionospheric reflection height using elementary diffraction theory.

Following the basic work of Wait described above, an extensive and long-term effort was undertaken to develop general numerical models to calculate, two-dimensionally, VLF wave propagation within the Earth-ionosphere waveguide along arbitrary paths.

Much of the initial work was in developing the theoretical formulations required [Pappert *et al.*, 1967; Wait, 1968; Wait and Spies, 1968; Sheddy, 1968; Galejs, 1968; Snyder and Pappert, 1969; Morfitt and Hildebrand, 1970; Barr, 1971; Galejs, 1971], after which operational computer programs began to appear. A full-wave, 2-D, mode conversion program to calculate VLF propagation for an inhomogeneous anisotropic ionosphere called "FULLMC" was developed by NOSC [Pappert and Shockey, 1972] and initial results using it were reported in Pappert and Snyder [1972] and Pappert and Morfitt [1975]. An improved program to calculate the mode eigenangle solutions essential to the solution of the VLF waveguide propagation problem, called "MODESRCH", was also developed by NOSC [Morfitt and Shellman, 1976]. This was refined and improved, and renamed "MODEFNDR" [Ferguson *et al.*, 1985; Shellman, 1986], and a program, called "FASTMC", using a different, approximate, formulation was developed to increase the computation speed compared to FULLMC [Ferguson and Snyder, 1980] while maintaining equivalent accuracy [Pappert and Ferguson, 1986]. A program to automate the calculation of VLF wave propagation along actual paths on the Earth's surface, including actual parameter values of the chosen propagation path, called "SEGMWVGD", was developed and added to the series of NOSC programs described above [Ferguson and Snyder, 1987] culminating in the complete Long-Wave Propagation Capability (LWPC) for performing 2-D calculations of VLF wave propagation along arbitrary paths in the Earth-ionosphere waveguide [Ferguson *et al.*, 1989].

Cotton [1989] developed their own complete full-wave 2-D VLF propagation model as described earlier. Tolstoy and Rosenberg [1985] briefly presented a scheme to extend the NOSC 2-D VLF propagation model to a quasi-three-dimensional propagation model using the results of Crombie [1964]. Barr *et al.* [1985] presented the results of a simple theoretical 3-D model based on the formulation of Wait [1964a, b] and Barr [1971] specifically tailored to calculate the effects of HF heating on a localized patch of the lower ionosphere whose properties abruptly change from those of the ambient ionosphere around it.

Other work relevant to the problem of calculating the effects of localized, cylindrically symmetric, disturbances within a waveguide can be found in Nielsen [1969], Dawson and

Oberman [1959], and most recently for the Earth-ionosphere waveguide case studied in this research, in *Wait* [1991].

1.4 Chapter Descriptions and Contributions of the Research

In this section, we provide a description of the contents of each chapter, and a brief summary of the contributions described therein.

Chapter 2 contains an overview of the waveguide mode theory of VLF wave propagation in the Earth-ionosphere waveguide. The basic formulation for calculating the electromagnetic fields as a VLF wave propagates along the waveguide is given. Since the use of the waveguide mode method of describing the wave field is essential to this research, the concept of using eigenangles to identify and represent each mode is described in some detail. In order to find the eigenangles for typical ground and ionosphere parameter values, a computer program called "MODEFNDR" (which was developed by NOSC as part of LWPC) is used, and is also described in Chapter 2.

Chapter 3 describes how the formulation given in Chapter 2 is modeled numerically. It describes how the necessary physical parameters of the ionosphere and the ground are incorporated in the calculations, and then goes on to describe the need for calculating the conversion between modes due to horizontal inhomogeneities along real propagation paths. NOSC also developed a computer program that calculates VLF propagation in two-dimensions (x and z), and accounts for mode conversion as the signal propagates along a waveguide with changing boundary parameters. It is called "FASTMC", and is used in tandem with MODEFNDR. This program is described, and both of these together are used as the starting point for the three-dimensional numerical model developed in this research. Chapter 3 summarizes the 2-D method of modeling the effects on subionospheric VLF propagation of localized ionospheric disturbances that has been used in previous studies.

Chapter 4 presents the formulation of the three-dimensional modeling of the scattering effects of a finite-sized disturbance in the lower ionosphere. Using this formulation, VLF scattering properties of typical lower ionospheric disturbances that are expected to be

induced by lightning-induced electron precipitation (LEP) are explored. Among the properties that were revealed as a result of this analysis are the following, which:

- The scattering from typical disturbances is generally insensitive to differences in the conductivity of the ground underneath it.
- The scattering is sensitive to differences in the altitude profile of electron density within the disturbed region.
- For typical disturbances, and for a variety of disturbance sizes, most of the wave energy is scattered into a fairly narrow ($\pm 20^\circ$) angular range about the forward scatter direction. This result implies that the effects of disturbances of this type located beyond ~ 200 km transverse to the GCP can in most cases be neglected.

Chapter 5 describes a simple application of the 3-D scattering model to the case of single mode WKB (Wentzel, Kramers, and Brillouin) propagation over a homogeneous surface; in particular, a long, all-sea-based path. Realistic values for the ground conductivity, ambient ionospheric electron density, disturbed electron density versus altitude profile, and dimensions and shape of the disturbance are used to investigate the effect these disturbances have on the received signal. The results are consistent with experimental data having similar geophysical characteristics to those used in the model calculations. Another result which was revealed in the single mode analysis was the following:

- The ratio of the change in amplitude of the received signal to the change in phase is strongly dependent on the altitude profile of ionization in the disturbed region, in particular to the depth of penetration of the enhancement in altitude.

Chapter 6 explains the extension of the single mode WKB technique to a three-dimensional multiple mode WKB scatterer method. Mode conversion along the propagation paths to the receiver, and to and from the scatterer are calculated. Hence, a more realistic, horizontally (x and y directions) inhomogeneous ground or ionospheric boundary can be modeled. The methodology used to accomplish this is described. Application of this method to a realistic path on the Earth is also found to produce results consistent

with experimental data. Other results that were revealed as a result of the analysis were as follows:

- Again, the scattering effect of the disturbance is sensitive to differences in the disturbed electron density altitude profile. In particular, the ionospheric 'conductivity' with altitude is the controlling parameter, rather than just the electron density.
- The dependence of amplitude and phase changes on location of the disturbed region with respect to the great circle path shows that the effects of disturbances at distances greater than ~ 200 km transverse to the GCP are negligible.

The importance of the location of the receiver with respect to the signal strength versus propagation distance pattern was elaborated, and for the multiple mode case in particular, the sensitivity to changes in the signal amplitude and phase of a receiver located at or near a deep null in the signal strength is illustrated. Consequently, another simple result of the model is:

- The altitude profile of the ambient electron density along the propagation path can significantly affect the signal strength pattern and thus the response at the receiver to a given disturbance.

Chapter 7 concludes with a summary of the contributions of the research and a number of suggestions for further investigation.

Chapter 2

Overview of VLF Waveguide Theory in the Earth-Ionosphere Waveguide

This chapter gives a brief description of the important aspects of the theory of VLF wave propagation within the Earth-ionosphere waveguide. The basic geometry of the problem is depicted in Figure 2.1.

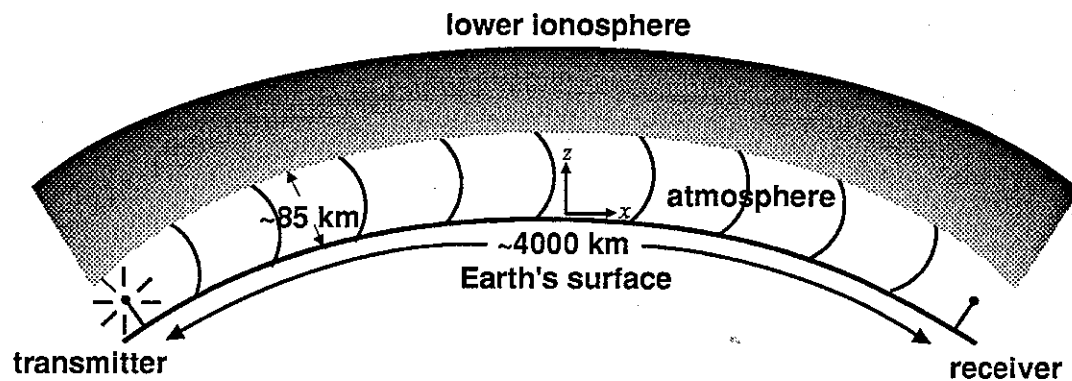


Figure 2.1: Geometry of the Earth-ionosphere VLF waveguide problem.

In very simplistic terms we can describe the system in the following way. The source of the wave signal is a transmitter that applies an oscillating electric voltage in the VLF frequency range to the terminals of an antenna. While the radiating antennas of most VLF transmitters consist of large and elaborate structures [Watt, 1967], typically, the antennas

used are equivalent to a vertical monopole (oriented perpendicularly to the ground surface, i.e., in the z direction of Figure 2.1) with a ground plane. (The Siple Station antenna is one exception, being a horizontal dipole, oriented parallel to the ground surface, lying on top of a 2-km thick ice sheet [Helliwell and Katsufrakis, 1974; Raghuram *et al.*, 1974].) Part of the energy of the oscillating electrical current is converted by the antenna into an electromagnetic wave which radiates from the antenna structure and propagates away from it. Most of the radiated energy for VLF frequencies is reflected back and forth and guided by the Earth and ionosphere boundaries. For a single vertical dipole, the wave energy radiates equally in all horizontal directions; i.e., the radiation pattern is radially symmetric about the antenna. A small amount of the wave energy can penetrate the ionospheric boundary and escape upwards to the upper ionosphere and magnetosphere. (See Helliwell [1965].) This represents one of the loss mechanisms of the waveguide. After the guided wave energy has propagated for some distance within the waveguide, it arrives at the receiver antenna (refer to Figure 2.1) which converts a portion of the wave energy back into an oscillating electrical current, which is processed, measured, and recorded by the receiver instrumentation.

2.1 Theoretical Considerations

The portion of the foregoing simple explanation that is of most importance in this research is the propagation of the electromagnetic wave. In particular, it is important to describe how the electromagnetic wave energy is transformed as it propagates within the, in our case Earth-ionosphere, waveguide. The most general formulation of electromagnetic waves is in terms of a set of four physical laws known as Maxwell's equations [Maxwell, 1873], which uniquely describe the (macroscopic) electromagnetic field. The differential form of these equations is given in Equation 2.1.

$$\begin{aligned}\nabla \cdot \mathbf{D} &= \rho, \\ \nabla \cdot \mathbf{B} &= 0, \\ \nabla \times \mathbf{H} &= \mathbf{J} + \frac{\partial \mathbf{D}}{\partial t},\end{aligned}\tag{2.1}$$

$$\nabla \times \mathbf{E} = -\frac{\partial \mathbf{B}}{\partial t}$$

where

\mathbf{E} is the total electric field,

\mathbf{H} is the total magnetic field,

$\mathbf{D} = \epsilon \mathbf{E}$,

$\mathbf{B} = \mu \mathbf{H}$,

ϵ is the permittivity of the medium,

μ is the permeability of the medium, and

\mathbf{J} is the current density.

The solution of these equations gives the electric and magnetic fields in the region for which they are solved. It is these fields that can be measured by the receiver and which are affected by the disturbances in the regions through which they propagate (such as the lower ionospheric type studied in this research). Therefore, Maxwell's equations must be solved for \mathbf{E} and \mathbf{H} , given the Earth-ionosphere waveguide conditions.

There are basically two methods for solving this type of problem: the geometrical "ray" theory, and the waveguide "mode" theory (these modes are also referred to as *eigenmodes*). The choice of which is best to use depends principally on the frequency of the signal and the distance the signal propagates. (See also *Wait [1964a]*.)

2.1.1 Ray Theory

Using the principles of geometric optics, the ray, or wave-hop, method traces every possible discrete ray path that completes an integral number of reflections, or "hops", from the Earth to the ionosphere and back to the Earth again, between the transmitter and the receiver. Figure 2.2 shows the first, second, and third order ray paths. Theoretically, there

are an infinite number of possible, discrete, paths between the transmitter and the receiver. However, the higher the order of the ray path, the more nearly vertical is the angle of incidence on the ionosphere. Due to the higher absorption and/or transmission into the ionosphere of such rays upon reflection at the ionospheric “boundary”, their contribution towards the total signal level at the receiver becomes less and less significant. Also, the overall path length of higher order ray paths becomes much longer and thus the field strength of such rays falls off more than for the lower order rays. The result is that only a finite number of low order rays are needed to calculate the total signal at the receiver [Davies, 1966; Cotton, 1989; Wolf, 1990].

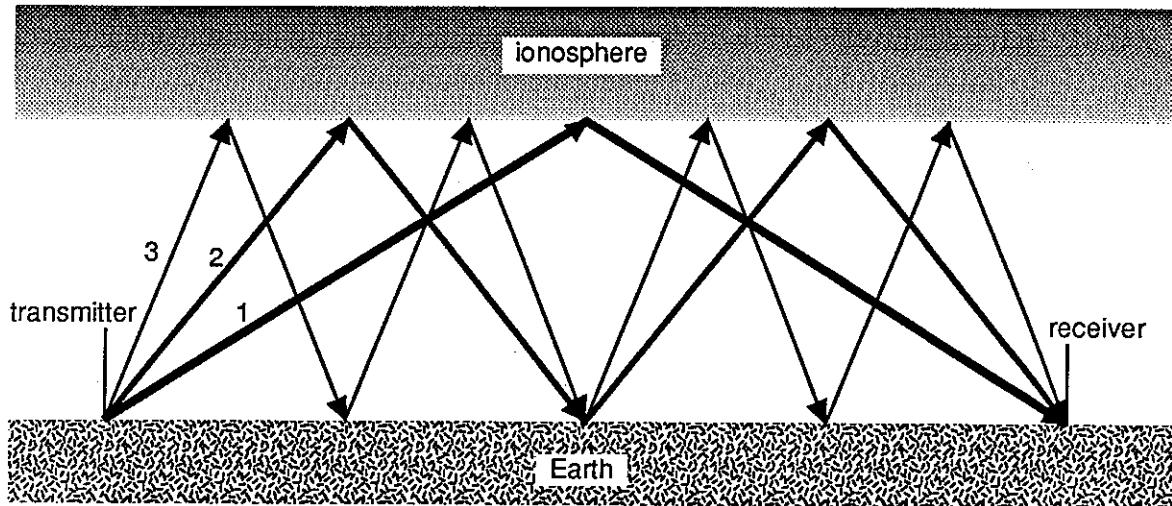


Figure 2.2: Possible discrete ray paths that complete an integral number of “hops” between the transmitter and the receiver. The first, second, and third order ray paths are indicated.

For very short (< 500 km) propagation paths, relatively few ray paths are needed to calculate the received signal. Also, for higher frequencies (LF and higher), a large number of waveguide modes are required to describe the wave structure, and thus, the ray method becomes the method of choice. However, the ray method becomes inconvenient for calculation purposes for long paths because many ray paths of relatively low attenuation are possible between transmitter and receiver. Also, for each separation distance between

the transmitter and the receiver there is a unique ray path geometry, which must be recalculated each time the transmitter-receiver path length is changed [Morfitt and Shellman, 1976].

2.1.2 Mode Theory

Another way to represent electromagnetic wave energy as it propagates in a waveguide is in terms of a sum of an infinite series of discrete waveguide "modes". A propagation mode has been defined as "a form of propagation of waves that is characterized by a particular field pattern in a plane transverse to the direction of propagation, which field pattern is independent of position along the axis of the guide" [Davies, 1966]. These waveguide modes can be found by solving Maxwell's equations (Equations 2.1) given the waveguide boundary conditions.

In general, in the VLF frequency range of interest here, and for the Earth-ionosphere waveguide, the higher order modes have a greater spatial attenuation rate versus propagation distance. (The 'order' of a waveguide mode is typically determined by the number of maxima and minima in the transverse vertical field pattern.) Also, as the mode order becomes very large, the amplitudes of those modes initially excited by the transmitter antenna become increasingly small. Thus, for relatively long paths, only a relatively small number of modes are required to describe the propagating waveform at VLF frequencies.

Another factor is that as the frequency (and/or the waveguide height, measured in wavelengths) decreases, fewer modes are needed to describe the propagating waveform. At the low end of the VLF band, only one to four modes are required for typical propagation path lengths. At 50 kHz, as many as 30 modes may be necessary in some cases [Morfitt and Shellman, 1976]. Nevertheless, these factors, along with the need to recalculate the ray path geometry every time the transmitter-receiver distance is changed (if the ray method is used) leads to the waveguide mode method being the preferred method for calculating VLF wave propagation along typical transmitter-receiver paths. In this work, we rely on the waveguide mode theory of VLF propagation which is described in some detail in the next two sections.

2.2 Overview of Waveguide Mode Theory

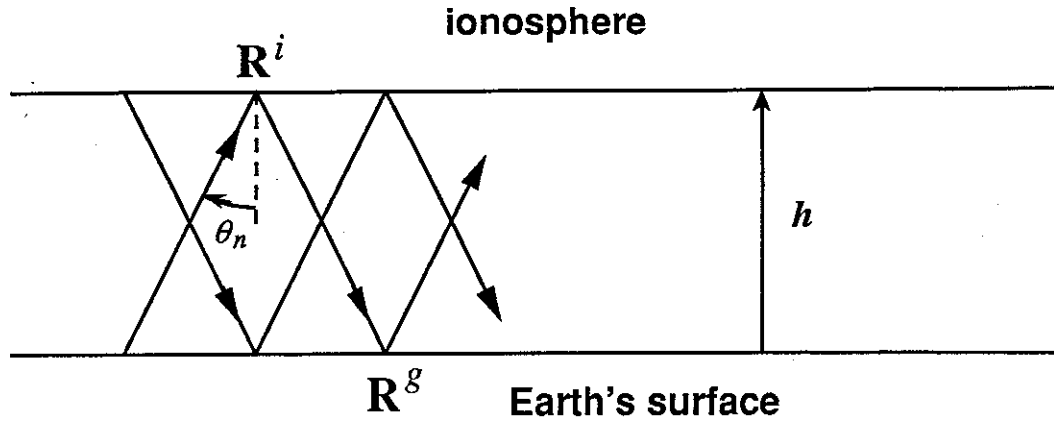


Figure 2.3: Two superposed plane waves propagating in a flat, infinitely wide waveguide with parallel, sharply-defined boundaries.

Waveguide mode theory can most easily be visualized by assuming that the waveguide is flat, infinitely wide, and has parallel, sharply-defined boundaries (as shown in Figure 2.3). It can be shown [Budden, 1961; Wait, 1970; Ramo *et al.*, 1984] that each waveguide mode can be found by superposing two plane waves, which reflect back and forth between the two waveguide boundaries, propagating at particular angles of incidence θ_n (see Figure 2.3). Solving Maxwell's equations for these two superposed waves for a series of θ_n yields an infinite sum of waveguide modes (some of which may be non-propagating or “evanescent” modes given the proper waveguide boundary conditions). If this same approach is used for a waveguide with spherical boundaries that are concentric, Maxwell's equations can again be solved to yield an electric field \mathbf{E} and a magnetic field \mathbf{H} whose components are each functions of $\psi(r, \vartheta)$, an infinite sum of rather complicated spherical wave functions [Wait [1970], Chapter 6]

$$\psi(r, \vartheta) = \sum_{n=1}^{\infty} D_n z_n(kr) P_n(-\cos \vartheta) \quad (2.2)$$

where

r, ϑ are spherical coordinates,

n , an integer, is the mode number,

ν is a complex value related to n (See Wait [1970], Chapter 6.),

D_ν are the mode coefficients,

z_ν are sums of Hankel functions of the first and second kind of order $\nu + \frac{1}{2}$,

$k = \omega/v$,

v is the phase velocity of the wave in the medium,

$\omega = 2\pi \times$ the wave frequency, and

P_ν are Legendre functions.

Wait [1970] showed that under undisturbed ionospheric conditions, with the Earth and the ionosphere taken to be a spherically concentric waveguide, and with homogeneous conditions along the entire path, Equation 2.2 can be simplified using asymptotic expansions to give the total vertical electric field E_{total} at a great circle path (GCP) distance d (\gg a wavelength) from the transmitter in the form

$$E_{total}(d) \simeq \frac{1}{\sqrt{|\sin(d/R_E)|}} \sum_n^\infty A_n^{T,R} e^{-ik_0 S_n d} \quad (2.3)$$

where

n is the mode number,

$i = \sqrt{-1}$,

$S_n = \sin \theta_n$, and is equivalent to the complex index of refraction for mode n , and thus determines the attenuation and phase velocity of that mode. In the general case, S_n is a function of the waveguide properties at each point along the propagation path.

θ_n is the complex-valued "angle of incidence" of each mode on the ionosphere,

R_E is the radius of the Earth,

$k_o = 2\pi/\lambda_o$ where λ_o is the free space wavelength of the signal, and

$A_n^{T,R}$ is a complex-valued function which includes the excitation and the height-gain factors at the transmitter and receiver and is dependent only on conditions at the transmitter and receiver locations.

The factor

$$\frac{1}{\sqrt{|\sin(d/R_E)|}}$$

represents a cylindrical spreading factor on a spherical surface and is a first order approximation resulting from the asymptotic expansions of the Legendre functions of Equation 2.2. (Due to this approximation, Equation 2.3 is not valid at the antipode of the transmitter.)

All of the variables in Equation 2.3 are functions only of the properties of the waveguide at the transmitter or receiver locations, or of the transmitter and receiver antennae, except for S_n .

The factor $A_n^{T,R}$ can be written out more completely as

$$A_n^{T,R} = K T_n R_n \quad (2.4)$$

where

$K = a\sqrt{Pf}$; a is a constant coefficient; P is the radiated power; f is the signal frequency;

$$\begin{aligned} T_n &= \sum_{j=1}^3 t_j \Lambda_{j,n}^T G_{j,n}^T(z) \\ R_n &= \sum_{j=1}^3 r_j \Lambda_{j,n}^R G_{j,n}^R(z) \end{aligned} \quad (2.5)$$

and

$j = 1, 2, 3$ represent the three dimensional coordinates x, y , and z ;

t_j, r_j are factors which account for the orientation of the transmitter or receiver antenna, respectively;

$\Lambda_{j,n}^{T,R}$ are the “initial excitation” factors for each mode for the transmitter or receiver antennas, respectively [Budden, 1961]. These factors represent the relative amount of each mode that each component of the antenna excites (or by reciprocity, receives). (The initial excitation factor Λ as written here is equivalent to $\sqrt{\Lambda}$ as defined in *Ferguson and Snyder* [1980].);

$G_{j,n}^{T,R}(z)$ are known as the “height-gain” factors for each mode for the transmitter or receiver, respectively. They represent the relative amplitude and phase of each of the three components of each waveguide mode as a function of altitude, at the transmitter or receiver.

The S_n are functions of the waveguide properties at each point along the propagation path, and must be determined at each point where the Earth or ionosphere boundary properties change. Equation 2.3 is essentially a two-dimensional formulation for a waveguide whose characteristic properties are constant throughout the propagation path (i.e., homogeneous). There is no dependency on changes in the y direction (transverse to the GCP). However, Equation 2.3 does take into account the spherical curvature of the waveguide.

2.2.1 Inhomogeneous Waveguides

WKB Approximation

If the waveguide properties are not homogeneous along the direction of propagation, then a more generalized version of Equation 2.3 is necessary. If the changes in the waveguide properties are “slowly varying”, i.e., the variations in the waveguide properties over distances of the order of a wavelength along the propagation direction are small, then

the energy of each mode does not contribute significantly to that of any of the other modes. The assumption of slow variations is known as the WKB (Wentzel, Kramers, and Brillouin) approximation, and when this approximation holds, each mode propagates independently of the other modes [Wait, 1962; Ferguson and Snyder, 1980]. Equation 2.3 can be generalized to account for this by noting that the angles of incidence θ_n are dependent on the waveguide properties at each point along the propagation path and are therefore functions of x . Thus, $S_n(x) = \sin[\theta_n(x)]$ is also a function of x and therefore Equation 2.3 can be generalized by making the substitution [Wait, 1964b]:

$$S_n \rightarrow \int_0^d S_n(x) dx. \quad (2.6)$$

Non-WKB Inhomogeneous Waveguides

If significant changes in the ionosphere or ground boundary properties occur over a shorter distance along the propagation path than a wavelength, the WKB approximation breaks down, and some of the wave energy of a mode may transfer to other modes. This effect is known as mode conversion, and must be accounted for in determining the total magnetic or electric field arriving at the receiver in non-WKB inhomogeneous waveguides. In order to numerically calculate signal strengths in the Earth-ionosphere waveguide, a method to approximate the waveguide and calculate the mode conversion that occurs along typical propagation paths is used in this work and is discussed in the next chapter.

2.3 Determination of the Mode Refractive Index S_n (VLF Waveguide Mode Theory)

The complex quantities S_n characterize the propagating modes which can be found by superposing two plane waves propagating at various angles of incidence θ_n on the ionosphere as shown in Figure 2.3. Values for S_n can be computed using the mode theory of VLF propagation in the Earth-ionosphere waveguide [Budden, 1961; Wait, 1970]. In this theory, the energy within the waveguide is considered to be partitioned among a series

of modes. Each mode is associated with one of a discrete set of angles of incidence θ_n of the waves on the ionosphere, for which constructive interference occurs and energy propagates away from the source.

To more easily visualize what is occurring, we consider again the case of the flat, infinitely wide waveguide with sharply defined boundaries (Figure 2.4). The ionosphere boundary has a reflection coefficient $R^g(\theta_n)$ and the ground surface has a reflection coefficient $R^i(\theta_n)$. Upgoing waves will reflect off the upper boundary to produce downgoing waves, which are in turn reflected from the lower boundary and give rise to more upgoing waves. In order to interfere constructively, the twice-reflected upgoing waves must be in phase with the original upgoing waves, and thus must have suffered a net phase change of $2\pi m$ radians (where m is an integer). This requirement, which satisfies the boundary conditions at both boundaries, yields the mode, or resonance, condition for a self-consistent mode [Budden, 1961; Wait, 1970]. If we let F_0 represent the upgoing wave and F_1 the twice-reflected upgoing wave, the mode condition gives

$$|F_1|e^{-i2\pi m} = |F_0|R^i(\theta_n)R^g(\theta_n)e^{-2ikh\sin\theta_n} \quad (2.7)$$

Since $|F_1| = |F_0|$ and m is an integer, Equation 2.7 reduces to

$$R^i(\theta_n)R^g(\theta_n)e^{-2ikh\sin\theta_n} = 1. \quad (2.8)$$

Due to the effect of the Earth's magnetic field on the plasma in the ionosphere, the plasma is an anisotropic medium, requiring that the reflection coefficients be described in matrix form. Also, because of various loss mechanisms in both the ground and the ionosphere, the elements of the reflection coefficients are complex (the imaginary part mathematically accounting for the ohmic losses in the calculations). Thus, Equation 2.8 becomes [Morfitt and Shellman, 1976]

$$|R_h^i(\theta_n)R_h^g(\theta_n) - \mathbf{I}| = 0 \quad (2.9)$$

where

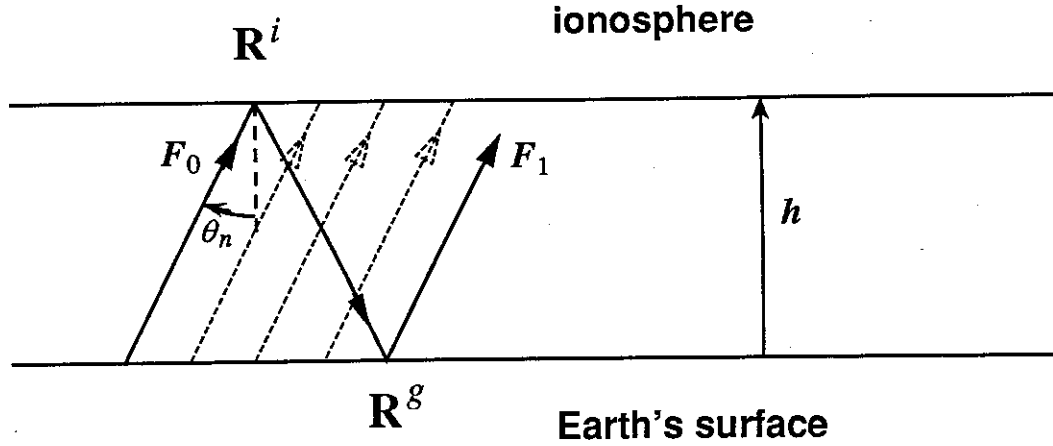


Figure 2.4: A flat, infinitely wide waveguide with sharply defined boundaries showing the reflection angles and geometry of the mode or resonance condition.

$\mathbf{R}_h^i(\theta_n)$ is the complex-valued reflection coefficient matrix looking up into the ionosphere from height h

$$\mathbf{R}_h^i(\theta_n) = \begin{bmatrix} {}_{\parallel}R_{\parallel}^i(\theta_n) & {}_{\perp}R_{\parallel}^i(\theta_n) \\ {}_{\parallel}R_{\perp}^i(\theta_n) & {}_{\perp}R_{\perp}^i(\theta_n) \end{bmatrix}, \quad (2.10)$$

$\mathbf{R}_h^g(\theta_n)$ is the complex-valued reflection coefficient matrix looking down towards the ground from height h

$$\mathbf{R}_h^g(\theta_n) = \begin{bmatrix} {}_{\parallel}R_{\parallel}^g(\theta_n) & 0 \\ 0 & {}_{\perp}R_{\perp}^g(\theta_n) \end{bmatrix}, \quad (2.11)$$

and

\mathbf{I} is the identity matrix

$$\mathbf{I} = \begin{bmatrix} 1 & 0 \\ 0 & 1 \end{bmatrix}. \quad (2.12)$$

Since the elements of the reflection coefficient matrices are complex, the mode solutions are complex also. These mode solutions consist of the set of "angles of reflection" θ_n ,

also called *eigenangles*, each representing one waveguide mode. This set of complex eigenangles, θ_n , constitute the solutions to the “modal equation” (Equation 2.9).

Due to the anisotropy of the ionosphere, a wave which has a component of its electric field perpendicular to the plane of incidence, for example E_y (the plane of incidence is the x - z plane), can, upon reflection, give rise to a wave with electric field components polarized both perpendicular and parallel to the plane of incidence. A component of the electric field which is parallel to the plane of incidence can also give rise to both polarizations in the reflected wave. Hence, in the matrix element notation (e.g., ${}_{\perp}R_{\parallel}^i(\theta_n)$), the pre-subscript (\perp) indicates the polarization of the incident electric field component and the post-subscript (\parallel) indicates the polarization of the reflected electric field component. The ground surface is considered to be homogeneous and isotropic in this model, leading to a diagonal matrix ($R_h^g(\theta_n)$) in Equation 2.9. (However, see *Galejs* [1972] for a description of equivalent anisotropy in a multilayer ground model.) Therefore, in the isotropic case, perpendicularly polarized incident wave components give rise only to perpendicularly reflected waves, and similarly for incident wave components having parallel polarization.

The elements of the two reflection coefficient matrices are determined by integration of differential equations which describe the reflection coefficients as functions of the properties of the Earth and the ionosphere ‘boundaries’ at a given location [*Budden*, 1955, 1961; *Sheddy*, 1968].

Once the eigenangles θ_n that satisfy Equation 2.9 for the appropriate waveguide boundary conditions are determined, the quantities S_n for each mode n can be obtained by taking the (complex-valued) sines of the respective eigenangles [*Wait*, 1970].

2.3.1 Numerical Solutions of the Mode Equation: MODEFNDR

Since the solutions to the mode equation (Equation 2.9) cannot, in general, be determined in closed form, we used the computer program “MODEFNDR” [*Morfitt and Shellman*, 1976; *Shellman*, 1986; *Ferguson and Snyder*, 1987] developed by the Naval Ocean Systems Center (NOSC) to obtain values for S_n numerically. The input to this program,

which accounts for the curvature of the Earth, consists of arbitrarily assigned electron and ion density distributions with altitude, collision frequency versus altitude profiles, the local vector magnetic field, ground conductivity, and ground permittivity. Using these quantities, MODEFNDR determines the elements of the ionospheric and ground reflection coefficient matrices (R_h^i, R_h^g) and solves for the θ_n which satisfy Equation 2.9.

Ionospheric electron and ion density versus altitude profiles can be input either via an exponential equation describing the profile, or by means of a table containing a series of altitude values and the corresponding density values, for non-exponential profiles. Ionospheric collision frequency profiles can also be input either via an exponential equation or by explicitly entering a table of values versus altitude.

Generally, values for all the important wave and boundary properties can be input to MODEFNDR. Both the magnitude and direction of the magnetic field are input, as well as the wave frequency, and the altitude of the transmitter and receiver above the ground boundary. Also, the masses of the different ion species can be specified by the user. However, in the currently implemented form of the program, both the transmitter and receiver antennas are assumed to be electric dipoles of arbitrary orientation, and the ground boundary is specified by only two parameters: its conductivity and its relative dielectric constant (permittivity). There is as yet no capability to account for variations in the ground conductivity or permittivity versus depth (which becomes more important for the lower end of the VLF band, where the wave penetration into the ground, or skin depth, becomes increasingly large). Nor does MODEFNDR itself calculate variations in conductivity or dielectric constant versus frequency. Finally, no mechanism has been provided to indicate changes in the altitude (above some average sea level) of the ground surface along the propagation path.

Using these parameter values, MODEFNDR searches a region of the complex plane, specified either explicitly or by inputting a maximum desired modal attenuation rate (See section 2.4.2), for all θ_n which satisfy Equation 2.9. In the process of determining the reflection coefficients of the ionosphere, MODEFNDR calculates an effective reflection height. From the resultant values of the reflection coefficient matrix elements and the modal eigenangle solutions, the attenuation rate, phase velocity, initial excitation and

“height-gain” factors, and the polarization mixing ratio for each mode are calculated [Pappert and Shockey, 1971; Morfitt and Shellman, 1976]. From these, the x , y , and z components of each mode’s electric and magnetic fields can be calculated versus altitude (i.e., $e_{j,n}(z)$ and $h_{j,n}(z)$). See Pappert and Hitney [1981]; Ferguson and Hitney [1987]. (One aspect of interest provided by the polarization mixing ratio, is an indication of whether a mode is mostly transverse magnetic (TM) in nature, mostly transverse electric (TE), or some mixture in between; i.e., whether a mode’s vector magnetic field is nearly perpendicular to the direction of propagation (TM modes), or whether the mode’s vector electric field is nearly perpendicular to the propagation direction (TE modes). Magnitudes > 1 indicate quasi-transverse magnetic (QTM) modes, whereas magnitudes < 1 indicate quasi-transverse electric (QTE) modes. The further from unity the polarization ratio is, the ‘purer’ is the character of the mode.)

2.4 Examples

2.4.1 Ideal (Perfectly Conducting) Waveguide Boundaries

To give some idea of what occurs in the Earth-ionosphere waveguide, we can roughly approximate it by treating the lower, or ground surface, boundary as a perfect electrical conductor and the upper, or ionosphere, boundary as a perfect magnetic conductor [Davies, 1966] (Figure 2.5a). The boundaries are flat, parallel, sharply-defined, and isotropic (and hence, the reflection coefficients are scalars). Thus, the lower boundary’s reflection coefficient is $R = 1$ and the upper boundary’s reflection coefficient is $R = -1$. Figure 2.5b shows the first 20 mode, or eigenangle, solutions for this simple case for a 25 kHz signal and a boundary separation of 85 km (which is roughly the effective waveguide height of the nighttime Earth-ionosphere waveguide). In this case, because there are no losses, the modes are either

- 1) purely propagating, represented by eigenangle solutions on the real axis,
- 2) or, purely attenuating, i.e., non-propagating or “evanescent” (below the “cut-off” angle), represented by solutions along the imaginary axis.

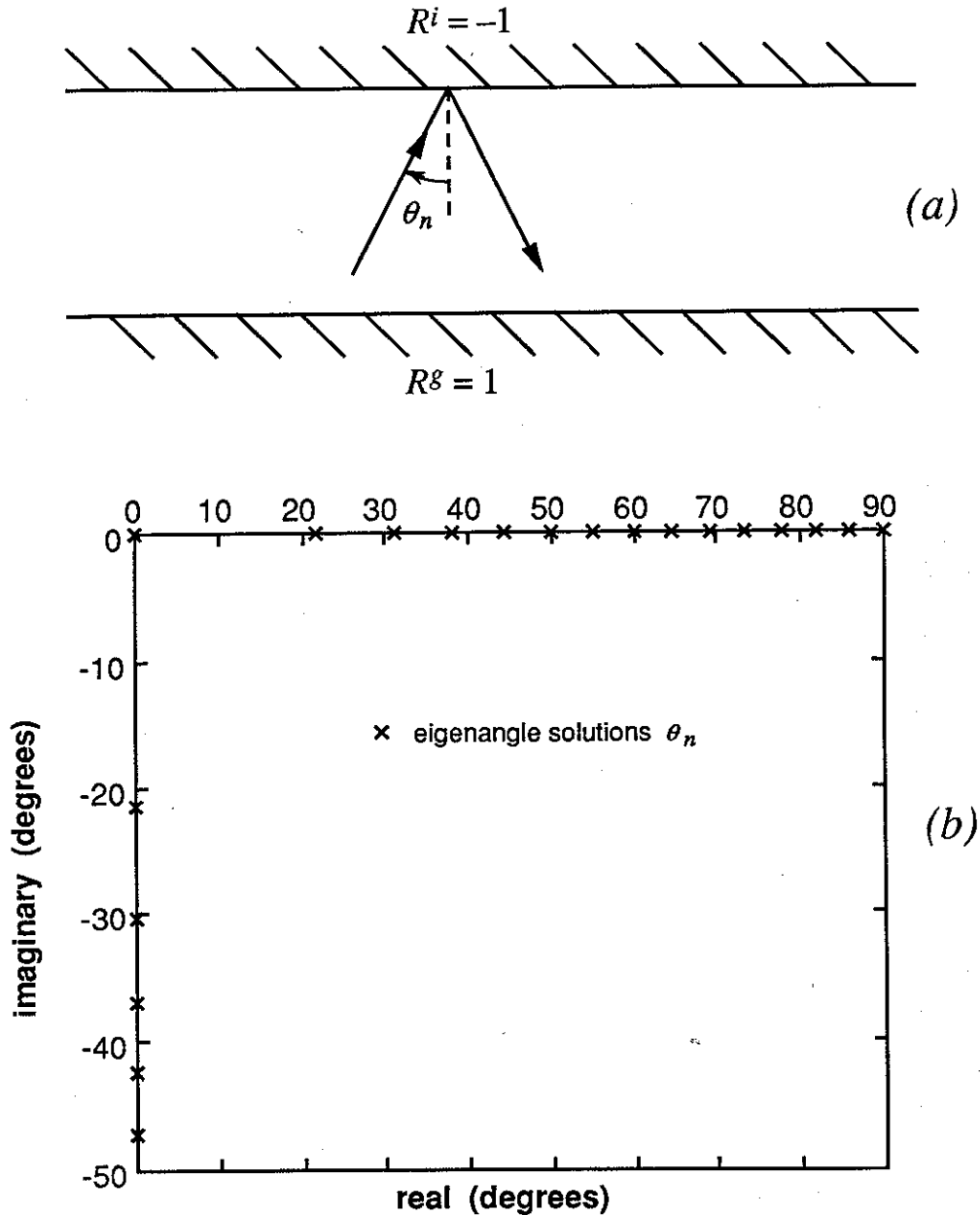


Figure 2.5: (a) Representation of the Earth-ionosphere waveguide as a waveguide with flat, parallel, sharply-defined, and isotropic boundaries. The Earth surface (or lower) boundary is treated as a perfect electric conductor ($R^g = 1$) and the ionospheric (or upper) 'boundary' is treated as a perfect magnetic conductor ($R^i = -1$). (b) The first 20 mode, or eigenangle, solutions for a 25 kHz signal propagating in the waveguide shown in Figure 2.5a assuming a boundary separation of 85 km.

2.4.2 “Real” Waveguide Boundaries

In the actual Earth-ionosphere waveguide, the boundaries are curved, are not perfectly conducting, and have complex, anisotropic reflection coefficients, as mentioned before. All of the modes attenuate as they propagate and are thus represented by eigenangles that are neither purely real nor purely imaginary, as shown in Figure 2.6. The eigenangles plotted in Figure 2.6*b* are mode solutions for a 25 kHz signal where the Earth-ionosphere waveguide boundaries consist of the typical nighttime ambient ionosphere shown in Figure 1.3 and a sea-water surface. Contours of attenuation (in dB/Mm) have been plotted in Figure 2.6*b* to illustrate the attenuation each eigenangle solution represents. The lowest order modes (those whose real part of their eigenangles are closest to 90 degrees) have relatively lower attenuation rates (< 10 dB/Mm) than most of the other modes, and thus become the dominant modes that play a role in the wave’s propagation after sufficient distance has been traversed. The ultimate dominance of any mode, however, depends on how strongly each mode is initially excited by the transmitter antenna; generally, all modes are not equally excited, initially. (See section 2.4.4.)

If we compare this case to the ideal case of Figure 2.5, we can see that there are no purely evanescent modes. However, some modes, particularly the higher-order modes, have increasingly large attenuation rates. This is shown in Figure 2.6*b* where we see that the two branches of eigenangle solutions head towards higher attenuation rate regions of the complex plane as their real part decreases towards zero degrees. (This is the same as the mode number increasing towards infinity.) Figure 2.6 illustrates graphically why VLF is used for long distance global communication and navigation; some of the lowest order modes have attenuation rates on the order of only 1 dB/1000 km.

The two “branches” seen in the locus of eigenangle solutions represent two different sets of modes; one set are quasi-transverse magnetic (QTM) and the other set are quasi-transverse electric (QTE). The reason that none of these modes is purely TM or purely TE is due to the anisotropy of the ionosphere which couples the parallel and perpendicular components of the propagating wave field, as compared to the perfectly conducting case where all the propagating modes are either purely TM or TE. (The difference between the TM and TE modes of section 2.4.1 cannot be distinguished in Figure 2.5 because all

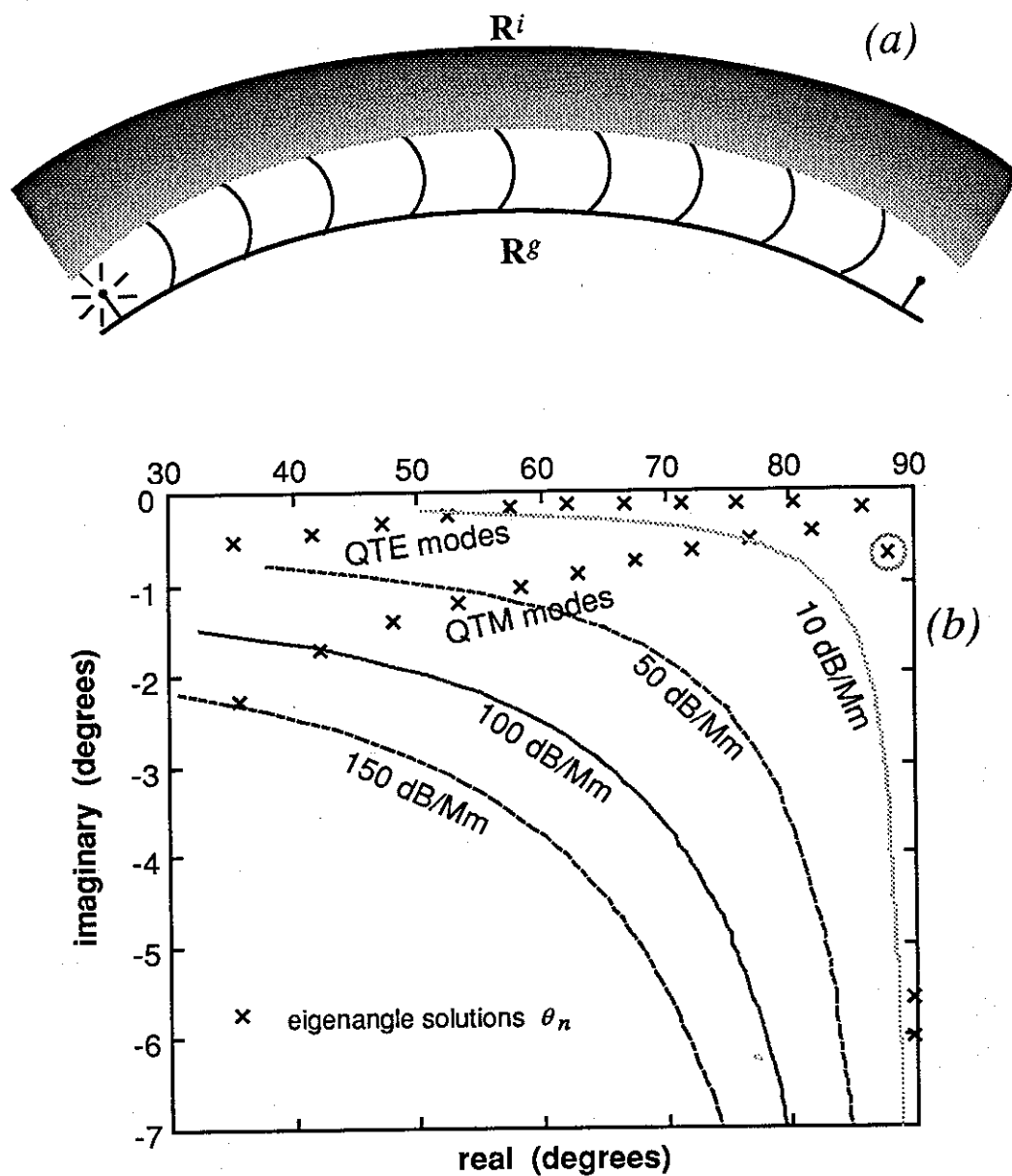


Figure 2.6: (a) Representation of the actual Earth-ionosphere waveguide including Earth curvature and the smoothly varying electron density of the ionospheric 'boundary'. (b) The first 24 mode or eigenangle solutions for a 25 kHz signal propagating in the Earth-ionosphere waveguide with the typical nighttime ambient ionosphere represented by Figure 1.3 and a sea-water Earth surface. Also plotted are contours of attenuation in dB/Mm.

of the propagating solutions lie along the real axis. The x , y , and z components must be examined to determine which of these are TM and which are TE.)

2.4.3 Field Strength versus Altitude

Each waveguide mode has a unique field strength profile versus altitude as shown in Figure 2.7 for one example mode. This figure shows the magnitude versus altitude of the three rectangular coordinate components of both the electric and magnetic fields of one of the modes in the example depicted in Figure 2.6. In this case, the mode illustrated is one of the lowest order modes (mode 3 according to MODEFNDR's mode numbering system, which happens to be mode QTM₂) and is the mode corresponding to the eigenangle with a circle drawn around it in Figure 2.6. (MODEFNDR's method of assigning a number to a mode consists of ordering all the eigenangle solutions in descending order according to their real part, starting with the mode closest to 90°. This method does not consistently assign the same number to a given mode independent of changes in the eigenangle solutions caused by changes in the waveguide boundary properties.)

We note that this mode is indeed mostly transverse magnetic because, even though there are finite amounts of all three electric field components (which is not the case for the ideal situation; see Figure 2.8.), there is almost no x component of the magnetic field; the magnetic field consists almost entirely of the transverse y and z components. It can be seen by the small but finite magnitude of several of the electromagnetic field components that continue upward in altitude beyond ~ 90 km, that a small amount of wave energy escapes into the ionosphere, and that the effective reflection height in this example is ~ 85 km below which the bulk of the wave energy resides. (See *Helliwell* [1965]; *Wait* [1970]; and *Budden* [1985] for discussion of what happens to the wave energy that penetrates the Earth-ionosphere interface and propagates into the ionosphere and magnetosphere.)

Once again, if we compare the real case to the ideal case (See Figure 2.8 for a plot of the magnitude of the components of the electric and magnetic fields as a function of height for the ideal TM₂ case depicted in Figure 2.5), we can see that the components are

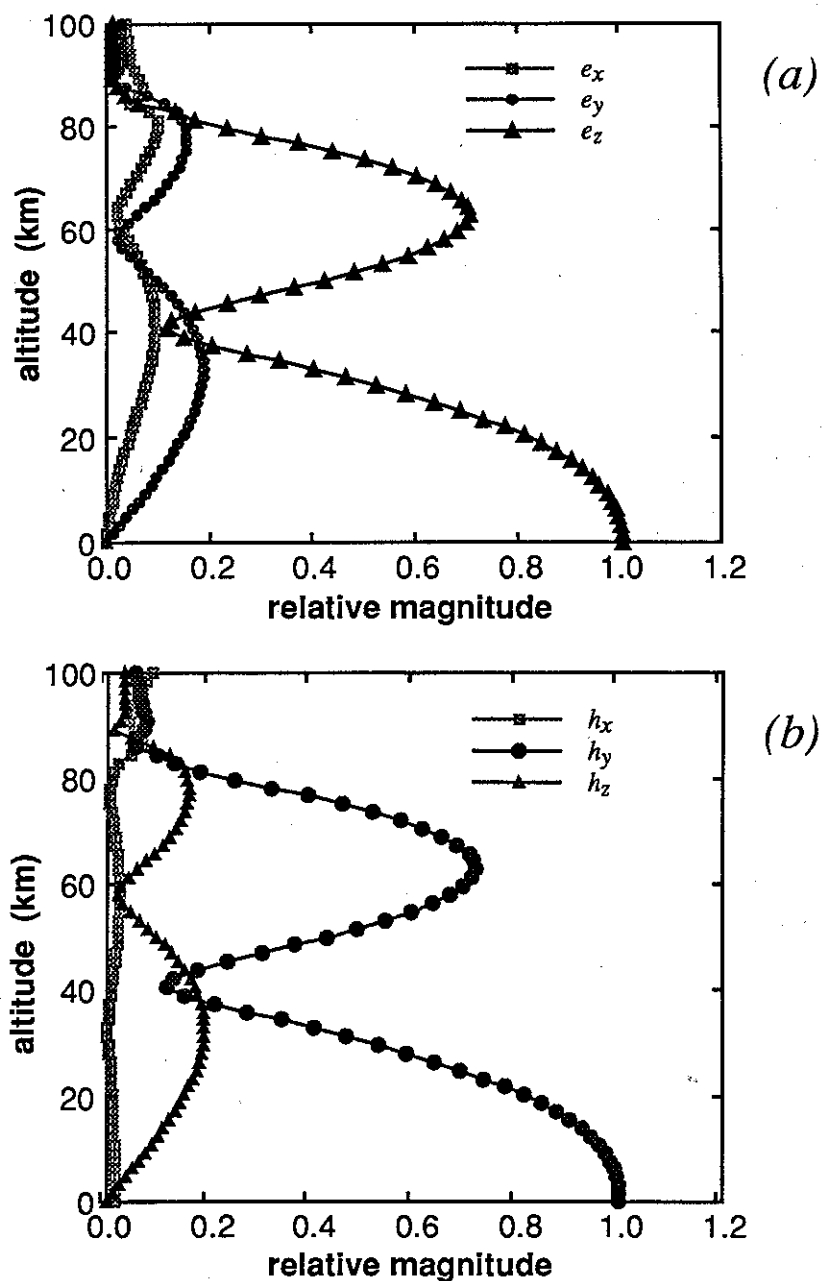


Figure 2.7: (a) Relative magnitude versus altitude of the three rectangular coordinate components of the modal electric field of mode QTM₂ for the example depicted in Figure 2.6. (b) The three components of the modal magnetic field corresponding to the electric field magnitudes shown in Figure 2.7a.

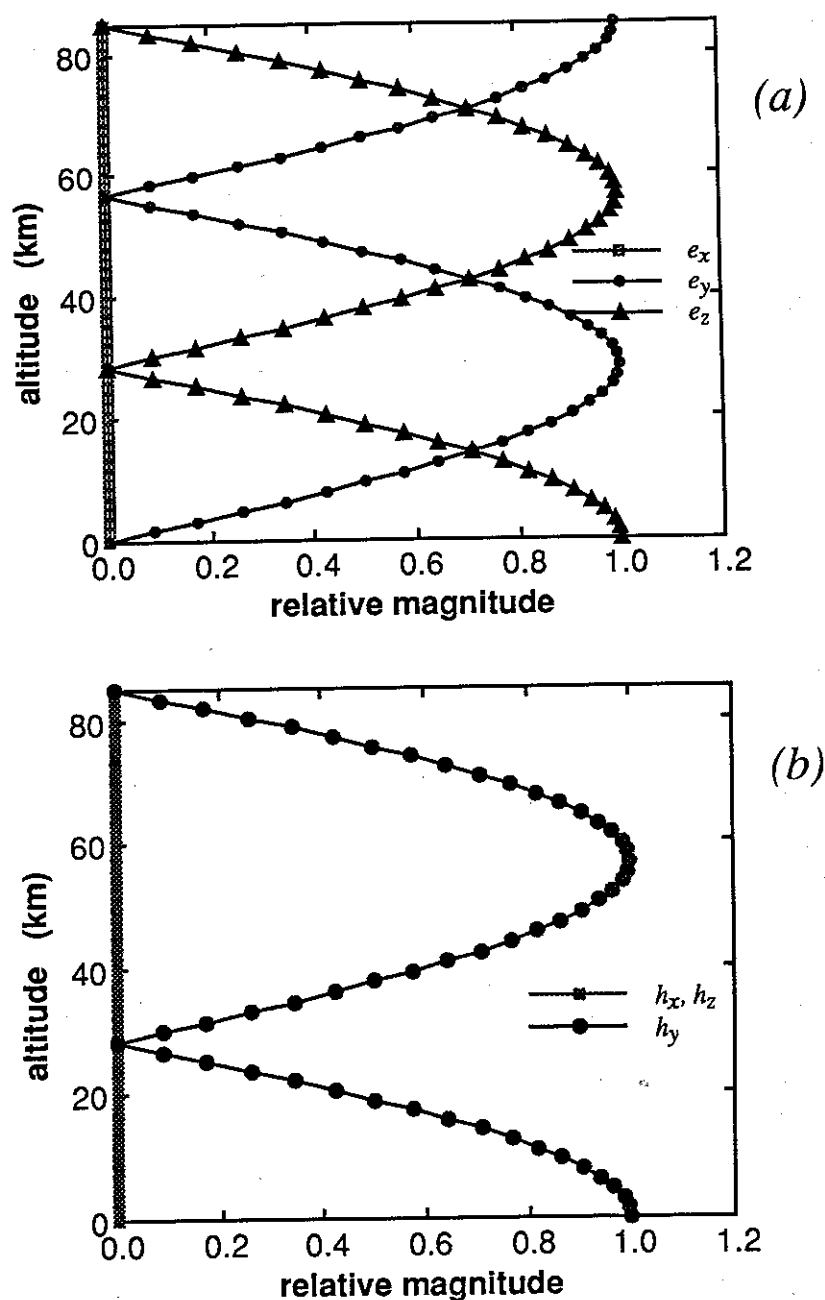


Figure 2.8: (a) Relative magnitude versus altitude of the three components of the modal electric field of mode TM_2 for the 'ideal' case depicted in Figure 2.6. (b) The corresponding magnetic field components for the 'ideal' case.

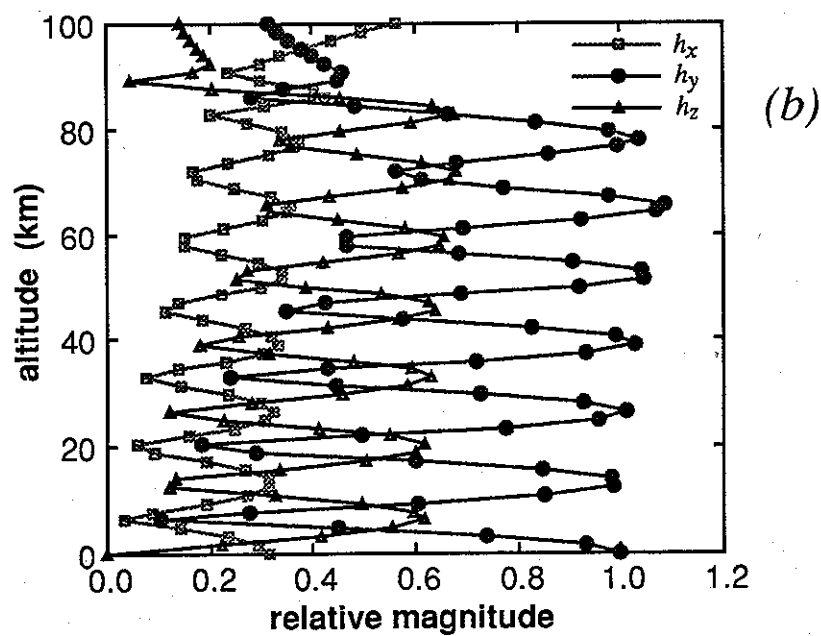
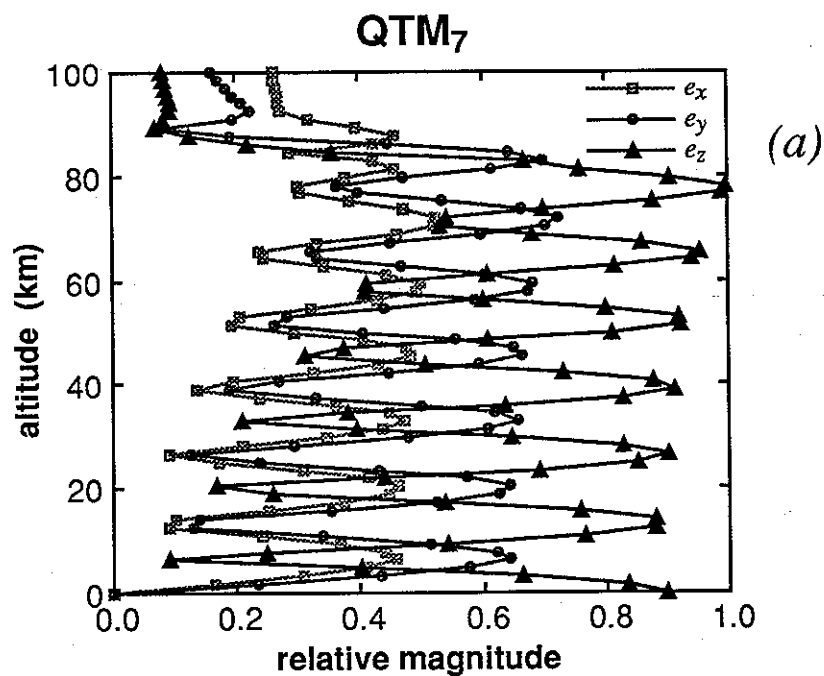
similar, but due to the coupling of the two polarizations, e_y and h_z are not everywhere zero and have finite magnitudes. We can also see that while the ground surface can be closely approximated by a perfect electric conductor (the value of all six components of the electric and magnetic fields at or near the ground are nearly the same as in the ideal case), the ionosphere does not behave like a perfect magnetic conductor. In the real case, all the components become very small in magnitude as they move into the lower ionosphere, whereas for an ideal $R = -1$ conductor, the x component of the electric field ($e_{x,3}$) has a maximum value at the upper boundary. An analogous situation occurs if we were to approximate the ionosphere using a perfect electric conductor ($R = 1$). Thus, the ionosphere cannot in general be treated as an ideal, perfectly conducting boundary.

Figure 2.9 shows examples of the component electric and magnetic field structure versus altitude for modes 13 and 14 (QTM₇ and QTE₇, respectively) for the same ambient nighttime conditions as in the previous figures. Higher order modes have more lobes versus altitude, the number of lobes corresponding to the subscript n used when indicating that the mode is of type QTM _{n} .

2.4.4 Initial Excitation versus Mode Number

Table 2.1 is a list of the first 24 modes of the example case discussed in the previous two sections. Along with the mode number, the magnitude of the initial excitation level (relative to the strongest mode excited) in dB, and the initial attenuation rate in dB/Mm, is given for each mode. Figures 2.10a and b show corresponding plots of both of these sets of values versus their mode number. The initial excitation values (i.e., $\Lambda_{j,n}^{T,R}$ in Equation 2.5) are obtained directly from MODEFNDR, which evaluates them based on the formulation of *Ferguson and Snyder* [1980], assuming, in this case, vertical electric dipoles.

We note that mode 3 (QTM₂) is the strongest mode excited at the transmitter followed closely by mode 5, but they do not have the lowest attenuation rates; modes 1, 2, and 4 have the lowest attenuation rates. However, the initial excitation levels of these modes are much lower than those of modes 3 and 5. Thus, at least initially and for quite some



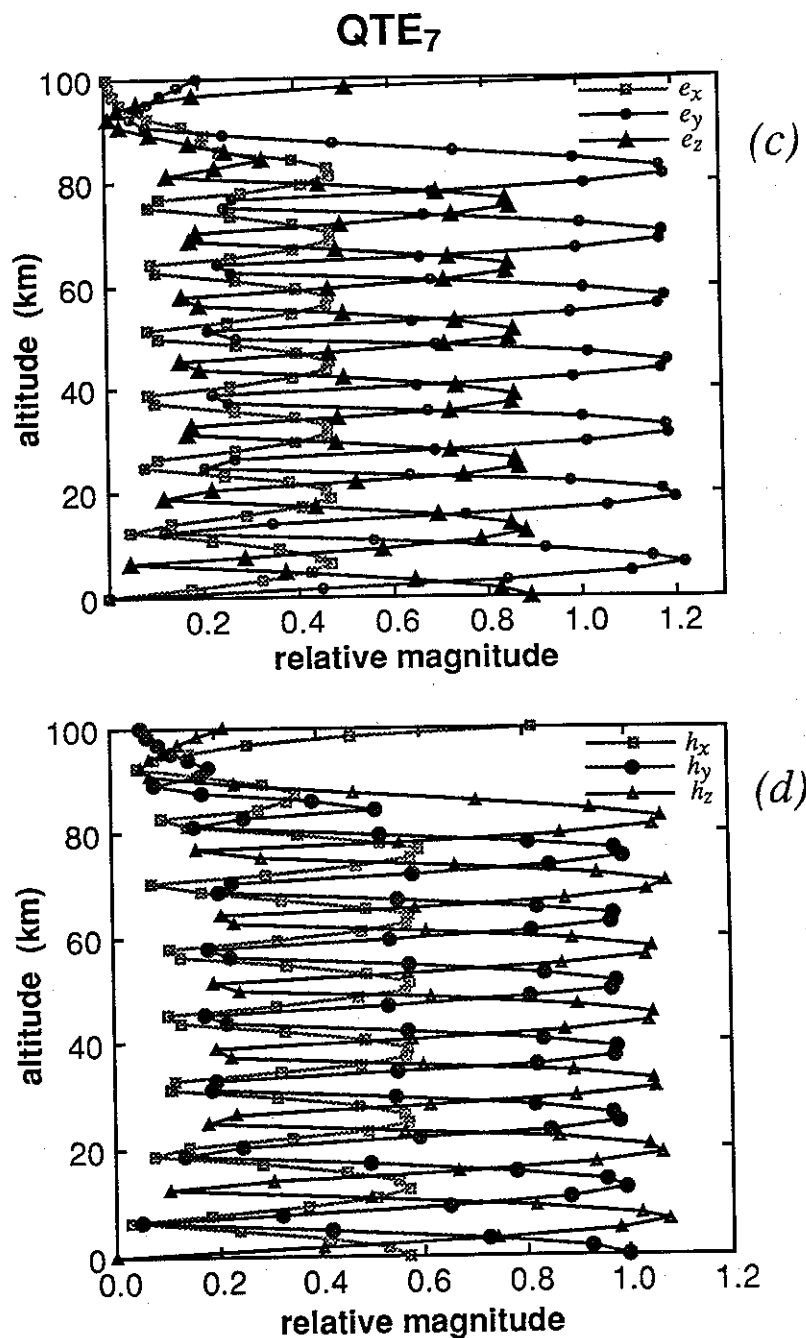


Figure 2.9: (a) Component electric field structure versus altitude of mode QTM₇ for the conditions depicted in Figure 2.6. (b) The corresponding magnetic field structure of mode QTM₇. (c) The component electric field structure of mode QTE₇. (d) The corresponding magnetic field structure of mode QTE₇.

Table 2.1: Relative initial excitation levels and attenuation rates for the first 24 modes of a 25 kHz signal above a sea-water surface for an ambient nighttime lower ionosphere.

Mode Type	Mode Number	Relative Initial Excitation Level (dB)	Attenuation Rate (dB/Mm)
QTE ₁	1	-39.8	-1.2
QTM ₁	2	-18.7	-1.1
QTM ₂	3	0.0	-2.1
QTE ₂	4	-25.1	-1.1
QTM ₃	5	-0.2	-5.1
QTE ₃	6	-24.4	-2.0
QTM ₄	7	-1.7	-9.5
QTE ₄	8	-20.4	-2.9
QTM ₅	9	-3.1	-15.5
QTE ₅	10	-16.6	-3.6
QTM ₆	11	-4.8	-23.2
QTE ₆	12	-13.8	-4.3
QTM ₇	13	-6.5	-32.6
QTE ₇	14	-11.9	-5.4
QTM ₈	15	-8.0	-43.7
QTE ₈	16	-10.8	-7.6
QTM ₉	17	-9.1	-57.1
QTE ₉	18	-10.1	-11.7
QTM ₁₀	19	-9.6	-74.6
QTE ₁₀	20	-10.0	-18.1
QTM ₁₁	21	-9.9	-100.8
QTE ₁₁	22	-11.0	-26.8
QTM ₁₂	23	-11.3	-147.0
QTE ₁₂	24	-13.7	-35.3

distance, modes 1, 2, and 4 do not contribute significantly to the total field of the wave. This illustrates how it can be possible for one or more modes to be initially excited so effectively that they remain the dominant modes for quite a long propagation distance, even if their attenuation rates are not as low as other modes excited less effectively by the transmitter antenna.

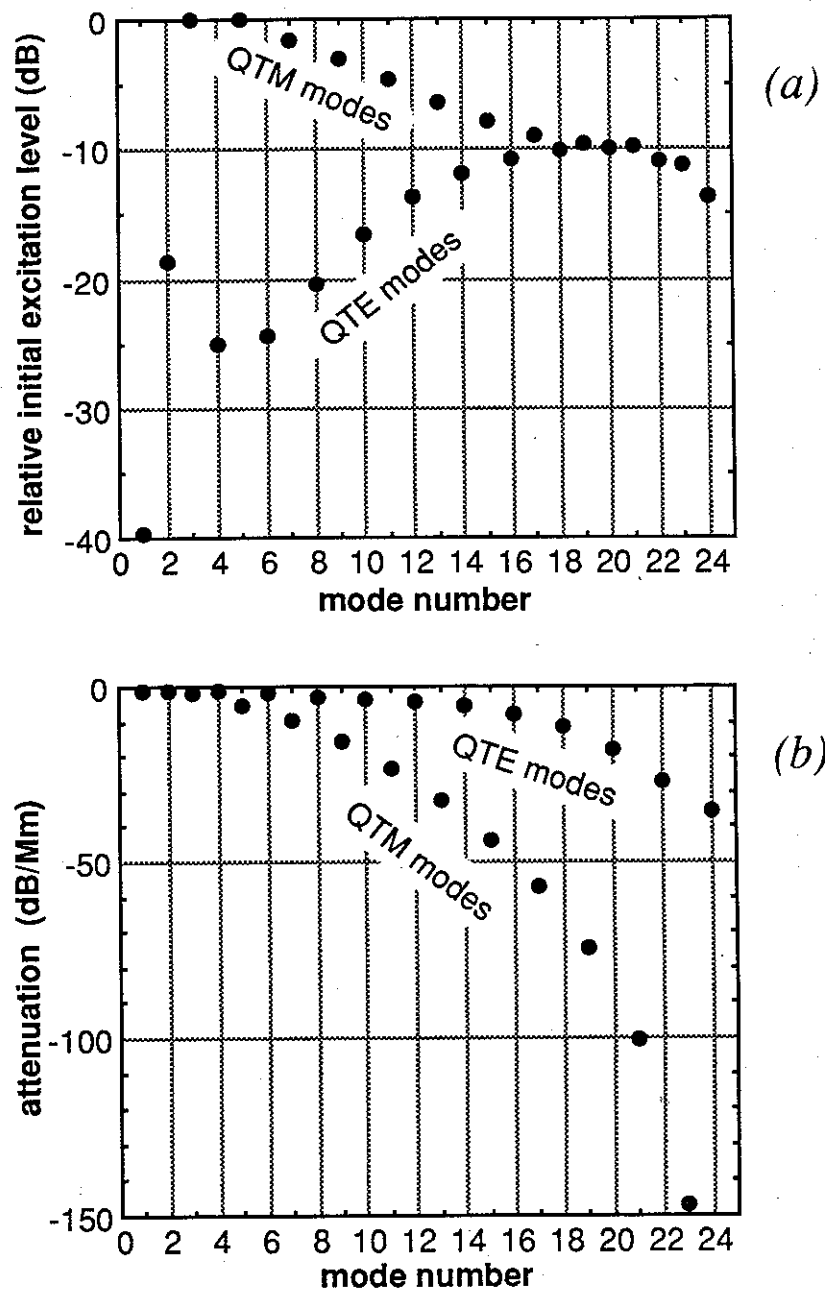


Figure 2.10: (a) Relative initial excitation level (in dB) of the first 24 modes for the example depicted in Figure 2.6. (b) The initial attenuation rate (in dB/Mm) for these same 24 modes.

Chapter 3

Two-dimensional Numerical Modeling of VLF Wave Propagation in the Earth-Ionosphere Waveguide

3.1 Simple Two-dimensional Modeling

The governing equation (Equation 2.3) for VLF wave propagation in the Earth-ionosphere waveguide can be modeled numerically using realistic (“typical”) values for the various geophysical parameters required by these expressions.

Parameters

These include:

- Transmitter characteristics such as the transmitter location x_T and altitude, the transmitter frequency f , the radiated power P , the antenna orientation t_j , and the type of antenna;
- receiver characteristics such as the receiver location (with respect to the transmitter location) x_R and its altitude, the antenna orientation r_j , and the type of antenna;
- the propagation path (or great circle path, GCP) distance d ;
- properties of the Earth surface such as conductivity σ , relative dielectric constant versus depth $\epsilon_r(-z)$, and height of the surface above sea level;

- and properties of the lower ionosphere such as the electron, positive ion, and negative ion densities as functions of altitude ($N_e(z)$, $N_+(z)$, and $N_-(z)$), the electron and ion collision frequencies versus altitude, and the local magnetic field $B(z)$.

Typical Parameter Values

Typical values of these variables for VLF wave propagation in the Earth-ionosphere waveguide are as follows:

- Frequencies f of interest range from ~ 3 kHz to 50 kHz. (These correspond to wavelengths λ between 100 km and 6 km, respectively.) As for the total radiated transmitter power P , in all of the calculations made in this research, its value has been normalized to 1 kW.
- Typically utilized VLF antennas include electric dipoles, monopoles, or magnetic loop antennas, but as mentioned in the previous chapter, high power VLF transmitters typically use a vertically-oriented (z direction) electric monopole antenna. VLF narrowband receivers used by Stanford for measurement of subionospheric signals as mentioned in Chapter 1 typically use a magnetic loop which is oriented to detect the horizontal component of the magnetic field h_y of the propagating wave [Wolf, 1990]. At the Earth's surface, this usually corresponds to the vertical electric field component e_z , and for low order modes (typically the dominant modes for frequencies $< \sim 30$ kHz) this is usually the case as can be seen by comparing the magnitude profiles of h_y and e_z in Figure 2.7. However, for higher order modes (see Figure 2.9), even though the e_y component is still the only non-zero electric field component at the Earth's surface, the h_y component is not the only non-zero magnetic field component at the surface—there is also a finite amount of h_x , which is also a horizontal component of the magnetic field. For the purposes of this research, however, vertical electric dipoles are assumed for both the transmitting and receiving antennas.
- Typical transmitter–receiver path lengths d of interest range from ~ 500 to 12,000 km.

- Effective Earth surface conductivities σ at the frequencies of interest range from $\sim 10^{-5}$ to 10^{-4} S/m for ice caps and ice shelves, and $\sim 10^{-3}$ to 10^{-2} S/m for continental mountains and soils, to 4 S/m for sea water [Hauser *et al.*, 1969]. Corresponding relative dielectric constants range from $\epsilon_r = 5$ for ice through $\epsilon_r = 15$ for soils to $\epsilon_r = 81$ for sea water.
- This research is confined to modeling disturbances in the nighttime lower ionosphere because the daytime lower ionosphere 'boundary' is so low in altitude that the effect of the electron precipitation mechanism described in Chapter 1 that causes Trimpi events is not large enough to measureably perturb the daytime ambient electron density profile. The nighttime D region (see Chapter 1) of the ionosphere is the least well known region of the ionosphere [Forbes, 1989; Ferguson *et al.*, 1989], and several versions of electron and ion density versus altitude profiles for this altitude range (~ 50 – 90 km) are commonly used. The simplest is a model in which the electron density increases exponentially with altitude [Wait and Spies, 1964]

$$N_e(z) = 1.4265 \times 10^7 e^{(\beta - 0.15)z - \beta h'} \quad (3.1)$$

where β is in inverse km, z is in km, N_e is in electrons per cm^3 , and h' is a reference height in km and can have various values depending on whether it is local daytime or local nighttime, the frequency of the wave, and the geomagnetic latitude [Morfitt, 1977; Ferguson, 1980; Ferguson *et al.*, 1989]. Other profiles are based on rocket measurements and various types of soundings (partial reflection method [Belrose and Burke, 1964], pulse cross modulation [Barrington *et al.*, 1963], incoherent scatter radar [Reagan *et al.*, 1981]) and are not simple mathematical relationships between electron density and altitude [Wait and Spies, 1964; Reagan *et al.*, 1981]. A typical example of these is the density profile shown in Figure 1.3, which is used as the ambient nighttime profile in most of the numerical examples given in this report.

- Similarly, various collision frequency altitude profiles exist for electron-neutral particle $\nu_e(z)$, positive ion-neutral particle $\nu_+(z)$, and negative ion-neutral particle $\nu_-(z)$ collision frequencies [Wait and Spies, 1964; Morfitt and Shellman, 1976]. A

typical example of these is the set of exponential profiles given in *Wait and Spies* [1964], and which are used as the default profiles throughout this research

$$\begin{aligned}\nu_e(z) &= 1.816 \times 10^{11} e^{-0.15z} \\ \nu_+(z) &= 4.540 \times 10^9 e^{-0.15z} \\ \nu_-(z) &= 4.540 \times 10^9 e^{-0.15z}\end{aligned}\tag{3.2}$$

where ν are in s^{-1} , and z is in km.

- The magnetic field is that of the Earth, and therefore has a magnitude of ~ 0.2 to 0.7 gauss ($1 \text{ gauss} = 10^{-4} \text{ tesla}$) and an orientation that varies from horizontal (parallel to the Earth's surface) near the equator to nearly vertical near the poles, and therefore depends on what geomagnetic latitudes the propagation path traverses.

Given these parameter values, the electric field along a propagation path can be calculated using the straightforward two-dimensional method given by Equation 2.3 [Wait, 1962], one dimension being distance along the transmitter-receiver great circle path (GCP) of propagation (x), and the other dimension being altitude (z). This method assumes that all path parameters extend to infinity in both directions transverse to the GCP direction (i.e., y direction; see Figure 3.1).

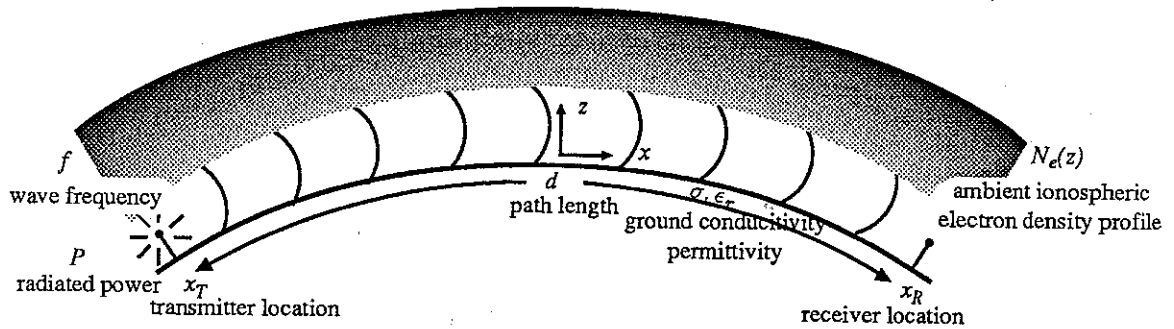


Figure 3.1: Geometry of the 2-D VLF Earth-ionosphere waveguide propagation problem showing the important parameters.

The values for the frequency, ground conductivity, relative dielectric constant, particle densities, collision frequencies, and magnetic field are used to determine the reflection

coefficient matrix elements which are then used to determine the eigenangles θ_n (and consequently the S_n). The reflection coefficient matrix elements, together with the antenna orientation factors t_j and r_j and antenna altitudes, are in turn used to determine the initial excitation factors $\Lambda_{j,n}^{T,R}$ and "height-gain" factors $G_{j,n}^{T,R}$.

Equation 2.3, however, assumes homogeneous conditions along the entire path. This situation occurs rarely. One example is long-distance propagation over an all-sea path. Even then, the path may cross a part of the Earth's surface where the Earth's magnetic field changes sufficiently (either in magnitude or direction) to cause significant differences in the signal's propagation from the simple case having homogeneous conditions (including a constant magnetic field) over the entire propagation path.

3.2 2-D Homogeneous Propagation Example

Figure 3.2 shows two examples of a 2-D calculation of vertical electric field strength versus distance for homogeneous conditions, one for an Earth surface conductivity of $\sigma = 10^{-3}$ S/m and relative dielectric constant of $\epsilon_r = 15$ which represents soil conditions in the mid-continental United States, and the other for $\sigma = 4$ S/m and $\epsilon_r = 81$ which represents sea-water; all other parameters being the same for the two calculations. The ambient nighttime ionospheric electron density profile given in Figure 1.3 was used, and the signal frequency was taken to be 25 kHz radiated from a vertical electric dipole transmitting antenna. Notice that the plots show that the received signal amplitude clearly depends on ground conductivity; the signal strength patterns for the two different ground conductivities diverge with distance. The signal that propagates over water is attenuated less after a long distance than the one propagating over land.

Figure 3.3 shows the signal strength pattern for the 25 kHz sea water example of Figure 3.2, but also plots the signal strength pattern for the slightly lower frequency of 24.5 kHz as well. We note that the successive series of peaks and nulls are shifted somewhat with distance for one frequency as compared to the other, but the overall behavior of the amplitude versus distance is very similar.

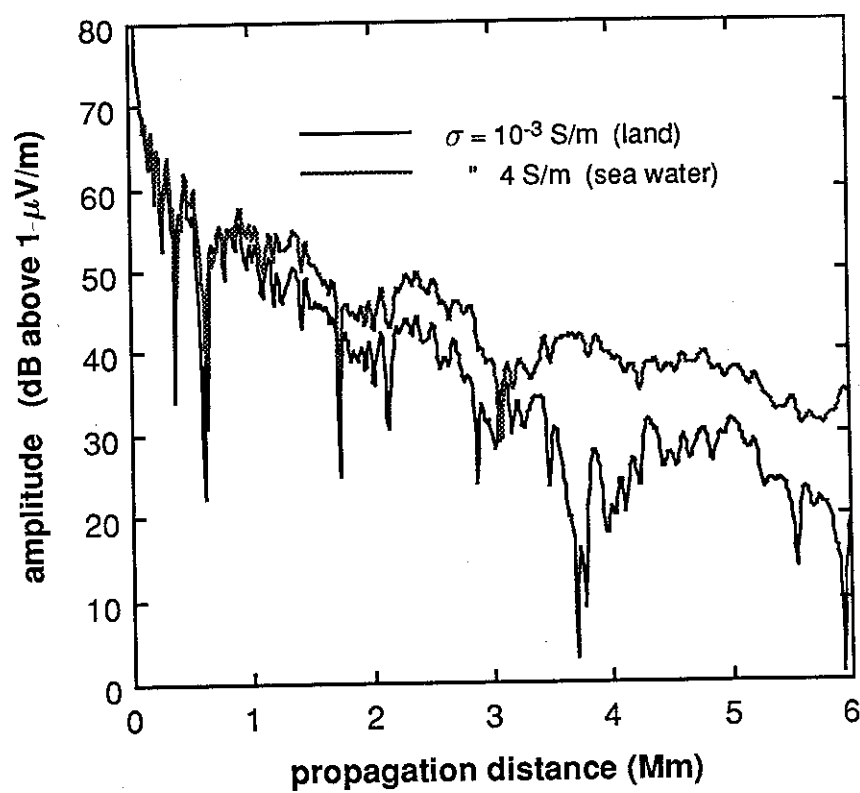


Figure 3.2: 2-D calculation of vertical electric field strength versus distance for two different homogeneous ground conductivities. See text for details.

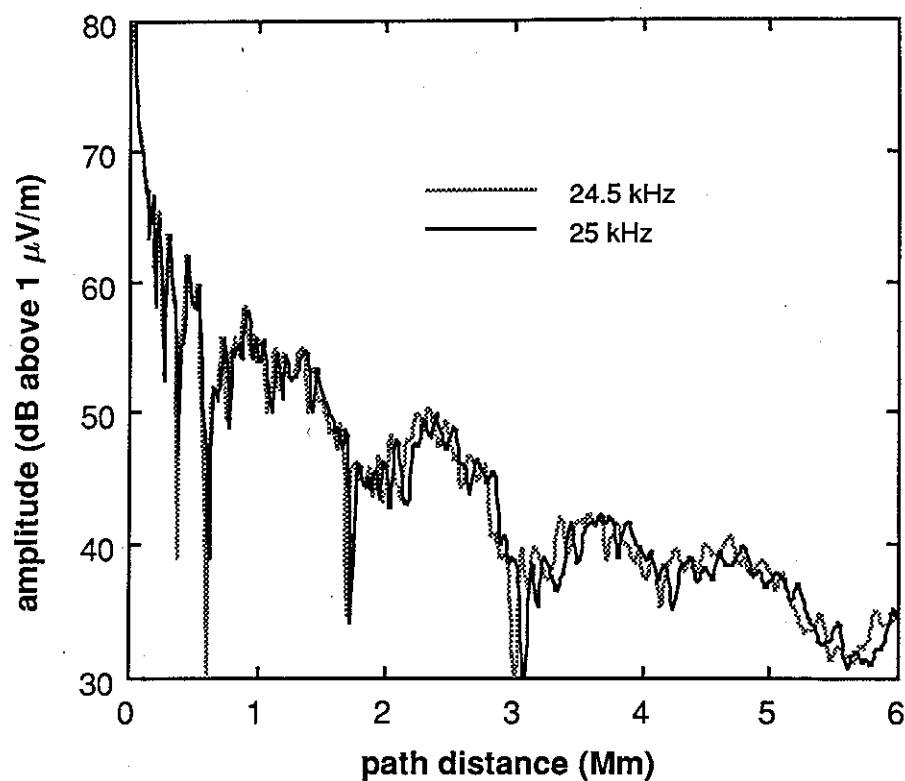


Figure 3.3: 2-D calculation of vertical electric field strength versus distance at two different frequencies for the same sea-water conditions as in Figure 3.2.

Figure 3.4 is a plot of the total vertical electric field strength versus distance for the same conditions as in the previous two figures ($f = 25$ kHz, $\sigma = 4$ S/m, $\epsilon_r = 15$, transmitter at $z = 0$ km), but measured by an antenna at three different elevations within the Earth-ionosphere waveguide: namely, at $z = 0$ km, 30 km, and 60 km. Note that the vertical component of the electric field at $z = 0$ plotted in Figure 3.4 is approximately equal to the total electric field at $z = 0$ since the horizontal electric field components in the relatively highly conducting sea-water are small. We note from Figure 3.4 that the total electric field structure varies considerably with altitude along the entire propagation path, due to the fact that the constructive or destructive interference between different waveguide modes is further modulated by the altitude variation of the electric field components for each mode as shown in Figure 2.7.

3.3 Mode Conversion

In the previous chapter we described how the electric field is a function of S_n which itself depends on the characteristics of the waveguide at each point along the propagation path. If these change slowly over distances the order of a wavelength, then it has been shown [Wait, 1962] that the energy of each mode does not convert measurably to other modes. On the Earth's surface, ground conductivity does change fairly rapidly and sometimes abruptly, and mode conversion must be accounted for whenever such a rapid conductivity change is encountered along a propagation path. Conversion between modes will occur wherever the propagating wave encounters rapid changes in the properties of the ionosphere boundary as well.

One method to numerically account for mode conversion along the propagation path (called the "mode conversion" method) is described as follows (refer to Figure 3.5). The entire propagation path is approximated by dividing the path into a discrete number of segments or "slabs" [Wait, 1968; Pappert and Snyder, 1972]. Within each slab all waveguide parameters are assumed to be homogeneous, and changes in the ground or ionospheric boundary characteristics occur abruptly at each slab-slab boundary. At each boundary, a set (a matrix, actually) of mode conversion coefficients is calculated based

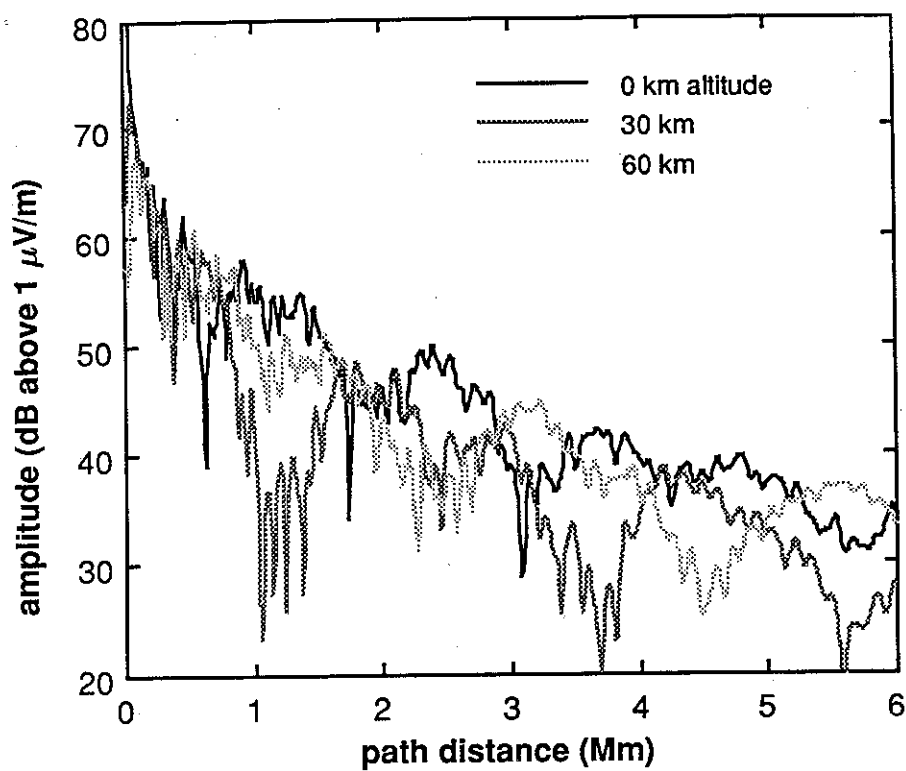


Figure 3.4: 2-D calculation of the total vertical electric field strength versus distance for the same conditions as in Figure 3.3 but measured at three different receiver elevations: 0, 30, and 60 km in altitude.

on the differences in the waveguide characteristics of the two adjoining slabs. These (complex-valued) coefficients represent how much of a given mode “converts” to each mode of the signal on the other side of the boundary. Theoretically, there are an infinite number of modes making up the total signal within each slab, but we only need be concerned with the non-negligible modes. For example, if there are N significant modes in slab i and M modes in slab $i + 1$, then for each of the N “incoming” modes there must be a coefficient representing how much of each of those modes is “converted” to each of the M “outgoing” modes. Thus, the set of all significant mode conversion coefficients will be a matrix with $N \times M$ elements.

The mode conversion process is represented pictorially in Figure 3.5 which shows a very simplified case of a propagation path consisting of three slabs. At the first slab–slab boundary, the ground conductivity σ changes suddenly, but the ionosphere remains the same. Below this point in the figure, we represent the signal propagating within the first slab as being made up of three modes of equal magnitude. At the boundary, most of the energy of mode 1 continues on as mode 1 and a small amount converts to mode 2. However, a larger amount of mode 2 converts to mode 1 resulting in there being more of mode 1 than of mode 2 propagating within slab 2. All of the energy of mode 3 continues into slab 2 as mode 3, so it does not change at the boundary. At the next slab boundary, the ground conductivity remains the same, but now the ionospheric density profile changes from profile I to profile II. The various mode conversions that occur due to this change in the waveguide characteristics are similarly represented below this slab.

3.3.1 The NOSC “Long Wave Propagation Capability” Program

As with the mode equation (Equation 2.9), the conversion coefficient matrices cannot be determined in closed form. In their development of a comprehensive 2-D modeling program called the Long Wave Propagation Capability, or “LWPC”, one of whose main components is the program MODEFNDR described in Chapter 2, NOSC also developed two different programs to calculate the mode conversion coefficient matrices at arbitrarily input slab–slab interfaces. One of these is called “FULLMC” [Pappert and Shockey, 1972] and is more mathematically fundamental, and slower in execution time,

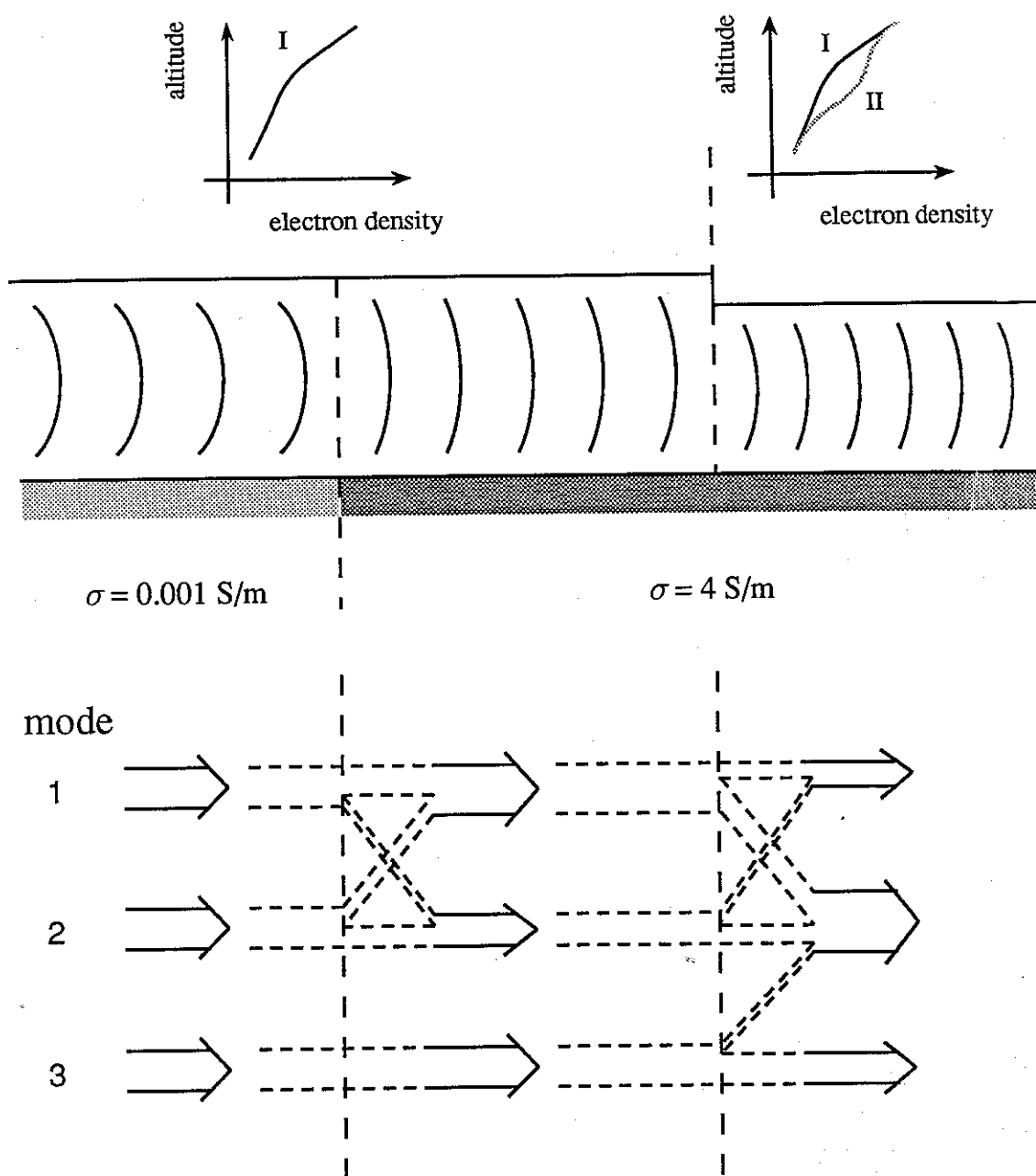


Figure 3.5: Illustration of mode conversion at slab boundaries.

than the other, called "FASTMC" [Ferguson and Snyder, 1980], which uses a number of approximations to reduce the execution time, and which has been made the other main component of NOSC's LWPC model.

Both methods assume invariance of all parameters in the transverse, or y , direction, and most importantly, neglect reflection at each boundary so that therefore there are no backward-traveling modes, eliminating the need to know the future propagation history of the signal [Wait, 1968a, b; Galejs, 1971; Pappert and Snyder, 1972; Smith, 1974].

FULLMC uses conventional mode conversion theory (see Ferguson and Snyder [1980]) where the electromagnetic field is represented by a complete set of orthogonal eigenvector functions, and the eigenvectors consist of all the components of both the electric and magnetic fields versus altitude (see section 2.3.1). An adjoint waveguide with adjoint eigenvector functions is calculated, and both sets of eigenfunctions are used to solve a full-wave integration up through the ionosphere that takes advantage of the biorthogonality condition to determine the mode conversion coefficients for the slab-slab interface [Pappert and Shockey, 1972; Pappert and Smith, 1972; Pappert and Snyder, 1972; Pappert and Morfitt, 1975].

FASTMC employs an incomplete set of non-orthogonal functions produced by discarding the complete eigenfunctions above some height h in the waveguide and approximating them below height h by Airy functions. No adjoint waveguide is introduced and the associated integrals are performed analytically. The problem reduces to a system of n equations in n unknowns, which can be solved by conventional techniques [Ferguson and Snyder, 1980; Pappert and Morfitt, 1975; Pappert and Ferguson, 1986].

Pappert and Ferguson [1986] showed that the FASTMC model gives excellent agreement with the FULLMC results and was therefore incorporated into NOSC's LWPC model [Ferguson et al., 1989]. Accordingly, our formulation of the 3-D VLF propagation code also relies on the use of FASTMC. In either case, in order to calculate the eigenfunction solutions required to determine the mode conversion coefficients, a knowledge of the mode eigenangle solutions and "height-gain" functions for each of the slabs along the propagation path is necessary. These are calculated by MODEFNDR as described in the

previous chapter, and the output from MODEFNDR is used as input to FULLMC or FASTMC.

3.3.2 The Ground Parameters

In order to model real signal propagation along arbitrary paths over the Earth's surface, values of conductivity σ and relative dielectric constant ϵ_r are taken from the DECO-NRL 10 level ground conductivity map of the world's surface [Ferguson and Snyder, 1987; Hauser *et al.*, 1969]. This database maps the entire Earth's surface into ten different pairs of σ and ϵ_r values. No capability for determination of the variation of these values with frequency is given. It also does not give ground elevation directly; nor does it allow for calculation of ground parameters versus depth, as was mentioned in Chapter 2.

3.3.3 The Ionospheric Parameters

As mentioned in section 3.1, a number of different models for the electron density in the lower ionosphere have been described [Wait and Spies, 1964; Helliwell, 1965; Morfit, 1977; Ferguson, 1980; Reagan *et al.*, 1981]. In order to compare the effects of lower ionospheric disturbances on waves propagating in their vicinity with waves propagating in their absence, we must use an ambient density profile that is consistent with the modified, or disturbed, density profile being examined. Tolstoy *et al.* [1986] use the exponential profile (Equation 3.1) of Wait and Spies [1964] as their ambient density profile and calculated their modified density profiles based on it. For the purposes of this research, we use modified electron density profiles produced by the model described in Inan *et al.* [1988a], and to maintain consistency, we adopt the ambient nighttime *D* region profile used in that model which was taken to be representative of geomagnetically quiet times [Reagan *et al.*, 1981; Helliwell, 1965]. This ambient profile is shown in Figure 1.3.

3.4 2-D Multiple Slab (Mode Conversion) Example

Figure 3.6 is a plot of the amplitude and phase of the total vertical electric field as a function of distance from the NSS transmitter (21.4 kHz) in Annapolis, Maryland along the GCP to Stanford, California. It uses the ambient ionosphere of Figure 1.3 (described in section 3.3.3) and the ground conductivities and relative dielectric constants as contained in the ground conductivity map described in section 3.3.2. The vertical lines indicate the “slab” boundaries; i.e., where the ground conductivity changed along the NSS-to-Stanford propagation path. The ionospheric properties were assumed to be unchanging along the path.

3.5 2-D Modeling in the Presence of an Ionospheric Disturbance

Given the capability of accounting for mode conversion between two “slabs” having one or more differing geophysical parameters, the 2-D method can be used to model VLF propagation in the presence of an ionospheric disturbance along the propagation path as shown in Figure 3.7a. For example, the effects on the received signal of a disturbed density profile, such as the one shown in Figure 3.7b, can be studied as a function of its width a and location x_0 along the GCP. The disturbed region can be modeled as yet another “slab” along the propagation path with the same ground parameters as existed along that segment in the absence of the disturbance, but with the modified ionospheric parameters due to the disturbance. Initial theoretical models of the effects of lightning-induced disturbances on subionospheric signals have used this 2-D method, which treats the Earth-ionosphere waveguide as infinite in the horizontal direction transverse to the propagation path, and assumes that the lower ionospheric disturbance lies on the propagation path and is infinite in the transverse dimension also [Tolstoy, 1983; Inan *et al.*, 1985; Tolstoy *et al.*, 1986; Inan and Carpenter, 1987; Cotton, 1989].

Figure 3.7c and d show respectively the amplitude and phase of the total vertical electric field at ground level as a function of distance in the absence of the disturbance

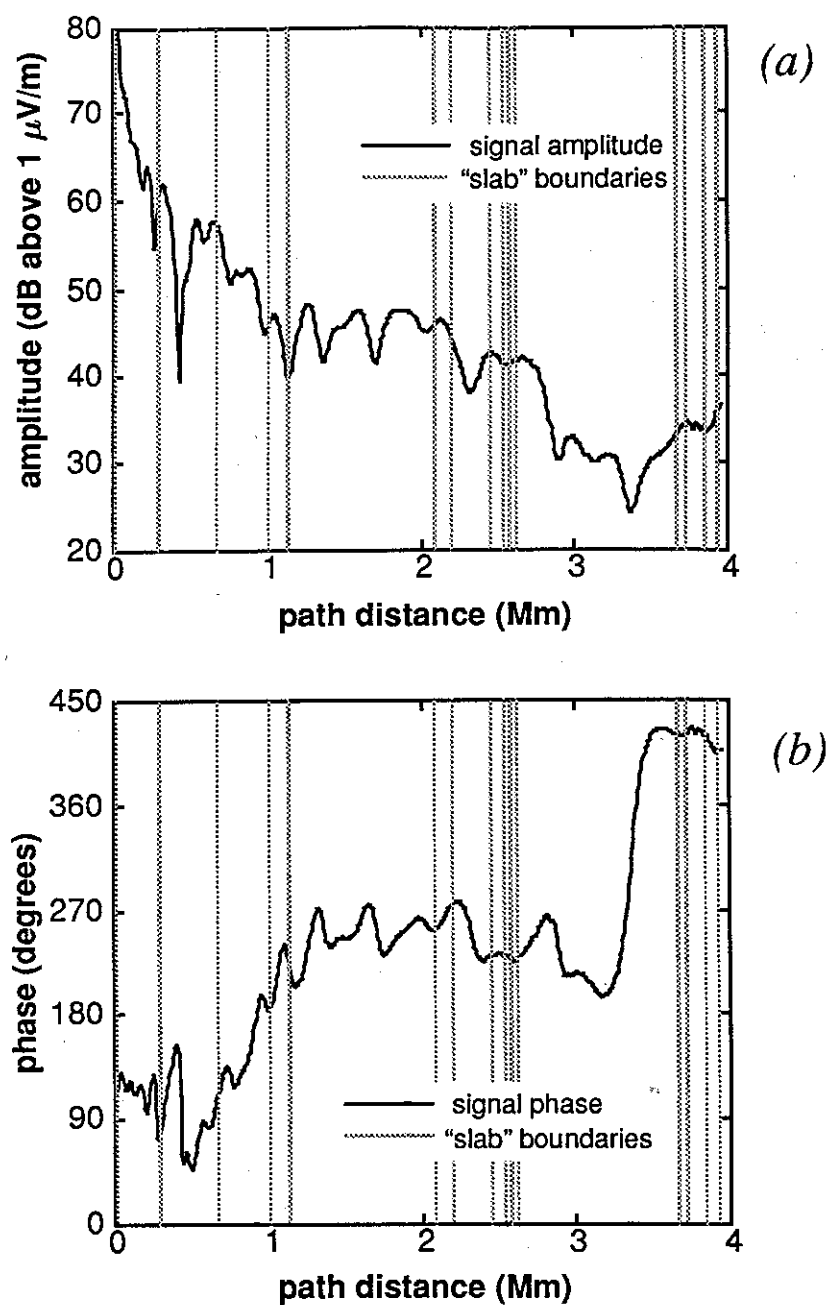
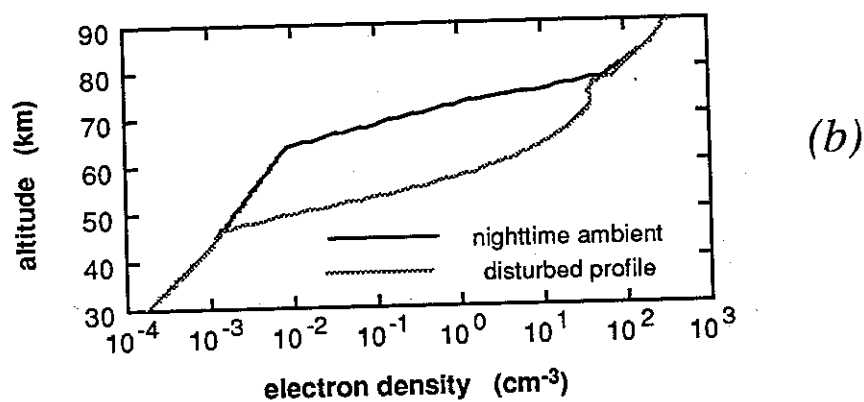
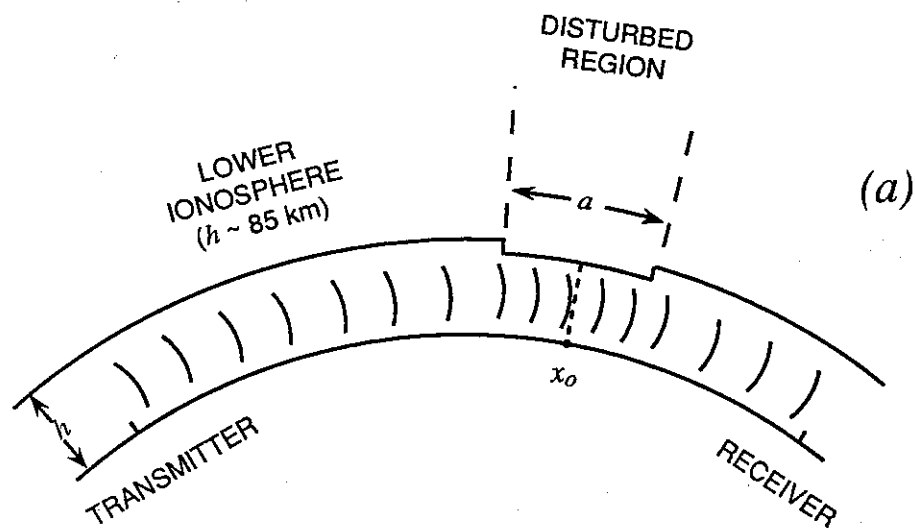


Figure 3.6: (a) Electric field strength along the NSS to Stanford path. The dashed vertical lines indicate the slab boundaries at which the ground conductivity changes and conversion of waveguide modes can occur. (b) Phase of the signal versus path distance.

(ambient condition) and in the presence of the disturbance. This example is for the 21.4 kHz NSS signal traveling from east to west across North America described in the previous section. A disturbance “slab” with a width $a = 200$ km centered at $x_o = 2$ Mm along the GCP from the transmitter was used in the calculations for this plot. The ionospheric disturbance perturbs the signal in a manner similar to that illustrated in Figure 3.5 so that the variation of both amplitude and phase is different from the ambient pattern beyond the point where the disturbance is located. We note that the change in amplitude and/or phase relative to the ambient signal at points beyond the disturbance (along the GCP) sensitively depends on the receiver location. Both the magnitude and sign of the change in amplitude (denoted as ΔA) or the change in phase (denoted as $\Delta\phi$) changes with location of the receiver—sometimes being negative in sign and sometimes positive. In this example, for a receiver located at Stanford, California (~ 3950 km from the transmitter), a change in amplitude ΔA of -1.95 dB and a change in phase $\Delta\phi$ of 14.1° is evident from Figure 3.7. However, the 2-D method of modeling the effect of these disturbances is very limited in how well it can represent actual ionospheric disturbances due to lightning, which are believed to have a finite transverse extent of the order of 50–500 km.



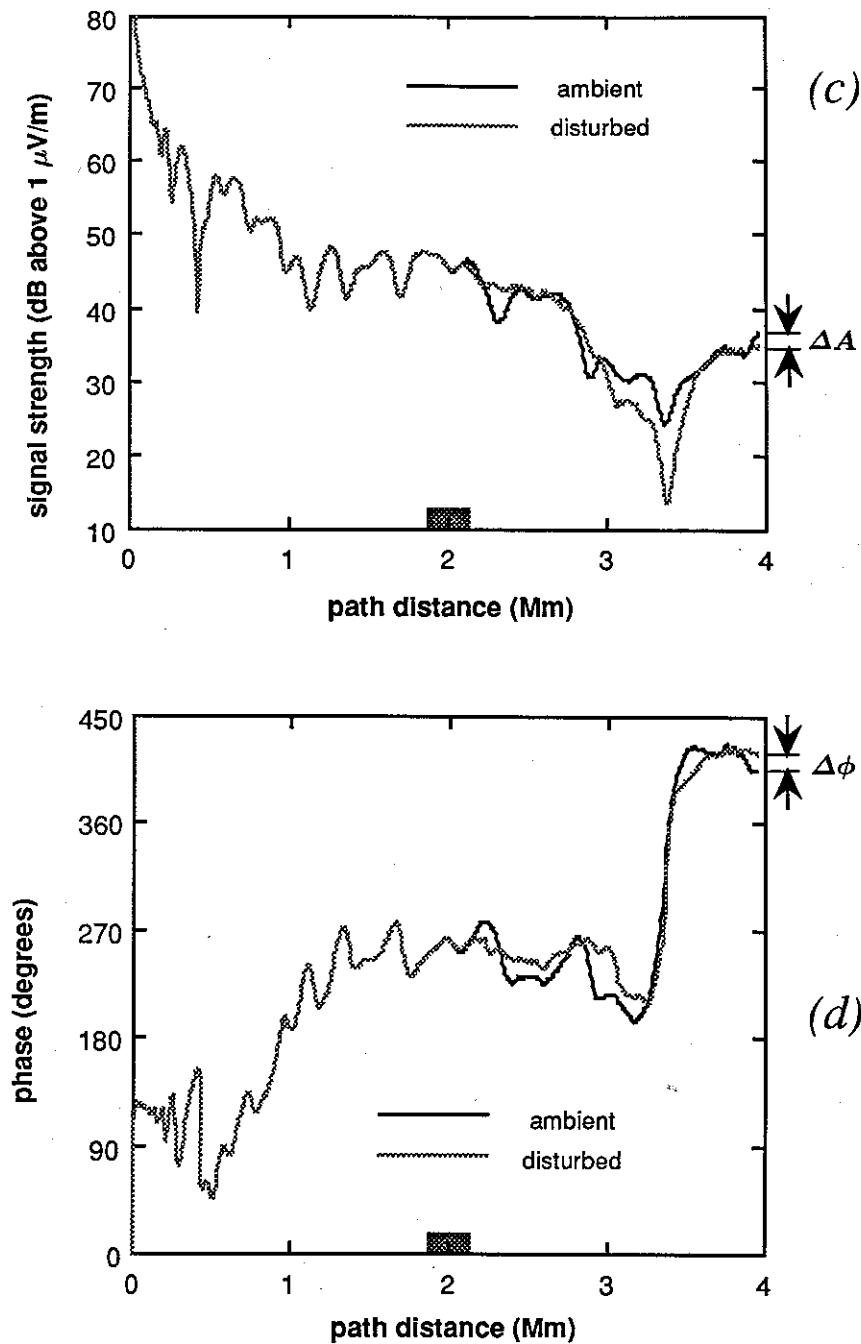


Figure 3.7: (a) Schematic illustration of the 2-D method for modeling waveguide propagation in the presence of a disturbance along the waveguide. (b) Profiles of electron density versus altitude of the ambient ionosphere and within the disturbance region used to calculate Figures 3.7c and d. (c) Amplitude of the total vertical electric field as a function of distance under ambient conditions and in the presence of the disturbance. (d) Corresponding phase of the signal.

Chapter 4

Three-Dimensional Modeling of VLF Scattering from Localized Disturbances in the Lower Ionosphere

A three-dimensional model of VLF propagation in the Earth-ionosphere waveguide is needed in order to better model realistic cases of scattering caused by localized disturbances in the Earth-ionosphere waveguide. One of the applications of such a model that is of current interest concerns disturbances of finite transverse extent that are believed to be created by LEP events as discussed in Chapter 1. Such disturbances may either partially overlie the great circle propagation path (GCP), or be located nearby, but to one side of the GCP, completely off the path.

4.1 Formulation of the Method

In a 2-D model, a localized disturbance can be modeled only as a “strip” crossing over the propagation path and extending on either side out to infinity. Experimental evidence, on the other hand, indicates that lightning-induced ionospheric disturbances are finite in extent [*Inan et al.*, 1990]. A 3-D model is thus needed for more realistic modeling of disturbances that lie on the GCP as well as those lying completely off the propagation path. Possibly the first evidence of the need for a 3-D model was brought out by *Carpenter and LaBelle* [1982] who found that perturbations associated with ducted whistlers can at times be located at significant distances (up to ~ 200 km) transverse to the GCP

between transmitter and receiver. *Inan and Carpenter* [1987] also recognized the need for more realistic models which include the effects of off-GCP locations of ionospheric perturbations.

Recently, *Dowden and Adams* [1988, 1989a] put forward a heuristic three-dimensional model based on ‘echoes’ from lightning-induced electron precipitation (LEP) ionization ‘patches’ or ridges located off the GCP. In this chapter, we present a three-dimensional model based on a waveguide mode scattering analysis of VLF propagation in the Earth-ionosphere waveguide in the presence of ionospheric perturbations of various types [Wait, 1961, 1964a, b, c].

4.1.1 Modal Electric Field Scattered by an Ionospheric Disturbance

Figure 4.1 shows the basic geometry of the 3-D problem. To account for all three dimensions, we need to incorporate information from the transverse (y) direction into the formulation. Equation 2.3 can be generalized to include slow variations in the local properties of the Earth-ionosphere waveguide in both the GCP direction (x direction) and the transverse direction (y direction), in which case S_n becomes a function of both x and y . (See Figure 4.1b.) The expression for the total field a distance d from the transmitter then has the form [Wait, 1964a]

$$E_{total}(d) \simeq \left[\frac{d/R_E}{\sin(d/R_E)} \right]^{\frac{1}{2}} \sum_n A_n^{T,R} e_n$$

where

$$e_n \simeq \left\{ \frac{1}{\sqrt{x/R_E}} \exp[-ik_o \int_C S_n(x', y') ds] \right\}_{x=d}, \quad (4.1)$$

the origin ($x = 0, y = 0$) is located at the transmitter, and the integration contour C is along the path of minimum total phase between the transmitter and observation point at d . The other variables are as defined previously in Chapter 2.

The above expression assumes that the properties of the Earth-ionosphere waveguide are slowly-varying in the horizontal (x and y) directions so that the conversion of modes from one order to another, i.e., mode coupling, can be safely ignored. As noted before,

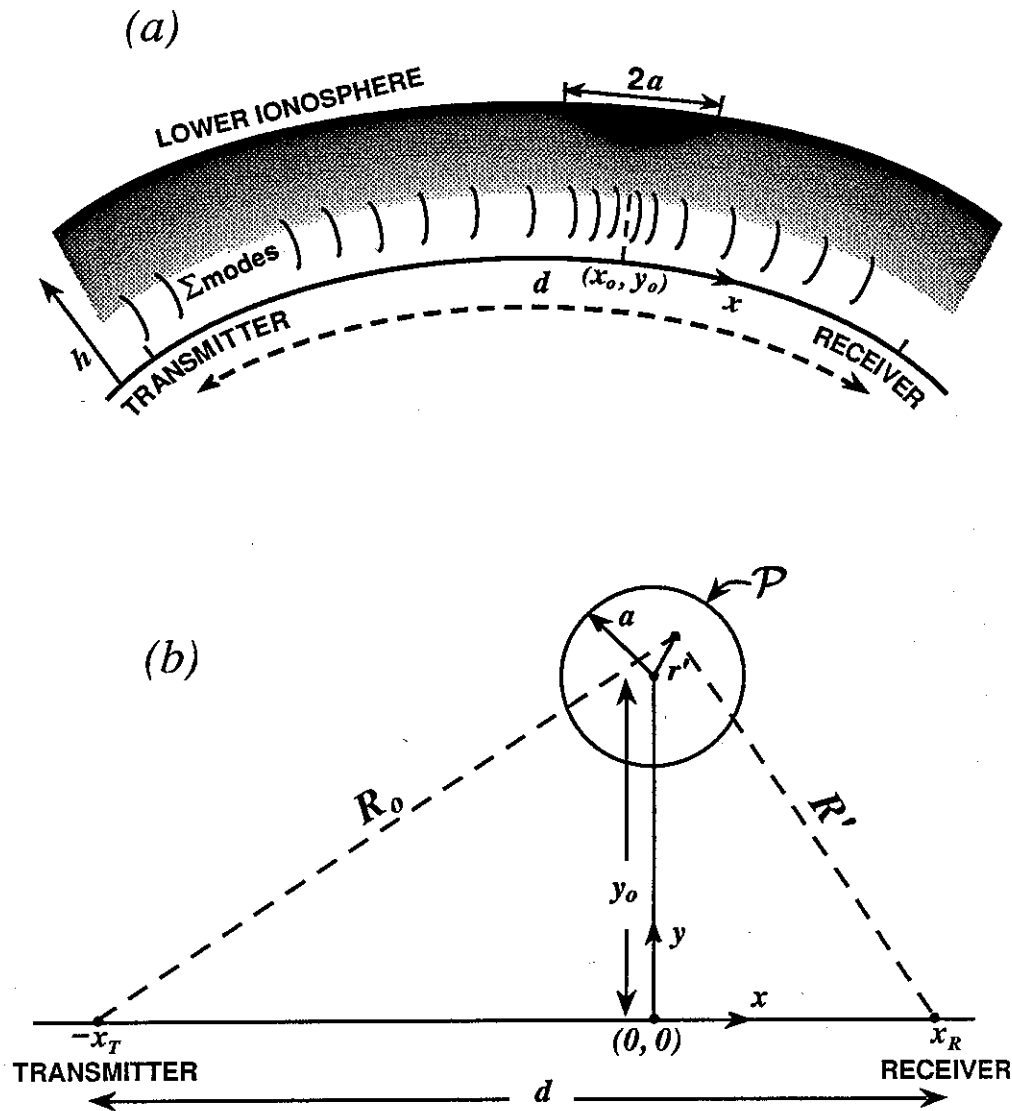


Figure 4.1: (a) Side view representation of the Earth-ionosphere waveguide between a transmitter and receiver separated by a distance d along the surface of the Earth. The change in the electron density with altitude h of the lower ionosphere is represented by the change in shading density. Also represented is a density enhancement disturbance region or perturbation of the ambient ionosphere such as those generated by lightning-induced electron precipitation bursts. The center of this disturbance is located at the point (x_o, y_o) . Such a disturbance, appearing transiently, scatters some of the signal impinging on it and causes a temporary perturbation in the total signal measured at the receiver. (b) A plan view, seen from above, of the situation depicted in Figure 4.1a showing the three-dimensional configuration of the problem and identifying the geometry and variables used in Equations 4.5–4.11. Note that the origin has been shifted to the point $x = x_o$.

this is referred to as the WKB approximation. This assumption is justified if the waveguide properties do not change appreciably in a horizontal distance of one wavelength [Wait, 1964a] and if each mode n has relatively low attenuation, i.e.,

$$\text{Im}[S_n(x, y)] \ll 1. \quad (4.2)$$

Since the modal field e_n satisfies a two-dimensional Helmholtz equation of the form

$$\left[\frac{\partial^2}{\partial x^2} + \frac{\partial^2}{\partial y^2} + (k_0 S_n)^2 \right] e_n = 0 \quad (4.3)$$

for each mode of order n , we can use a perturbation method to solve for each modal field e_n in the presence of a localized disturbance region \mathcal{P} in the waveguide. Assuming that within the region \mathcal{P} mode coupling effects do not occur, and that Earth curvature effects are negligible, the solution of Equation 4.3 for each modal field e_n can be found using a Green's function method [Arfken, 1970]. In this case, the solution is found to be [Wait, 1964a]

$$\begin{aligned} e_n(x, y) &= \overbrace{e_n^o(x, y)}^{\text{direct field}} + \overbrace{e_n^s(x, y)}^{\text{scattered field}} \\ &= e_n^o(x, y) - \frac{ik_0^2}{4} \iint_{\mathcal{P}} \underbrace{[S_n^2(x', y') - (S_n^o)^2]}_{\Delta S^2} \underbrace{e_n(x', y')}_{\substack{\text{field} \\ \text{inside} \\ \text{disturbance}}} \underbrace{H_0^{(2)}(k_0 S_n^o R')}_{\substack{\text{cylindrical} \\ \text{spreading} \\ \text{factor}}} dx' dy' \end{aligned} \quad (4.4)$$

where

e_n is the total modal field for the mode of order n (i.e., the total field seen at (x, y) in the presence of some disturbance in the waveguide);

e_n^o is the unperturbed modal field, also called the 'direct' field, (i.e., the field seen at (x, y) in the absence of any disturbance);

e_n^s is the secondary or 'scattered' field, (i.e., the field seen at (x, y) due to the disturbance);

S_n^o is the ambient value of S_n in the absence of any disturbance. (In the single-mode analysis, it is a constant independent of x and y);

\mathcal{P} is the region of integration, or 'patch', which extends over that portion of the x - y plane that encompasses the disturbance (i.e., where $S_n \neq S_n^o$);

$H_0^{(2)}$ is a Hankel function of the second kind of order zero;

and

$$R' = \sqrt{(x - x')^2 + (y - y')^2}. \quad (4.5)$$

is the distance from each integration point (x', y') within the disturbance to the observation point (x, y) .

In order to simplify the evaluation of Equation 4.4, we shift the origin from the transmitter location to the point $x = x_o$ along the GCP between transmitter and receiver. A plan view of the geometry is shown in Figure 4.1b. The origin is located such that the transmitter coordinates are $(-x_T, 0)$ and the location where the field e_n is observed, i.e., the receiver coordinates, are $(x_R, 0)$. Thus, $R' = \sqrt{(x_R - x')^2 + (y')^2}$ and $d = x_T + x_R$.

Equation 4.4 is a Fredholm equation of the second kind, which has no general closed form solution and is typically solved by successive approximations to form a Neumann series [Arfken, 1970]. However, an approximate solution of Equation 4.4 can be found by substituting the unperturbed field e_n^o for the total perturbed field e_n inside the integral. (This is known as the Born approximation [Born and Wolf, 1965].) This substitution is justified if S_n inside the disturbance region \mathcal{P} is only slightly different from the ambient, or undisturbed, value S_n^o (i.e., $|S_n^2 - (S_n^o)^2| \ll 1$), a condition that holds for the various ionospheric disturbance electron density profiles that were considered in this study and which are described in section 4.2.

From Equation 4.1 it can be shown that the unperturbed field e_n^o at a distance R_o from the transmitter and at a location (x', y') has the form

$$e_n^o(x', y') \simeq \frac{K}{\sqrt{R_o}} e^{-ik_o S_n^o R_o} \quad (4.6)$$

where for the geometry shown in Figure 4.1b, K is a constant factor and

$$R_o = \sqrt{(x_T + x')^2 + (y')^2}. \quad (4.7)$$

For locations (x, y) greater than approximately one wavelength from the transmitter or receiver, the asymptotic form of the Hankel function as given below can be used in Equation 4.4 [Abramowitz and Stegun, 1964].

$$H_0^{(2)}(k_o S_n^o R') \simeq \left[\frac{2i}{\pi k_o S_n^o R'} \right]^{\frac{1}{2}} e^{-ik_o S_n^o R'} \quad (4.8)$$

With the above-mentioned assumptions and substitutions, the expression for the scattered modal field seen at the receiver, $e_n^s(x_R, 0)$, normalized by the unperturbed modal field that would have been seen at the receiver in the absence of a disturbance, $e_n^o(x_R, 0)$, is

$$\frac{e_n^s}{e_n^o} \bigg|_{(x_R, 0)} \simeq \frac{-ik_o^2}{4} \sqrt{\frac{i2d}{\pi k_o S_n^o}} \iint_{\mathcal{P}} \frac{[S_n^2(x', y') - (S_n^o)^2]}{\sqrt{R_o R'}} e^{-ik_o S_n^o (R_o + R' - d)} dx' dy' \quad (4.9)$$

where d is the GCP distance between the transmitter and receiver. For the purposes of this study the region \mathcal{P} is assumed to be a circular, cylindrically symmetric disturbance with radius a , and because of circular symmetry, $S(x', y')$ becomes $S(r')$ [Wait, 1964b]. Thus, the assumed geometry is as shown in Figure 4.1b, and after making the substitutions $x' = r' \sin \theta'$ and $y' = y_o + r' \cos \theta'$, Equation 4.9 can be rewritten as

$$\frac{e_n^s}{e_n^o} \bigg|_{(x_R, 0)} \simeq \frac{-ik_o^2}{4} \sqrt{\frac{i2d}{\pi k_o S_n^o}} \int_0^{2\pi} \int_0^a \frac{[S_n^2(r') - (S_n^o)^2]}{\sqrt{R_o R'}} e^{-ik_o S_n^o (R_o + R' - d)} r' dr' d\theta' \quad (4.10)$$

For a circular disturbance of the ionosphere of radius a , located at (x_o, y_o) , and for a given frequency, a (complex) value for the field scattered by the disturbance relative to the 'direct' signal can be determined numerically from Equation 4.10 if the ambient refractive index S_n^o and the refractive index in the disturbance region $S_n(r')$ are known. The above equations provide a means to numerically model the effects of localized 3-D disturbances on VLF waves propagating in the Earth-ionosphere waveguide [Poulsen et al., 1990].

4.1.2 Relationship between the Direct Modal Field e_n^o and the Scattered Modal Field e_n^s

The relationship between e_n^s and e_n^o of Equation 4.10 can be illustrated by using a phasor diagram as pictured in Figure 4.2. The phasor representing the total field e_n is the vector sum of the phasors representing the direct field e_n^o and the scattered field e_n^s . The difference between the length of e_n and the length of e_n^o represents the change in amplitude (ΔA) caused by e_n^s . The difference between the phase angles $\angle e_n$ and $\angle e_n^o$ represents the change in phase ($\Delta\phi$) caused by e_n^s . These two quantities, ΔA and $\Delta\phi$, are the relevant quantities measured in the experimental data; and theoretical values for ΔA and $\Delta\phi$ as would be observed at the receiver can be readily computed from the (complex) value of e_n^s/e_n^o determined from Equation 4.10.

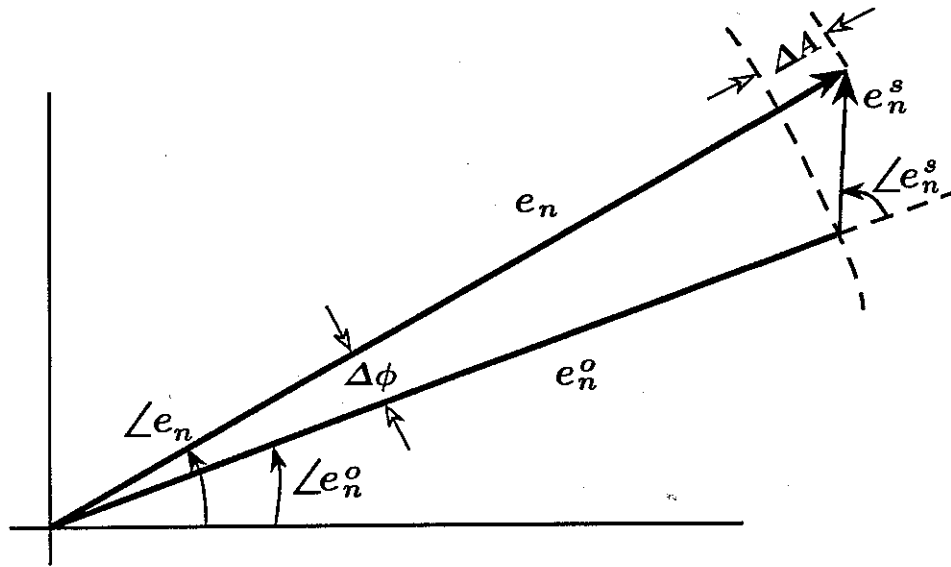


Figure 4.2: Phasor diagram illustrating the relationship between the total signal modal field e_n , the direct, or unperturbed, signal modal field e_n^o , and the scattered signal modal field e_n^s . The two quantities important in the discussion of the results, ΔA (change in amplitude) and $\Delta\phi$ (change in phase), are indicated. The phase angles $\angle e_n$ and $\angle e_n^o$ are measured with respect to the same (arbitrary) reference.

4.2 The Scattering Disturbance Model

One important cause of localized disturbances in the lower ionosphere, and the primary motivation behind this research, is the mechanism hypothesized as causing LEP events and associated perturbations in subionospheric VLF signals (see Chapter 1). This hypothesis is that an observed subionospheric VLF signal perturbation occurring within 0.2–1.0 s after the time of origin of an associated whistler or lightning discharge is caused by the precipitation of bursts of electrons resulting from gyroresonant interactions in the magnetosphere between whistler waves from lightning and energetic electrons [Chang and Inan, 1985]. When the energies of the precipitating electrons exceed ~ 50 keV, the particles penetrate down to altitudes below 90–100 km, where they can alter the upper VLF waveguide boundary in a localized region and consequently affect the mode structure of the propagating wave [Wolf and Inan, 1990].

Since the energy spectra of electrons precipitated by whistlers is a complicated function of wave frequency and magnetospheric parameters [Chang and Inan, 1985], a program, called “TSIM”, based on a simple theoretical model developed by Inan *et al.* [1988] is used to calculate the change in the lower ionospheric electron density profile that is expected to be produced under different conditions. The model does not account for the magnitude of pitch angle scattering that is induced by the wave, which requires test particle modeling of the gyroresonant scattering process [Inan *et al.*, 1989]. Rather, the simple model assumes interactions to occur at the equator and determines the energy content of the precipitated electron burst based on the frequency spectrum of the whistler wave and the L -shell of propagation. (The McIlwain’s L parameter identifies the Earth’s magnetic field lines; e.g., the $L = 2$ field line crosses the geomagnetic equator at a geocentric distance of 2 Earth radii [McIlwain, 1966; Hilton, 1971].)

In calculating the energy distribution of the precipitated electron burst, the model considers the electron energies required for gyroresonance with typical whistler frequencies of 0.2–6 kHz, representative equatorial cold plasma densities [Park *et al.*, 1978; Brace and Theis, 1974], and it assumes equilibrium conditions for the energy and L -dependence of the trapped particle flux, linear scattering with an interaction region of fixed length,

and a constant whistler wave intensity over the 0.2–6 kHz range. The pulse duration of the lightning-induced electron precipitation (LEP) bursts is a user-defined variable, and is assumed to be 0.2 s based on *Chang and Inan* [1985], *Inan and Carpenter* [1987], and *Voss et al.* [1984]. The average total energy flux in ergs cm⁻² s⁻¹ is also a user-defined variable which is determined on the basis of experimental data; typically measured fluxes being in the 10⁻³ to 10⁻² ergs cm⁻² s⁻¹ range.

For the production of the secondary ionization by the precipitating electrons, the model assumes that the depth of penetration is determined by the incident particle energy and atmospheric pressure [*Rees*, 1963; *Rishbeth and Garriott*, 1969]. The ambient nighttime *D* region electron density profile used, as shown in Figure 1.3 (also shown here in Figure 4.3), is representative of geomagnetically quiet times. The various disturbance density profiles used in this research, were determined using the TSIM model by specifying specific *L*-shell values of interest and typical average total energy fluxes based on theoretical work [*Chang and Inan*, 1985] and also satellite observations [*Voss et al.*, 1984]. Figure 4.3 shows examples of several profiles (which we identify by the labels “I”, “II”, “III”, “IV”, and “V”) representative of the electron density at the location of maximum perturbation (x_o, y_o) as a function of altitude h resulting from electron precipitation bursts induced by lightning-generated whistlers propagating at $L = 3, 2.5, 2, 1.6$, and 1.4 , respectively. The ambient nighttime *D* region electron density profile is also shown for reference. The total precipitating electron energy flux density for each profile was taken to be 5×10^{-3} ergs cm⁻² s⁻¹.

The difference between the disturbed electron density $N_e(h)$ at the location of maximum ionospheric perturbation and the ambient nighttime density $N_e^o(h)$ is designated by $\Delta N_e(h)$. The variation of $\Delta N_e(h)$ with distance in the horizontal direction r' (see Figure 4.1b) is represented in this work by a cylindrically symmetric Gaussian distribution such that

$$\Delta N_e(r', h) = \Delta N_e(x_o, y_o, h) e^{-(\frac{r'}{a})^2} \quad (4.11)$$

where $r' = [(x' - x_o)^2 + (y' - y_o)^2]^{\frac{1}{2}}$ and the parameter a is the effective disturbance ‘patch’ radius. In general, the refractive index $S_n(r')$ depends on density in a complex manner. However, analysis indicates that, for the parameter ranges considered, an approximate

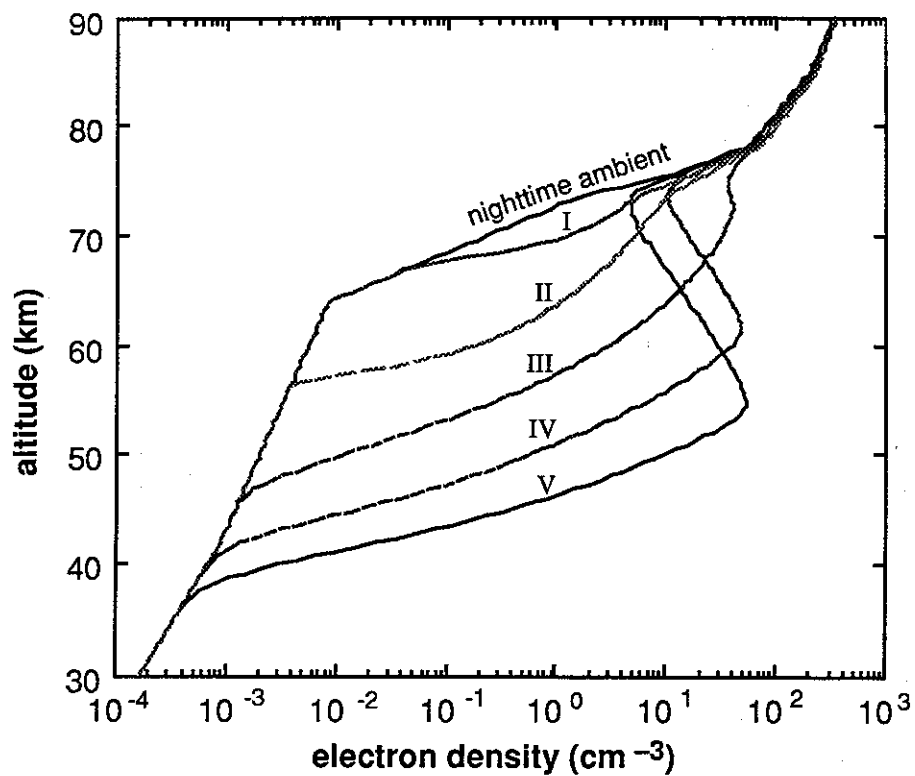


Figure 4.3: Ionospheric profiles used for examples and comparisons in this work. See text for the rationale for selection of these profiles.

expression for $S_n(r')$ can be written as

$$S_n(r') = [S_n(0) - S_n^o]e^{-(r'/a)^2} + S_n^o \quad (4.12)$$

Simplified analytic solutions of Equation 4.9 are derived in Appendix A assuming that Equations 4.11 and 4.12 apply.

4.3 Properties of the Modeled Scatterers

Using the range of typical values given in Chapter 3 of the various geophysical parameters relevant to the problem in hand, Equation 4.4 was evaluated to investigate the scattering nature of the type of ionospheric disturbances described in the previous section. The next two chapters report on the effect that this type of scatterer has on a VLF wave propagating within the Earth-ionosphere waveguide; in particular, the effects these scatterers have on the signal amplitude and phase as measured at the receiver. In this section, we describe several properties of the scatterers themselves as determined by numerically investigating the “scattered field” portion $e_n^s(x, y)$ of Equation 4.4.

4.3.1 Insensitivity of the Scattering to Surface Conductivity Variations under the Disturbance Region

Figure 4.4 is a plot of the eigenangle solutions in the complex plane for a 25 kHz signal and profile II of Figure 4.3 as the disturbed electron density profile for the lower ionosphere. The figure shows the results for four different cases of Earth surface conductivity, ranging from $\sigma = 4$ S/m for sea-water to $\sigma = 10^{-3}$ S/m for low-conductivity continental soil ($\epsilon_r = 81$ for the sea-water case, and $\epsilon_r = 15$ for the other three cases). Also plotted are the eigenangle solutions for the ambient electron density profile of Figure 4.3 and $\sigma = 4$ S/m.

Notice that the *disturbed* density eigenangle solutions for each mode are nearly identical regardless of the conductivity of the Earth surface boundary underneath the disturbed region. Only for mode $n = 3$ (QTM₂) is there any significant change in the eigenangle

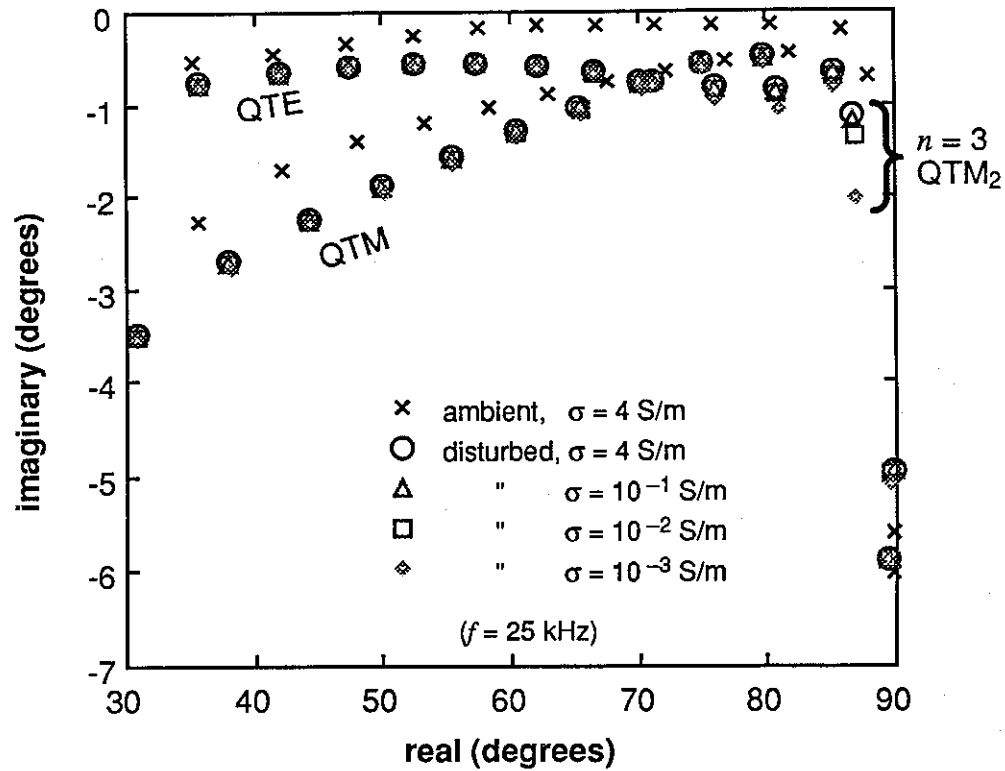


Figure 4.4: Eigenangles for different surface conductivities. Wave frequency of 25 kHz and disturbed density enhancement profile II from Figure 4.3 were assumed.

solution as the Earth surface conductivity is varied. The *ambient* ionosphere eigenangle solutions for Earth surface conductivities ranging from $\sigma = 10^{-1}$ to 10^{-3} S/m are also nearly identical to those of the ambient case shown in Figure 4.4 for $\sigma = 4$ S/m. This result indicates that the mode structure of propagating VLF waves encountering an ionospheric disturbance, as described by profile II of Figure 4.3, would be affected in a manner that is generally insensitive to differences in the conductivity σ of the surface under the disturbed region. In other words, a given ionospheric disturbance would scatter an incoming signal by the same amount whether the disturbance is over water or over different types of land.

Another way to show this result is by plotting the difference term of Equation 4.4 labelled " ΔS^2 " as shown in Figure 4.5. This is the only part of the "scattered field" portion of Equation 4.4 that depends on the properties of the disturbed region (i.e., the disturbed eigenangle solutions) under the Born approximation condition discussed in connection with Equations 4.9 and 4.10. As can be seen in the figure, the magnitude of ΔS^2 is nearly identical for all four ground conductivities for each mode. We note that since the strength of the scattered signal is directly proportional to the magnitude of ΔS^2 in Equation 4.4, the larger the ΔS^2 difference term is, the larger is the strength of the modal field scattered towards the receiver. Also since $S_n = \sin \theta_n$, generally speaking, in the region of the complex- θ plane where the non-negligible mode solutions lie, and for the type of disturbances considered in this research, the distance in the complex plane between an ambient mode eigenangle solution and its corresponding disturbed mode eigenangle solution gives a measure of the relative magnitude of the modal signal scattered towards the receiver by that disturbance. Thus, the farther apart a given mode's ambient and disturbed eigenangle solutions are, the greater is the relative magnitude of the scattered field of that mode compared to that of modes whose ambient and disturbed eigenangle solutions are closer together in the complex- θ plane. Figure 4.5 indicates that for a 25 kHz signal, the higher-order QTM modes have larger scattered field strengths than the higher-order QTE modes for a disturbance having the electron density shown in profile II of Figure 4.3. However, we note that the overall effect of any mode on the total scattered field is also dependent on the relative strength of that mode which arrives

at the disturbance, which is a function of the amount of that mode initially excited at the transmitter and the attenuation it suffers before reaching the disturbance.

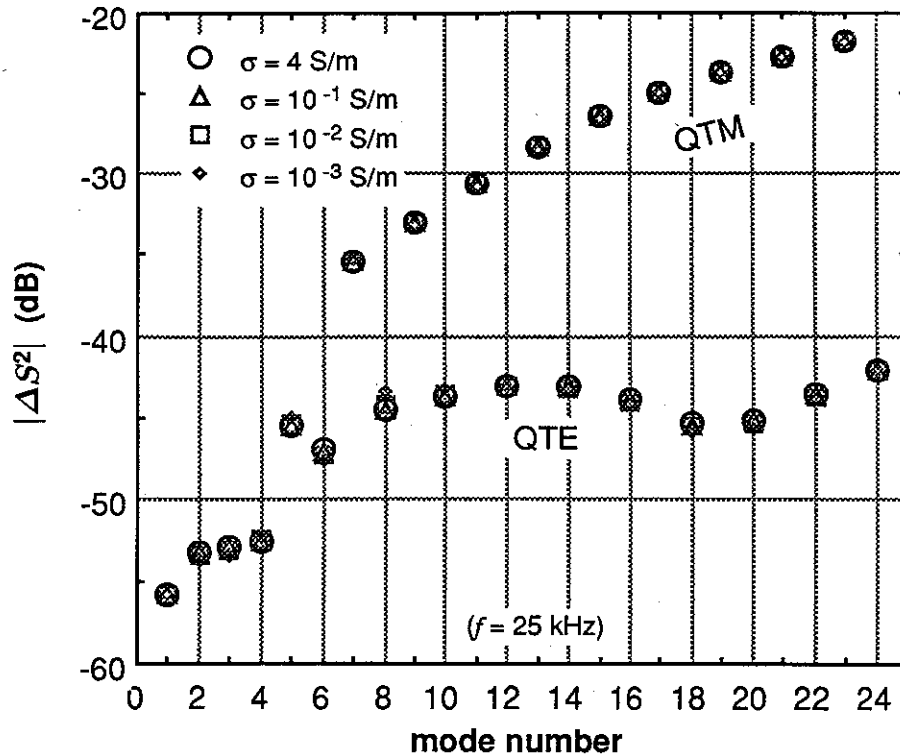


Figure 4.5: “ ΔS^2 ” (see Equation 4.4) versus mode number for a 25 kHz signal, profile II of Figure 4.3, and for different surface conductivities as indicated.

Figure 4.6 shows plots similar to Figure 4.4 for wave frequencies of 15 kHz (Figure 4.6a) and 50 kHz (Figure 4.6b). In Figure 4.6a only mode $n = 1$ (QTM₁) and $n = 3$ (QTM₂) show any significant variation in their eigenangle solutions (with respect to the ambient eigenangles); and in Figure 4.6b only mode $n = 6$ (QTM₃) shows any significant variation.

Finally Figure 4.7 is for the same conditions as Figure 4.4 except that two additional sets of eigenangle solutions are plotted. One set is for a low Earth surface conductivity of $\sigma = 10^{-4} \text{ S/m}$ and permittivity of $\epsilon_r = 10$ representative of ice shelves and shallow

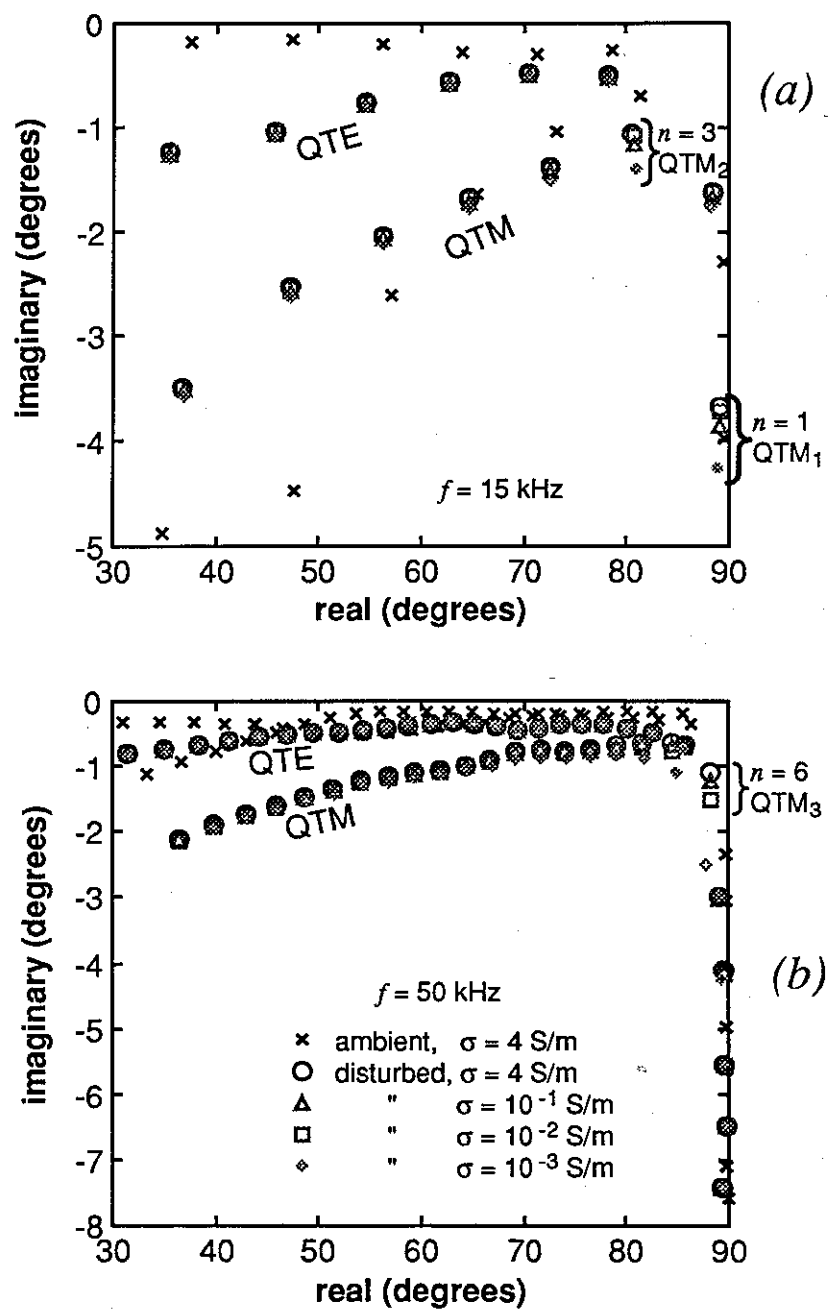


Figure 4.6: Eigenangle solutions for the different conductivities indicated and for (a) 15 and (b) 50 kHz signals.

ice-covered ground. The other set is for a very low Earth surface conductivity of $\sigma = 10^{-5}$ S/m and permittivity of $\epsilon_r = 5$ representative of deep ice caps such as those in Greenland and Antarctica [Hauser *et al.*, 1969]. For these conditions, and in particular over ice caps, the eigenangle solutions vary considerably from those described earlier in conjunction with Figure 4.4. Thus, for propagation over these regions of the Earth, the scattering from disturbances with altitude profiles such as those shown in Figure 4.3 is a sensitive function of the conductivity of the ground beneath the disturbance.

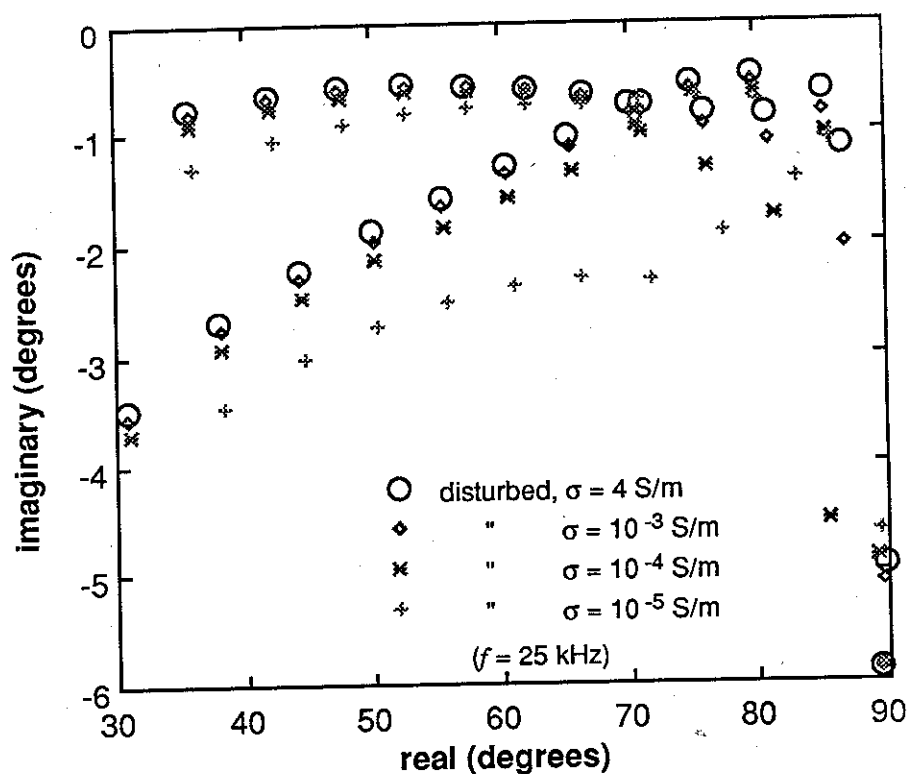


Figure 4.7: Eigenangle solutions for ice cap surface conditions.

4.3.2 Beamwidth of Density Enhancement Scatterers

Another important property of the type of scatterers defined by the altitude profiles of Figure 4.3 and having transverse extent of 50–200 km is depicted in Figure 4.8 for a representative case. Figure 4.8*b* shows a plot of the relative scattered signal strength calculated for each of the first ten modes of a 25 kHz signal as a function of the angle ψ (as depicted in Figure 4.8*a*) measured away from the forward-scatter direction. The scatterer used in the case shown was chosen to have a disturbed electron density profile labelled “II” in Figure 4.3 at its center (with density falling off with distance from the center in the manner described by Equation 4.11), and an effective radius a of 50 km, while the Earth surface conductivity and permittivity under the disturbance were respectively taken to be $\sigma = 4$ S/m and $\epsilon_r = 81$.

Notice that the main, forward, lobe of the scattered ‘radiation’ pattern is very similar (nearly identical) for every mode. Only the overall relative magnitude varies among the modes. The amplitudes of all the modes for scatter angles ψ outside the main lobe beamwidth are found to be uniformly much lower than the main lobe amplitudes for every non-negligible waveguide mode over the entire range of frequencies (15–50 kHz), effective radii (25–200 km), disturbed density profiles (profiles I–IV of Figure 4.3), and ground conductivities (10^{-3} –4 S/m) considered. In all the cases involving the gaussian-shaped (see section 4.2) disturbances considered in this research, only one main lobe is found as depicted in Figure 4.8. Figure 4.9*a* and *b* show the main lobe portion of the results of calculations for the same conditions as those of Figure 4.8*b* except they are for frequencies of 15 and 50 kHz, respectively. The general form of the main lobe is seen to be very similar at all three frequencies.

Figure 4.10 compares the main lobe of the scattered radiation patterns of four different disturbances with transverse radii $a = 100$ km, where each has a different peak disturbed ionospheric electron density profile (corresponding to profiles I, II, III, and IV of Figure 4.3). For comparison, the figure shows the scattering pattern of the same mode ($n = 3$) for each case. (Other parameter values are: $f = 25$ kHz, $\sigma = 4$ S/m, and $\epsilon_r = 81$.) This result illustrates the fact that the effective angular width of the main lobe of the

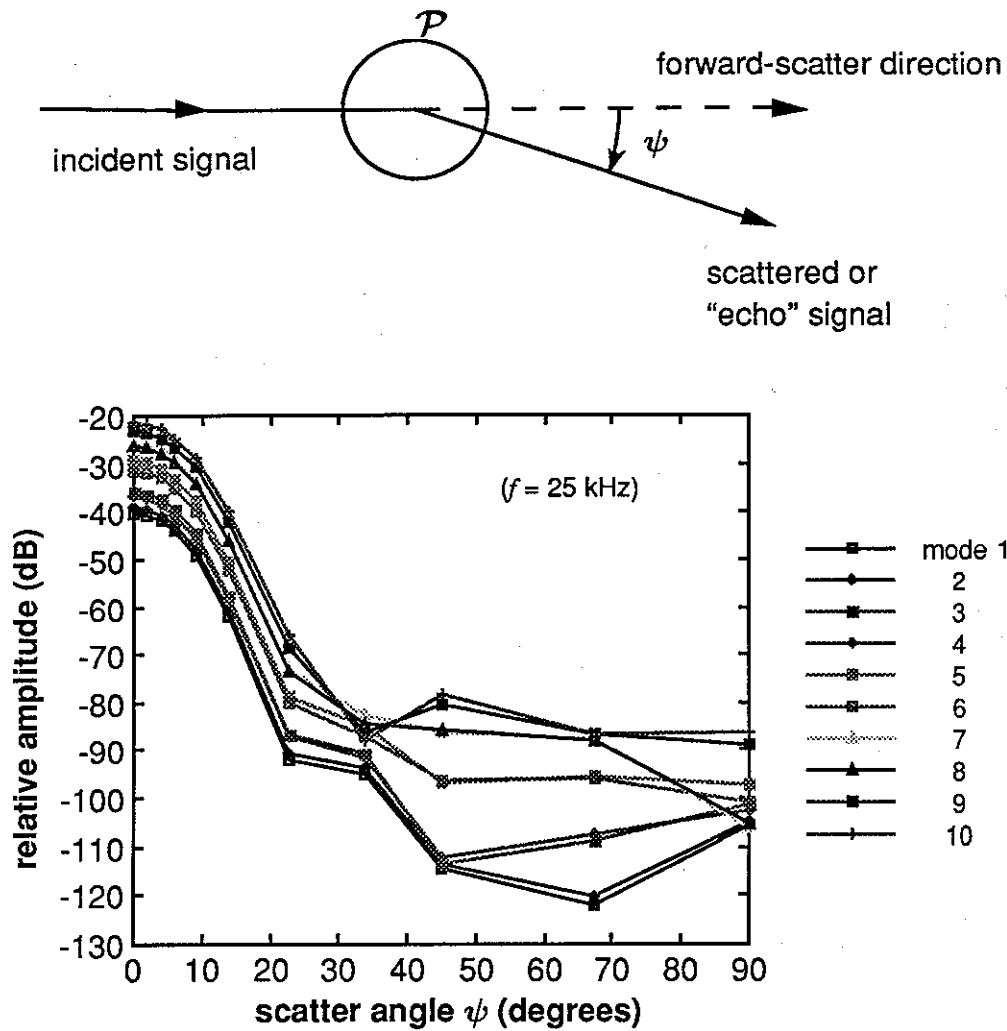


Figure 4.8: (a) Schematic description of the scattering geometry and the definition of angle ψ . (b) Scattered modal signal strength versus angle ψ for a 25 kHz signal and a disturbance 200 km in diameter. The density enhancement profile was assumed to be profile II from Figure 4.3 while the Earth surface conductivity and permittivity were taken to be $\sigma = 4$ S/m and $\epsilon_r = 81$.

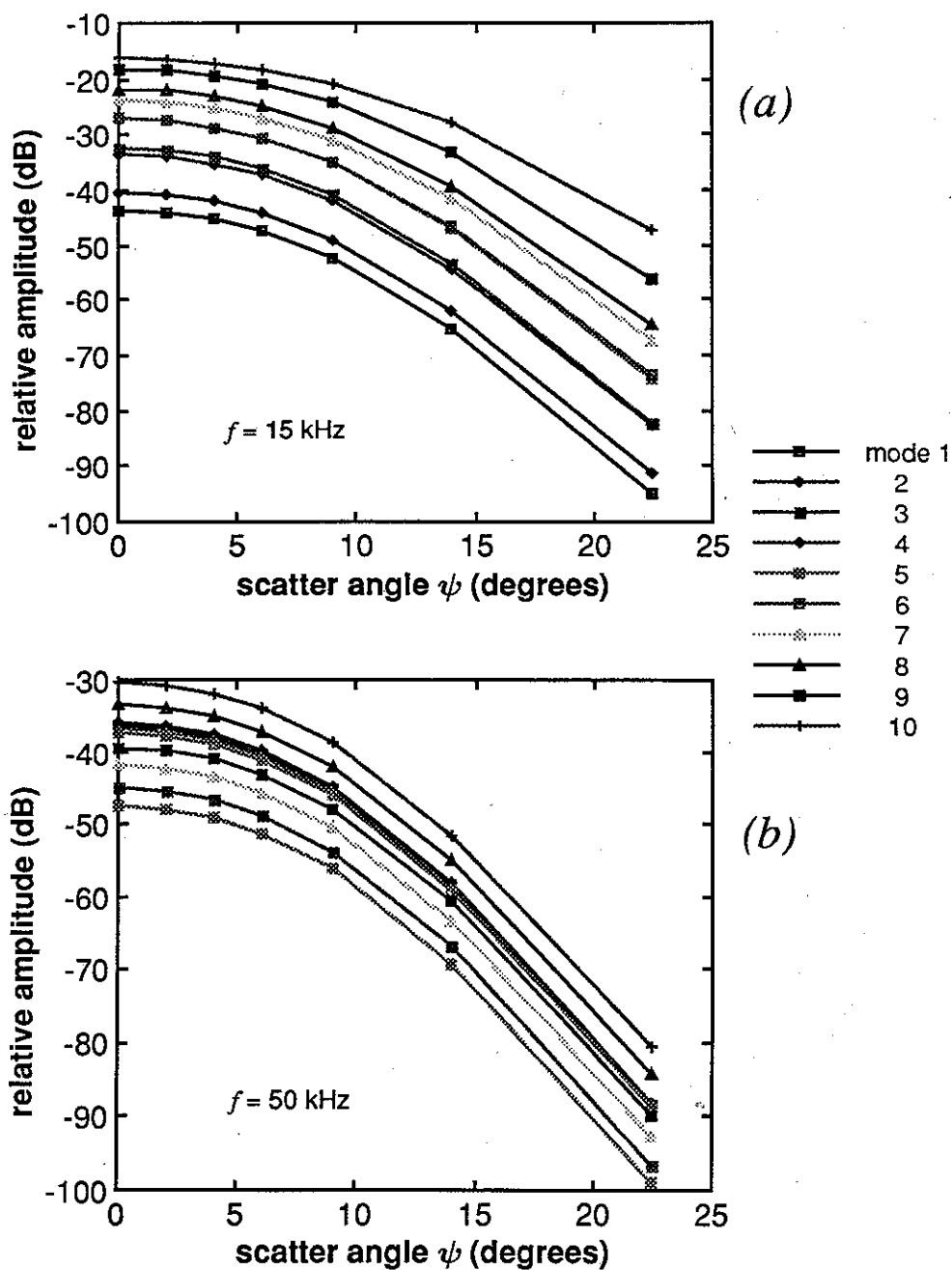


Figure 4.9: Scatter 'radiation' patterns for (a) 15 and (b) 50 kHz signals. All other parameters are the same as in Figure 4.8b.

scattered radiation pattern is insensitive to differences in the ionospheric electron density profile of the disturbance.

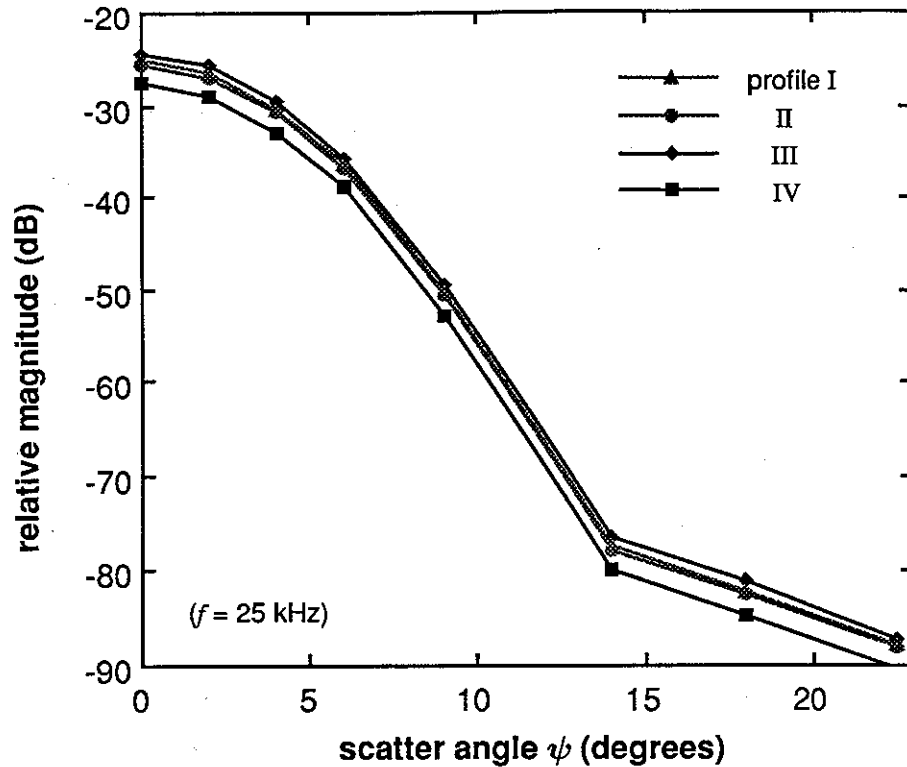


Figure 4.10: Scattered modal strength versus ψ for different disturbed density profiles I, II, III, IV as defined in Figure 4.3. All other parameters are the same as in Figure 4.8b.

Figure 4.11 compares the relative magnitudes of the scattered radiation patterns of an example waveguide mode ($n = 5$) for four disturbances of different effective radii ($a = 25, 50, 100$, and 200 km). Other parameter values for this example were taken to be $f = 25$ kHz, $\sigma = 4$ S/m, and $\epsilon_r = 81$, and profile I of Figure 4.3 was assumed to represent the altitude variation of density at the center point. Notice that for disturbances which have radii of 50 km or larger, the scattered signal strength at $\psi = 20^\circ$ is lower by more than 40 dB with respect to the forward scattered signal strength. Even for the relatively small 25-km radius disturbance, the scattered signal strength has diminished by

more than 30 dB for scatter angles $\psi \geq 35^\circ$. However, as can be seen for the forward scattered ($\psi = 0^\circ$) signal strength, the smaller disturbances scatter a relatively smaller amount of signal than the larger disturbances (as measured by the comparison of scattering magnitudes at $\psi = 0^\circ$). For example, the forward scatter for 25 km radius is ~ 25 dB lower than for 100 km radius, and 11 dB lower than for 50 km radius. Disturbances having radii smaller than 25 km were not considered because such small disturbances begin to violate the WKB approximation used in this model (see section 4.1.1). It also appears that the overall scattering effect of such small disturbances is lower, so that, generally, much larger density changes would be needed to produce the same amplitude and phase changes at the receiver.

Our results indicate that, for the type of disturbances considered here (Figure 4.3), most of the wave energy scatters within a fairly narrow ($\pm 20^\circ$) region to either side of the forward-scatter direction. An important implication of this finding is that if disturbances are located far enough away transverse to the GCP, the scattering angle ψ required for reception at the receiver end of the GCP would be greater than 20° and therefore, the effect of these disturbances on the received signal would be negligible. For frequencies and path characteristics considered in this work, we have found in general that most disturbances lying more than ~ 200 km to either side of the GCP have negligible effect on the signal seen at the receiver. This is because a scattered signal whose magnitude is more than ~ 35 dB below that of the direct, or main, signal perturbs the total signal strength at the receiver by less than 0.1 dB, which is the threshold measurement of transient amplitude changes in typical VLF data. A scattered signal having this same magnitude can perturb the phase at the receiver by a maximum of $\sim 0.6^\circ$.

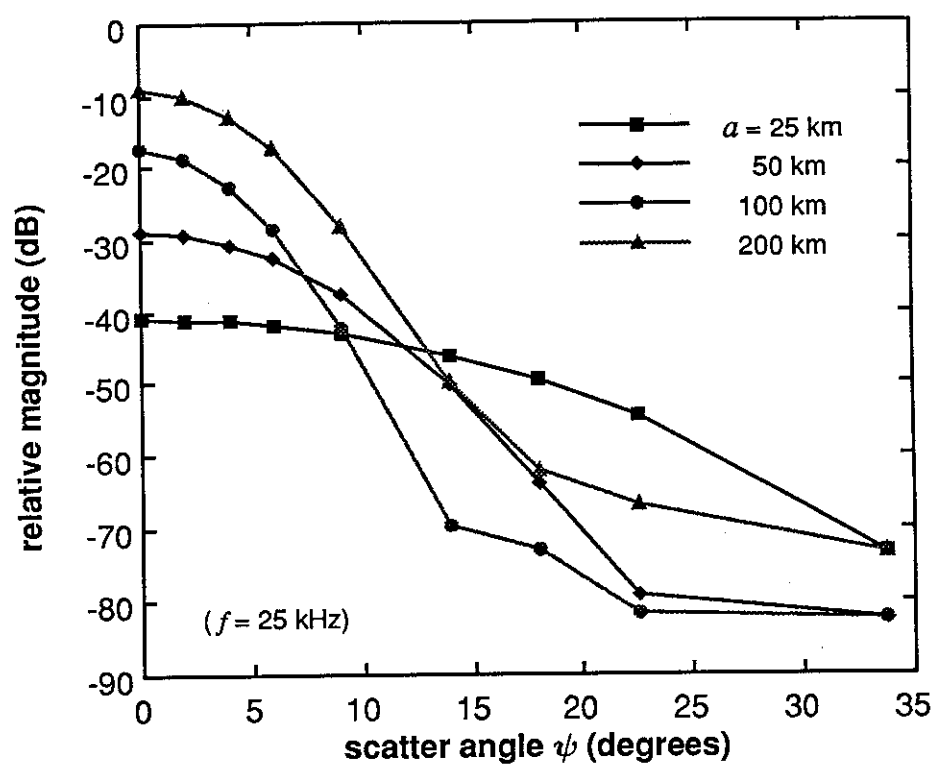


Figure 4.11: Scattered modal strength versus ψ for disturbances of different sizes, $a = 25, 50, 100$, and 200 . Profile I of Figure 4.3 was assumed for the disturbance profile. All other parameters are the same as in Figure 4.8.

Chapter 5

Single Mode 3-D Scattering Model

In this chapter we discuss a simple, single-mode-propagation version of the 3-D model of VLF wave propagation in the Earth-ionosphere waveguide in the presence of lower ionospheric disturbances. The methodology is explained and results are given for different cases, using typical parameter values, for which single mode analysis may be applicable. One such case that is addressed in particular is that of the propagation of 10–25 kHz waves over a long, all-sea-based path from the source to the receiver. Assuming that the ambient ionosphere does not change along the path and that a single ionospheric disturbance exists, which does not violate the WKB approximation [Budden, 1985], the problem reduces to the analysis of the propagation and scattering of a single ‘dominant’ mode. Substantial portions of this chapter and the content of sections 4.1 and 4.2 appeared in the *Journal of Geophysical Research* [Poulsen et al., 1990a].

5.1 Methodology

The results presented below were obtained by numerical evaluation of Equation 4.10 using realistic values for the different parameters d , a , y_o , x_T or x_R , S_n^o , and $S_n(r')$. All distances were normalized to units of wavelength (λ) and the following assumptions were made to facilitate comparison with published data, in particular with the results of Inan and Carpenter [1987] involving measurements of the 23.4 kHz NPM signal from Hawaii arriving on an $\sim 12,000$ km all-sea-based path to Palmer Station, Antarctica:

1. A long ($d = 800 \lambda$), all-sea-based, signal path from source to receiver (thereby making 'ground' conductivity and permittivity constant).
2. A single ambient density profile $N_e^\circ(h)$ for the lower ionosphere. Typical values of ambient density were obtained from the International Reference Ionosphere [Rawer *et al.*, 1978] for altitudes down to 95 km, below which, the ambient profile was assumed to have the form shown in Figure 5.1, in accordance with Reagan *et al.* [1981].
3. A single dominant mode arriving at the receiver. (For an $800\text{-}\lambda$ -long all-sea path at 20 kHz ($\lambda = 15$ km), our calculations, based on MODEFNDR, show the $n = 3$ [QTM₂] field component to be ~ 8 dB higher than the next highest mode, the $n = 1$ [QTM₁] component. However, the dominance of the 'dominant' mode may in general need to be more carefully assessed as discussed later in section 6.4.4.)
4. A single disturbance region, or "patch", having the general shape described by Equation 4.11.
5. Negligible mode coupling within the disturbed region.

With these assumptions Equation 4.10 was evaluated for (1) a series of patch radii a ranging from 0.15λ to 10λ (equivalent to a range of 2.3 km to 150 km at 20 kHz), (2) a series of patch location distances in the x direction (x_T) ranging from points 10λ from the transmitter to the path midpoint, i.e., 400λ in this case (equivalent to 150 km and 6000 km, respectively, at 20 kHz), and (3) a series of patch locations in the y direction (y_o) ranging from 0 to 20λ (equivalent to 0 and 300 km, respectively, at 20 kHz).

Since Equation 4.10 is symmetric both in the x direction about the midpoint of the GCP and in the y direction to either side of the GCP, a single 'quadrant' of the x - y plane between the transmitter and the receiver provides all non-redundant information about the received signal.

The numerical results presented in this chapter were obtained using the three different disturbed ionospheric electron density profiles shown in Figure 5.1. The three profiles, labeled I, II, and III (which are different from those of Figure 4.3), are taken to be

representative of the electron density at the location of maximum perturbation (x_o, y_o) as a function of altitude h resulting from electron precipitation bursts induced by lightning-generated whistlers propagating at $L = 2, 2.5$, and 3 , respectively. Again, these were obtained using the method of *Inan et al.* [1988a] as explained in section 4.2. The ambient nighttime D region electron density profile that is used is also shown for reference. The total precipitating electron energy flux density for each profile was adjusted so that the magnitude of the difference between the disturbed mode refractive index S_n (where $n = 3$ for this single mode case) and the ambient mode refractive index S_n^o was the same; i.e., $|S_3 - S_3^o|$ has been normalized to the same value for all three disturbance profiles shown in Figure 5.1. The resulting precipitated energy flux densities required to produce the disturbances represented by these profiles ranged from $\sim 2 \times 10^{-3}$ ergs $\text{cm}^{-2} \text{s}^{-1}$ for $L = 2$ to $\sim 4 \times 10^{-2}$ ergs $\text{cm}^{-2} \text{s}^{-1}$ for $L = 3$. The rationale behind this normalization is to ensure that any differences in scattering between the three profiles are due primarily to the differences in altitude distribution of electron density.

5.2 Results

The purpose of the calculations is to determine the effect of the modeled disturbance region on the change in amplitude ΔA and the change in phase $\Delta\phi$ of a single-mode VLF signal propagating over a long all-sea path. Numerical results for a few of the cases discussed above are presented in Figures 5.2–5.4. Figure 5.2 is a contour plot of the calculated change in signal amplitude (ΔA) and change in phase ($\Delta\phi$), *as seen at the receiver*, that would be produced by a disturbance whose center location (x_o, y_o) is varied in both the x and y directions over the range of values mentioned above. The result shown is for a disturbance with electron density profile I (of Figure 5.1) and an effective patch radius a of 5λ (60 km at 25 kHz). Figure 5.3 is a ‘slice’ along the y direction of the contour plot of Figure 5.2 at a fixed value of x ($x/d = 0.25$ in this example) but parametric in a , and shows the variation of ΔA and $\Delta\phi$ with transverse distance away from the GCP (i.e., in the y direction). Figure 5.4 shows the y dependence of the magnitude and phase of the scattered field e_n^s (where $n = 3$; see Equation 4.10 and

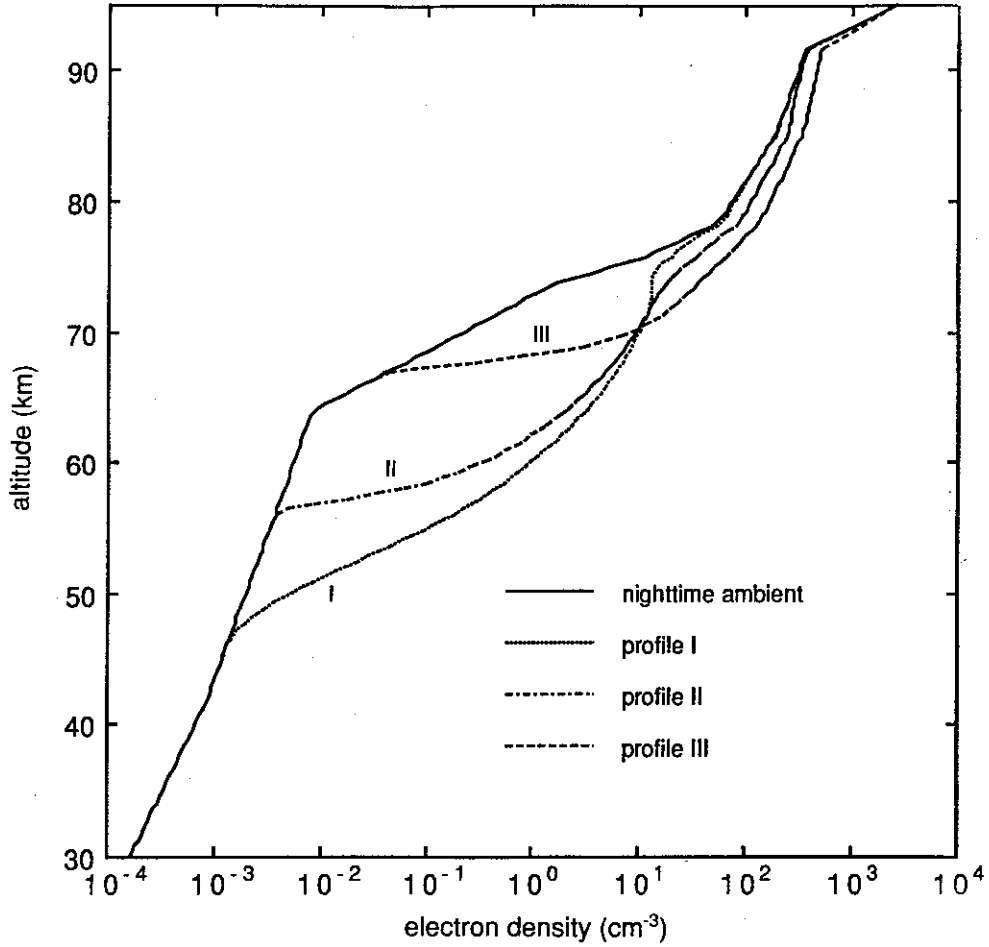


Figure 5.1: Plot of the ambient electron density distribution with altitude and three different ionospheric disturbance profiles used in the calculations. Profiles I, II, and III represent the electron density distribution with altitude at the location of maximum perturbation (x_o, y_o) resulting from electron precipitation bursts induced by lightning-generated whistlers propagating at $L = 2, 2.5$, and 3 , respectively. The total precipitating electron energy flux density for each profile has been adjusted such that the value of $|S_n - S_n^o|$ produced by each disturbed profile is the same. A typical value of 200 ms for the duration of the lightning discharge and the subsequent LEP burst has been assumed in the profile generation.

Figure 4.2), again at $x/d = 0.25$ and parametric in a . Several interesting aspects of the results shown in Figures 5.2–5.3 can be noted as follows:

1. Disturbances centered on the GCP produce an advance in the phase and/or a reduction in the amplitude of the received signal. For disturbances located off the GCP, any combination of positive or negative, amplitude or phase changes is possible depending on the patch location with respect to the transmitter or receiver, and to the GCP. (See Figure 5.3.)
2. The magnitude of the scattered modal field e_n^s continuously decreases with distance off the GCP (i.e., the y direction) as shown in Figure 5.4, becoming insignificant beyond $\sim 20 \lambda$. In terms of the phasor diagram shown in Figure 4.2, the length of the e_n^s vector continuously shrinks as the patch moves away from the GCP and thus the largest value of ΔA or $\Delta \phi$ possible also becomes smaller. This result is expected from the directional pattern of the scattered fields that were discussed in section 4.3.2, which indicated that the -40 dB beamwidth of the scattered field was approximately $\pm 20^\circ$ around the forward-scatter direction.
3. At a given patch location (x_o, y_o) , the amplitude of e_n^s is found to depend significantly on: (i) The magnitude of the difference, ΔS_n , between the mode refractive index at the peak of the disturbance $S_n(0)$ and the 'background' mode refractive index S_n° (in other words, $|\Delta S_n| = |S_n(0) - S_n^\circ|$). The value of ΔS_n depends on the electron density profile within the disturbance and on which modes are dominant at the disturbance. For the range of parameters considered, it was found that $|e_n^s|$ was proportional to $|\Delta S_n|$. It was also found that a given disturbance density profile generally produced different e_n^s for each waveguide mode. Thus, the effect produced by a given disturbance depends upon which mode is dominant at the patch location. (ii) The horizontal extent of the disturbance region. Near the GCP, as the radius a of the patch is increased, the magnitude of e_n^s is found to increase also (see Figure 5.4). Thus, the larger the patch size, in general, the larger the total VLF perturbation that is produced. However, at certain points either of the perturbation components ΔA , or $\Delta \phi$, may decrease as a increases depending on the phase of e_n^s with respect to that of e_n° (see Figure 5.3).

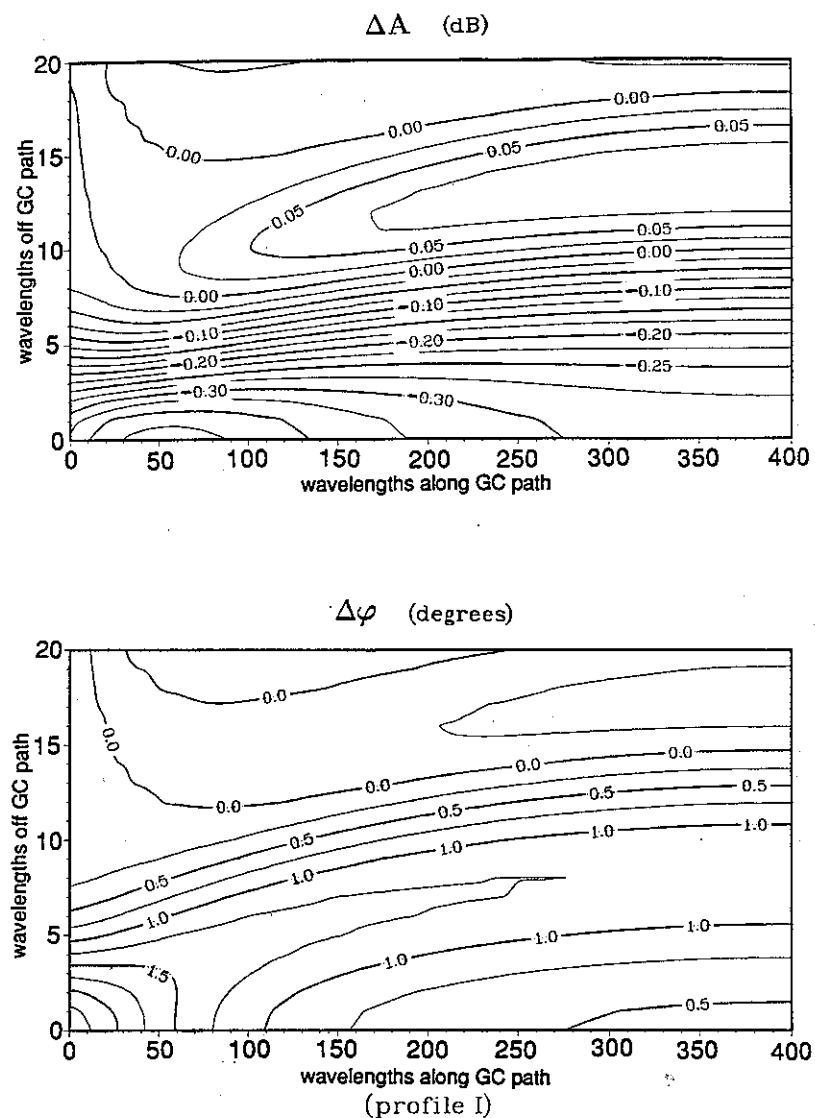


Figure 5.2: Contour plots of the calculated ΔA and $\Delta\phi$ seen at the receiver that would be produced by a circularly symmetric disturbance region with a horizontal Gaussian distribution whose center is moved in both the x (along the GCP) and y (off the GCP) directions over a range of values along the GCP of 10λ from the transmitter (or receiver) to the path midpoint (400λ), and over a range of values off the GCP of 0λ to 20λ away. The results shown were calculated using profile I of Figure 5.1 and an effective patch radius a of 5λ . The y dimension has been exaggerated for clarity.

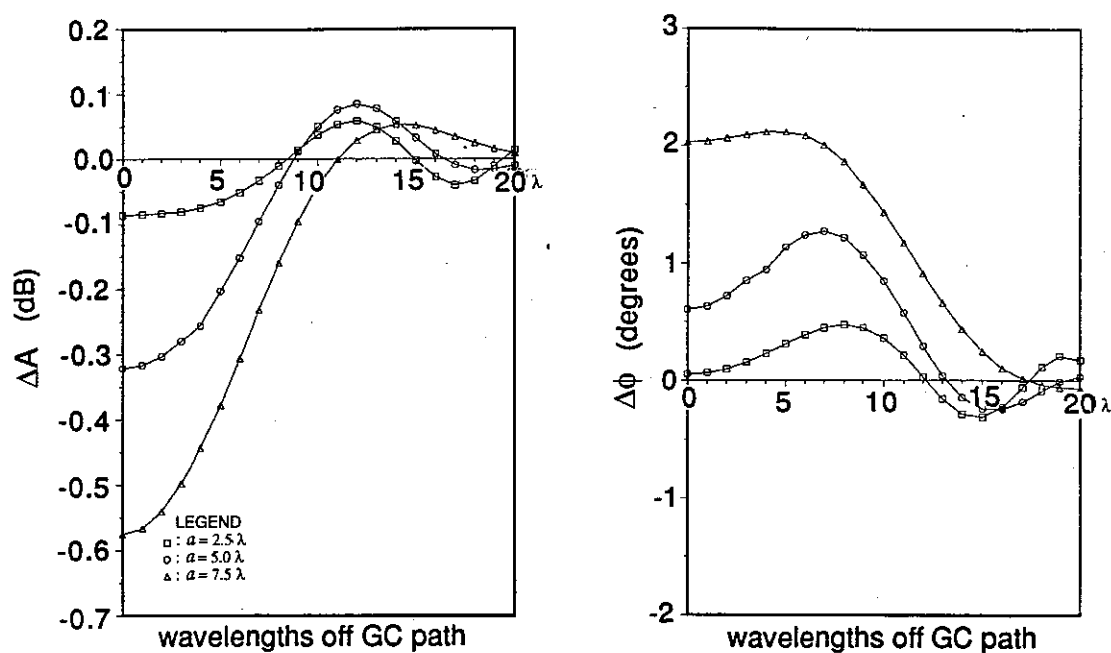


Figure 5.3: Two-dimensional 'cut' along the y direction of Figure 5.2 taken at a fixed value along the x axis ($x_T/d = 0.25$ in this case) showing the dependence of ΔA and $\Delta\phi$ on distance (in wavelengths) away from the GCP for three different values of effective radius a .

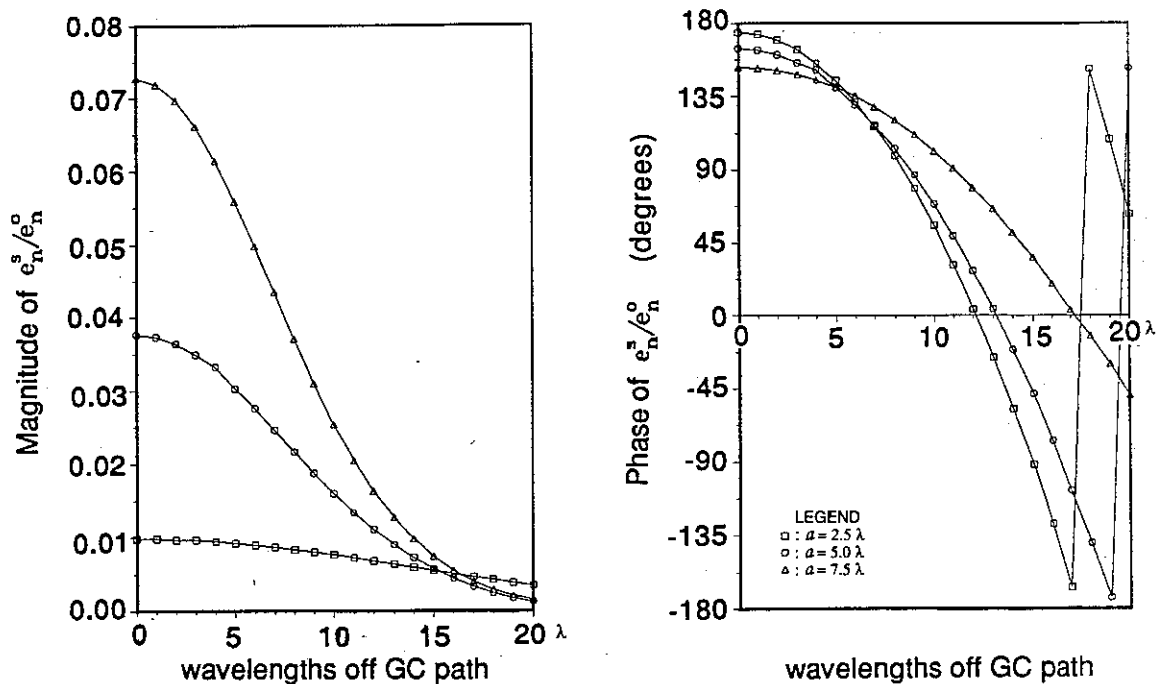
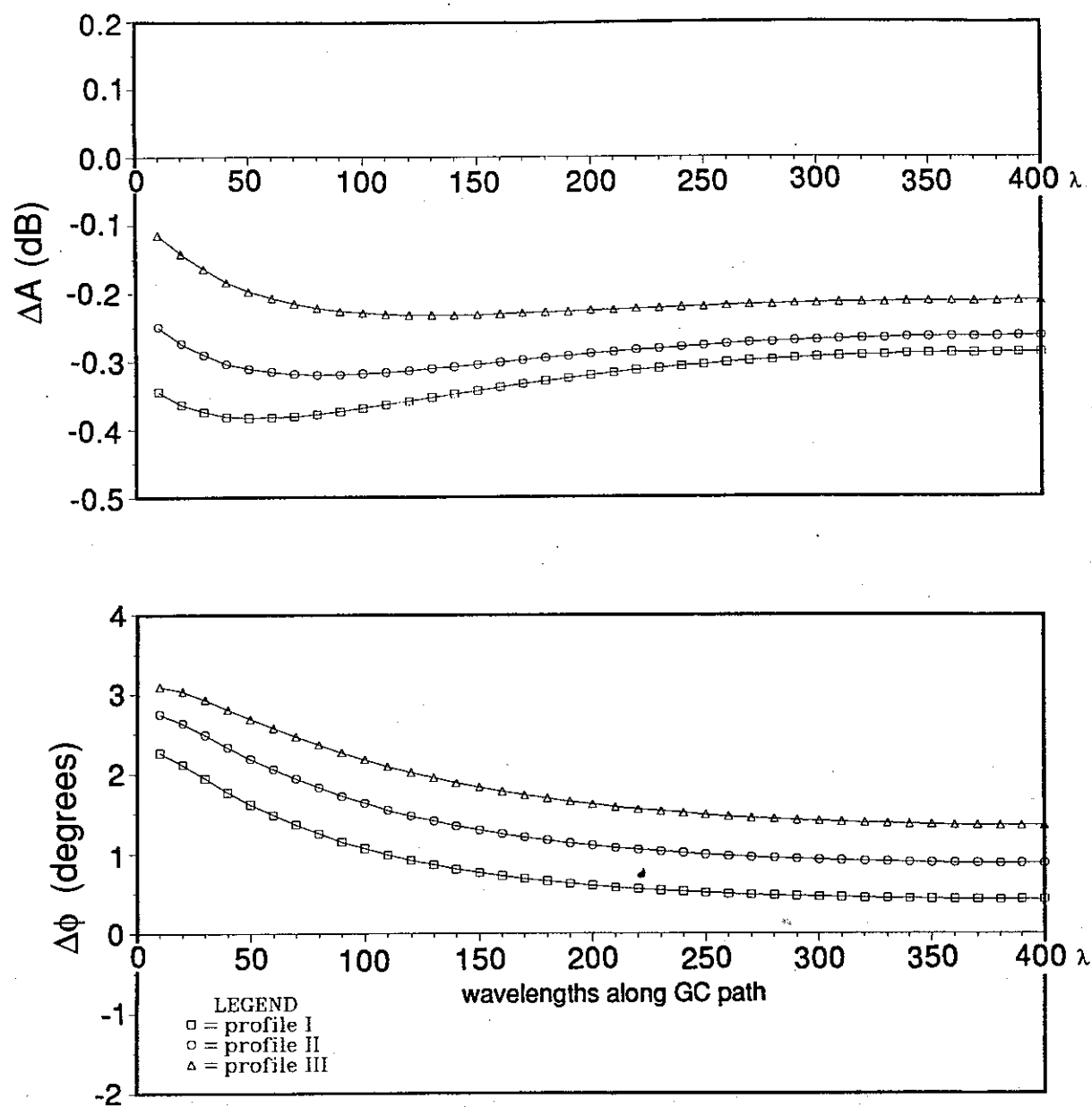


Figure 5.4: Plot showing the dependence of the magnitude and phase of the scattered signal e_n^s on distance (in wavelengths) away from the GCP for the same values of a and x_T/d as in Figure 5.3 and again using profile I of Figure 5.1. The values of $|e_n^s|$ and $\angle e_n^s$ are relative to those of the direct signal e_n^o .

4. Disturbance density enhancement profiles that extend to lower altitudes are in general found to cause larger changes in amplitude, yet smaller changes in phase, for single mode propagation, than those density enhancements that lie at higher altitudes but which have the same magnitude of ΔS_n as the deeply penetrating disturbances. Because of the dependence of $|e_n^s|$ on $|\Delta S_n|$, the density enhancement profiles shown in Figure 5.1 were normalized to the same $|\Delta S_n|$ in order to bring out the differences in ΔA and $\Delta\phi$ caused specifically by the differences in altitude distribution. In the context of lightning-induced electron precipitation, lightning-generated whistlers covering a constant frequency range and propagating at lower L -shells induce precipitation bursts of higher energy electrons that penetrate more deeply than do bursts induced by whistlers of the same frequency range propagating at higher L -shells (see Figure 5.1). This is illustrated in Figures 5.5a and 5.5b, which show curves of ΔA and $\Delta\phi$ calculated for a patch with an effective radius of 5λ , where each of the three curves in each plot are calculated for a disturbance patch having one of the three density profiles shown in Figure 5.1. Figure 5.5a shows the value of ΔA or $\Delta\phi$ along the GCP itself, and Figure 5.5b shows the value of ΔA or $\Delta\phi$ away (in the y direction) from a GCP point one-fourth of the total propagation path distance from the transmitter (or receiver). Comparing the curves in each plot, it can be seen that profile I of Figure 5.1, representing a disturbance at $L = 2$, produces greater maximum values of $|\Delta A|$ and smaller maximum values of $|\Delta\phi|$ than does profile III of Figure 5.1 representing a disturbance at $L = 3$ (with the same value of $|\Delta S_n|$ as profile I).
5. The values of ΔA and $\Delta\phi$ can in some cases be used to roughly determine the distance y_o from the GCP to the disturbance. For example, $\Delta A \sim 0$ when $y_o \sim 8\lambda$ for an effective patch radius of 5λ . (See Figure 5.2.)

5.3 Discussion and Comparison

As mentioned above, the parameters for the results shown in Figures 5.2–5.5 were chosen so as to facilitate direct comparison with experimental results on the NPM signal



(a)

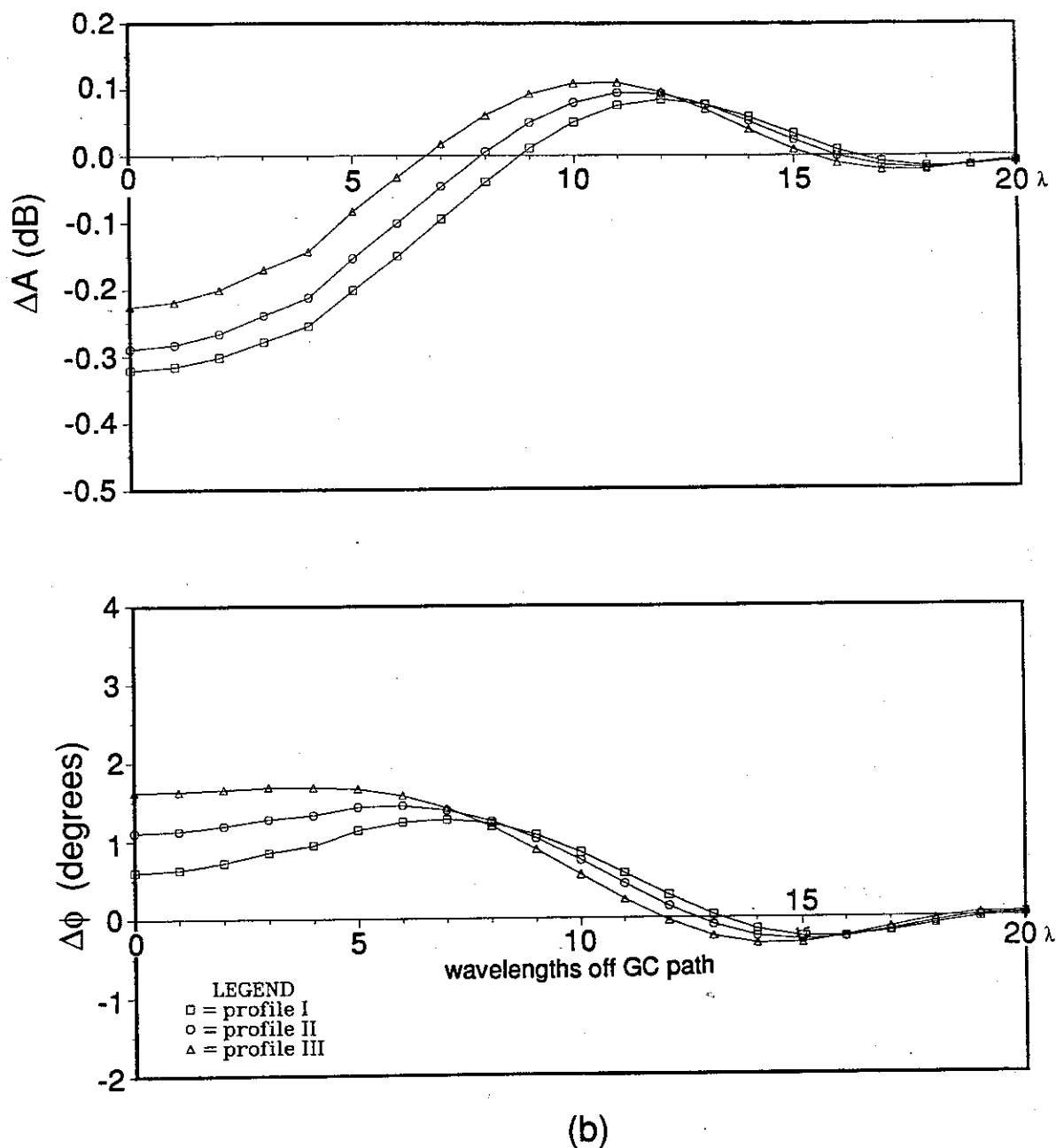


Figure 5.5: (a) Plots of ΔA and $\Delta \phi$ similar to those shown in Figure 5.4 except the two-dimensional 'cut' is taken along the x direction of Figure 5.2, along the GCP (i.e., for a fixed value along the y axis of $y_o = 0$). The effective radius a is fixed at 5λ and the three different curves of ΔA and $\Delta \phi$ are calculated using the three different disturbance density profiles of Figure 5.1. (b) Plots of ΔA and $\Delta \phi$ versus y similar to those shown in Figure 5.4 except that the effective radius was fixed at $a = 5 \lambda$ and the three curves shown represent the changes produced by the three density profiles of Figure 5.1 (the same as in Figure 5.5a). Again, x_T/d was fixed at 0.25 in this example.

received at Palmer Station, Antarctica [Inan and Carpenter, 1987]. The NPM transmitter frequency is 23.4 kHz ($\lambda = 12.8$ km) along an all-sea GCP of $\sim 12,335$ km (or 964λ), and the unperturbed signal at the receiver for these parameters consists basically of a single, dominant mode. Inan and Carpenter [1987] found that the distribution of phase perturbations typically peaked around $\Delta\phi \simeq 2.5^\circ$, and that the overwhelming percentage ($> 95\%$) of the events observed were positive phase, negative amplitude perturbations. More recent measurements [Wolf, 1990; Wolf and Inan, 1990] showed similar results and also found that the distribution of amplitude perturbations seen at Palmer typically peaked around $\Delta A \simeq -0.3$ dB. Our numerical results indicate that disturbance patches centered on or near the GCP always produce positive $\Delta\phi$ and negative ΔA values for single mode propagation, and that the strongest magnitude scattered signal strengths are produced by patches closest to the GCP. Thus, it appears that most Trimp events seen on the NPM–Palmer signal may be due to disturbances located close to or on the GCP.

It is of interest to consider the distribution of $|\Delta A|$ and $|\Delta\phi|$ over long time periods where a disturbance might be expected to appear at a wide range of locations. Figures 5.7a and 5.7b show plots of $|\Delta A|$ versus $|\Delta\phi|$ for a variety of patch sizes a and a regularly spaced grid of patch locations (x_o, y_o) for two specific disturbed density profiles $N_e(r', h)$, (profiles I and III of Figure 5.1, respectively). These figures are similar to Figure 11a of Inan and Carpenter [1987] or Figure 7 of Dowden and Adams [1988], reproduced here in Figure 5.6; however, the results shown in Figure 5.7 do not take into account the relative probability of occurrence of different size LEP patches nor the relative probability of occurrence of different locations of the patch with respect to the signal path. Rather, they show a range of ΔA -versus- $\Delta\phi$ values produced by a given disturbed density profile that can be expected on the basis of the present theory. In comparing Figure 5.7a with Figure 11a of Inan and Carpenter [1987], we note that the theoretical results are computed for a selected range of parameters that represent typical circumstances. In particular for Figure 5.7a, a range of patch radii a from 3.75λ to 10λ only was used together with the same density profile (profile I of Figure 5.1) for all of the values of the points. Profile I is representative of an energy flux density of $\sim 2 \times 10^{-3}$ ergs $\text{cm}^{-2} \text{s}^{-1}$ occurring at $L = 2$. Patch radii a larger than 10λ and/or energy flux densities greater than $\sim 2 \times 10^{-3}$ ergs $\text{cm}^{-2} \text{s}^{-1}$ would lead to $|\Delta A| > 0.9$ dB and/or $|\Delta\phi| > 6^\circ$. Any discrepancies between

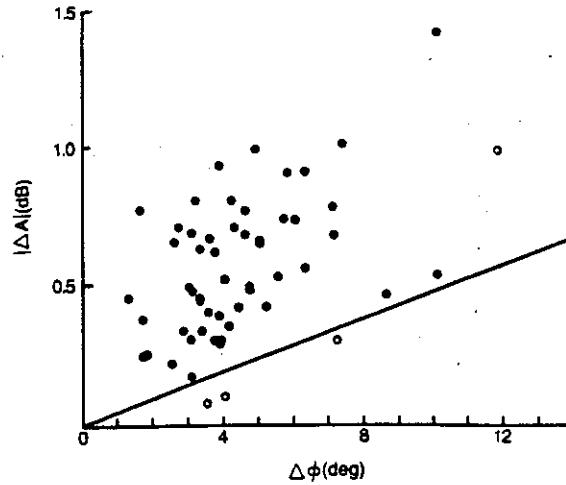


Figure 5.6: Figure 11a of *Inan and Carpenter* [1987] showing a comparison of measured simultaneous amplitude (ΔA) and phase ($\Delta\phi$) perturbation sizes on the NPM signal observed at Palmer Station, Antarctica. Data from 12 different periods during September–October 1983 are shown. In four of the periods fewer than three events could be scaled; these points are shown with open circles. The solid line shows the theoretically expected relationship of ΔA and $\Delta\phi$.

our Figure 5.7a and Figure 11a of *Inan and Carpenter* [1987], for example the fact that a number of the measured data points of *Inan and Carpenter* [1987] have $|\Delta A| > \sim 0.9$ dB or $|\Delta\phi| > \sim 6^\circ$ can be easily attributed to such variations in the parameter ranges.

While other recent work [*Inan and Carpenter*, 1987; *Dowden and Adams*, 1988, 1989a; *Cotton*, 1989] considered the ionospheric disturbances simply in terms of a reflection height change [*Ratcliffe*, 1959; *Hayakawa and Shimakura*, 1978], our results illustrate the critical dependence of ΔA and $\Delta\phi$ on the disturbed ionospheric density profile. One result is that the ratio of amplitude change to phase change, i.e., $|\Delta A/\Delta\phi|$, is larger for disturbance density enhancements lying at lower altitudes, such as what would be produced by LEP bursts at lower L -shells (e.g., see profile I of Figure 5.1) than for those lying at higher altitudes and corresponding to LEP events at higher L -shells (e.g., see profile III of Figure 5.1). This result is seen by comparing Figures 5.7a and 5.7b. Since the values plotted in Figure 5.7a correspond to a disturbance density

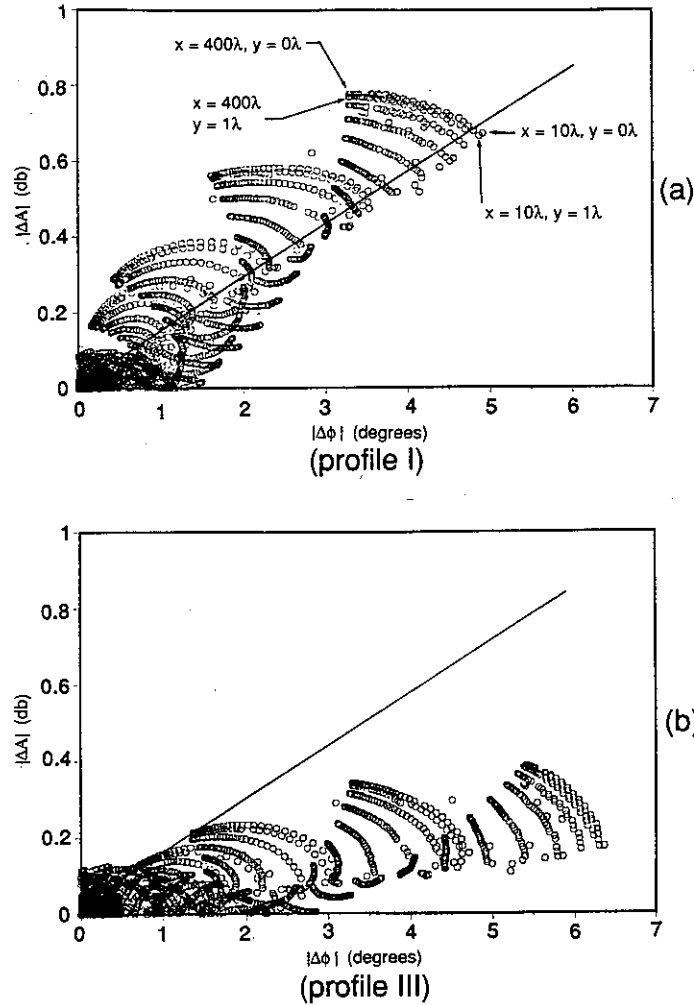


Figure 5.7: (a) A plot of calculated values of $|\Delta A|$ versus $|\Delta \phi|$ for a range of patch radii a from 3.75λ to 10λ , and a regularly spaced grid of patch locations (x_o, y_o) spaced 10λ apart in the x direction (ranging from 10λ to 400λ away from the transmitter or receiver) and 1λ apart in the y direction (ranging from on the GCP to 20λ off the GCP) for disturbance density profile I of Figure 5.1. Arrows indicate calculated values corresponding to disturbance patches located near the transmitter or receiver ($x = 10\lambda$) that lie on the GCP ($y = 0\lambda$) or 1λ away from it ($y = 1\lambda$), and patches located at the GCP midpoint ($x = 400\lambda$) that also lie either on the GCP or 1λ away from it. These outermost "arcs" of points in this figure correspond to a patch radius a of 10λ . For the outermost sets of points in this figure, as one travels along an arc from the end nearest the $|\Delta \phi|$ axis towards the end nearest the $|\Delta A|$ axis, the regularly spaced grid location of the center of the patch is traversed from $x = 10\lambda$ to $x = 400\lambda$, while moving from arc to arc towards the origin corresponds to increasing distance away from the GCP (i.e., the y direction). The outermost set of arcs corresponds to the largest patch radius used. The relative probability of occurrence of different size patches or of different locations is not taken into account in this figure. The line represents a $|\Delta A|/|\Delta \phi|$ ratio of 0.14 dB/degree. (b) A plot similar to Figure 5.7a except that disturbance density profile III of Figure 5.1 was used in the calculations instead of profile I.

enhancement lying at a lower altitude than that of the values plotted in Figure 5.7b (i.e., profile I versus profile III of Figure 5.1), the ratio $|\Delta A/\Delta\phi|$ of points in Figure 5.7a is larger than such a ratio of the corresponding points in Figure 5.7b (Figures 5.7a and 5.7b differ only in the disturbed density profile used in their calculation). As a consequence, it can be seen that the 'average' slope of the envelope of the points plotted in Figure 5.7a is higher than that of the envelope of points plotted in Figure 5.7b.

Another interesting feature of our results relating to the use of electron density profiles to model disturbance effects rather than the use of effective reflection height changes is that the ionospheric disturbance profiles shown in Figure 5.1 do not actually lead to significant changes in effective reflection height for the waveguide modes. For example, the maximum change in effective reflection height calculated by our model is produced by profile III and has the small value $\Delta h \sim 2$ km. Thus, the wave perturbations in our model are produced mainly by the ionization which lies below the effective reflection height, and the actual change in reflection height is a secondary effect in producing the perturbations. In contrast, some of the modeling work of *Dowden and Adams* [1989a] has relied on reflection height changes of ~ 15 km to produce ΔA and $\Delta\phi$ values comparable to measured ones. In view of this circumstance, we believe that it can be physically misleading to describe waveguide perturbations in terms of effective reflection height changes.

Dowden and Adams [1988] suggest that the Trimpi events they studied were produced by small LEP patches, and that there was no statistical correlation between the 'echo' (scattered) magnitude $|e_n^s|$ and the 'echo' phase $\angle e_n^s$. Based on this assumption, they hypothesized that the expected value of the scattered magnitude and scattered phase was the same, i.e., $\langle e_n^s \rangle \simeq \langle \angle e_n^s \rangle$. This corresponds to a line drawn on a $|\Delta A|$ - $|\Delta\phi|$ plot with a slope of 0.14 dB/degree. However, we find that based on our model, the results predict a different behavior for the scattered signal phase $\angle e_n^s$. It is interesting to note that when a line with slope 0.14 dB/degree is plotted in Figures 5.7a and 5.7b, it passes through the midst of many more of the points in plot a representing signal changes caused by a disturbance located at $L = 2$ than in plot b representing the same effect at $L = 3$. The 'average' slope of the envelope of points plotted in Figure 5.7b corresponding to

disturbances at $L = 3$ has a smaller value than that of the envelope of points plotted in Figure 5.7a corresponding to disturbances at $L = 2$; and this ‘average’ slope is found to increase as the location of the disturbance causing the signal changes is moved to lower L -shells (using the density distribution model described by *Inan et al.* [1988a]). Thus, the ‘average’ slope of the envelope of $|\Delta A|/|\Delta \phi|$ points plotted for a disturbance located at or near Palmer, which is located at $L \simeq 2.3$, would lie somewhere between that of Figure 5.7a, corresponding to $L = 2$, and that of Figure 5.7b, corresponding to $L = 3$, being somewhat closer to that of Figure 5.7a than that of Figure 5.7b. It is interesting to observe that the theoretical 0.14 dB/degree slope calculated by *Dowden and Adams* [1988] also lies between the ‘average’ slope of the points of Figure 5.7a and that of Figure 5.7b, but is closer to that of Figure 5.7a. Thus, if the measured data points plotted in Figure 11a of *Inan and Carpenter* [1987] correspond to disturbances somewhere near Palmer (located, say, between $L = 2$ and $L = 2.3$), it may be fortuitous that a line with slope of 0.14 dB/degree passes through their midst.

Dowden and Adams [1988] suggest that the disturbance patch is an inverted pimple or ‘stalactite’ of small horizontal dimensions. The model described in this paper indicates that as the horizontal size (e.g., radius a) of the disturbance is increased, the magnitude of e_n^s also increases (Figure 5.4). For the realistic ionospheric parameters used in our calculations, we find that the change in effective reflection height (Δh) produced by disturbance profiles such as those shown in Figure 5.1 is small ($\Delta h \leq \sim 2$ km), and that patches with small ($a < 1\lambda$) horizontal extent simply do not diffract enough signal to affect the ‘direct’ signal e_n^o significantly. In most cases when $a < \lambda$, the value calculated for $|e_n^s/e_n^o|$ is much less than -30 dB, which was the typical value *Dowden and Adams* [1988] suggested according to their calculations for the strength of the scattered signal relative to the direct signal. *Dowden and Adams* [1989a] suggest the existence of elongated disturbance stalactites or ridges produced by electron precipitation arcs aligned with an L -shell to explain Trimpi events measured at Dunedin, New Zealand. They again suggest that $\Delta h \simeq 15$ km which is much larger than what we find is produced by the density profiles used in our calculations. They explain that the location of such elongated stalactites is restricted to regions where some segment of an ellipse of constant echo signal delay (with the transmitter and receiver as foci) is within a few degrees

of L alignment and suggest that the lack of this requirement may prevent the use of their model for explaining Trimpi events measured on other paths such as the NPM-Palmer path mentioned in this paper. A plan view of their ridge-like depression is approximately elliptical and is parallel to the NWC-Dunedin GCP. Equation A.16 of Appendix A indicates that the strength of the scattered field of an elliptical disturbance patch with Gaussian density distributions along each axis of the ellipse in the horizontal plane is linearly proportional to disturbance length parallel to the GCP. Thus, there is some similarity between the results of *Dowden and Adams [1989a]* and our model. However, we note that our formulation assumes the density profile within and around the patch to be slowly varying (with vertical and horizontal distance) in order for mode coupling to be negligible and for the Born approximation to hold. Thus, a multiple-mode, non-Born-approximation model would be necessary to truly test the stalactite hypothesis.

For reasonable $S_n(r')$ shapes and ionospheric electron density profiles, we obtain values for ΔA and $\Delta\phi$ that are of the same order of magnitude as those measured on NPM-Palmer signals (i.e., $\Delta A \sim -0.3$ dB, $\Delta\phi \sim 3^\circ$). *Tolstoy et al.*'s [1986] multiple-mode 2-D theory predicts a range of values for ΔA and $\Delta\phi$ on the NPM-Palmer path of -0.08 to -0.34 dB and -0.46 to $+6.0$ degrees, respectively. Although some of these values are comparable to those of Figure 5.3, it is not possible to compare the results of our 3-D theory with the *Tolstoy et al.* [1986] 2-D theory since the *Tolstoy et al.* [1986] results include strong mode-coupling effects while our WKB theory neglects these effects. Nevertheless, the ionospheric density profiles used by *Tolstoy et al.* were based on monoenergetic electron precipitation, whereas the profiles we used to model the disturbances are more realistic (see section 4.2).

5.4 Summary and Conclusions

We have presented in this chapter, single mode results from a three-dimensional model of subionospheric VLF propagation in the presence of localized D region irregularities of the kind produced in lightning-induced electron precipitation events. This formulation allows us to estimate the magnitude and phase at the receiver of the electric field as it is affected

by scattering from ionization disturbances which lie off the great circle propagation path. Our results, using typical values for the ionospheric parameters, correspond well with actual values of amplitude and phase changes measured on a signal path having similar physical parameters as those assumed in the model, namely, single-mode propagation over a long sea-based path. It is found, for example, that modest ionospheric disturbances within $\sim 10 \lambda$ of the GCP can produce amplitude and phase changes of the same sign and order of magnitude as the large majority of LEP events measured on the NPM signal at Palmer Station, Antarctica. The specific details of the altitude profile of the disturbance is found to have a significant effect both on the magnitude of the scattered signal and on the ratio of amplitude changes to phase changes caused by such a disturbance. In the context of lightning-induced electron precipitation, the disturbed profile produced by a precipitation burst at a lower L -shell has a higher density enhancement at lower altitudes, and produces a higher $|\Delta A/\Delta \phi|$ ratio, than does a profile produced by precipitation at a higher L -shell. We also find that the values of ΔA and $\Delta \phi$ can be used to give a rough estimate of the distance from the GCP to the disturbance.

In this chapter it was assumed that the ionization disturbance varies smoothly with radius and that a single mode is dominant. However, more abrupt horizontal distribution profiles violate the slowly varying approximation, and thus, most likely produce additional modes through mode coupling. If this occurs close enough to the receiver that the additional modes are of comparable strength, effects more complicated than those predicted by a single-mode model would occur. In the next chapter, we extend the single-mode formulation to a multiple-mode WKB model which can account for the presence of multiple modes incident on the disturbed region and at the receiver.

Chapter 6

Multiple Mode Scattering Model

6.1 Introduction

In the previous chapter, we considered a single-mode method of modeling the effects of scattering caused by localized enhancement disturbances (also referred to as scatterers) in the lower ionosphere. The entire ambient path was considered to be horizontally homogeneous, and the disturbances considered were assumed to involve gradual (i.e., slowly varying) changes in electron density over distances in the horizontal direction of the order of a wavelength, thus allowing the use of the WKB approximation. Also, the maximum change in electron density from the ambient values was assumed to be of sufficiently small magnitude that the Born approximation could be used within the scattering region. This single-mode scattering method can be extended to the case of multiple modes in the WKB limit. In this chapter we consider more realistic great circle propagation paths by taking into account conversion between the different modes as the signal propagates along paths which have changing ground conductivities and permittivities *i*) between the transmitter and receiver, *ii*) between the transmitter and the disturbance, and *iii*) between the disturbance and the receiver. We extend the single mode method to take into account all non-negligible modes that arrive at and are scattered by the disturbance. However, we continue to assume that the nature of the disturbance is such that the WKB approximation still holds, and that, therefore, mode conversion within the scattering disturbance region can be neglected.

For the case of a single dominant waveguide mode, it was found (as described in the previous chapter, and by *Poulsen et al.* [1990]) that the scattering effect of a localized electron density enhancement is dependent on the altitude profile of ionization in the disturbed region. In other words, it was found that the disturbance should not merely be treated as a reflective scatterer, but that rather, the actual altitude profile of electron density within the disturbance (as compared to the ambient density profile) must be considered in determining the effects that a particular disturbance will have on the propagating VLF wave. Figure 6.1 shows an electron density disturbance profile (as well as a typical ambient density profile) that would be expected to occur at the center of a disturbance produced by an LEP event at $L \sim 2.0$ [*Inan et al.*, 1988a]. (The disturbed density profile shown here is the same as profile III of Figure 4.3.) The altitude profile of enhanced ionization within the disturbed region is expected to be an important determinant in the more general multiple-mode cases as well, especially since each waveguide mode is scattered a different amount relative to the other modes of the wave by the same disturbance.

6.2 The Model

The underlying methodology of the multiple-mode 3-D model is depicted in Figure 6.2. Basically, the Long Wave Propagation Capability (LWPC) developed by the Naval Ocean Systems Center (NOSC) [*Pappert and Snyder*, 1972; *Ferguson and Snyder*, 1987], as described in Chapters 2 and 3, is used to calculate the complex signal strength of the wave as it travels along the direct path between the transmitter and receiver ('direct path'), and along the paths from the transmitter to the disturbance ('leg 1') and from the disturbance (or scatterer) to the receiver ('leg 2'), taking into account the changes in ground conductivity and consequent multiple mode propagation which occurs along each path. In addition, the single-mode 3-D method described in the previous chapter is used to calculate the magnitude and phase of the signal scattered by the disturbance towards the receiver on a mode-by-mode basis, assuming that no conversion among modes occurs within the disturbed region. (This assumes that the WKB approximation is valid; in other

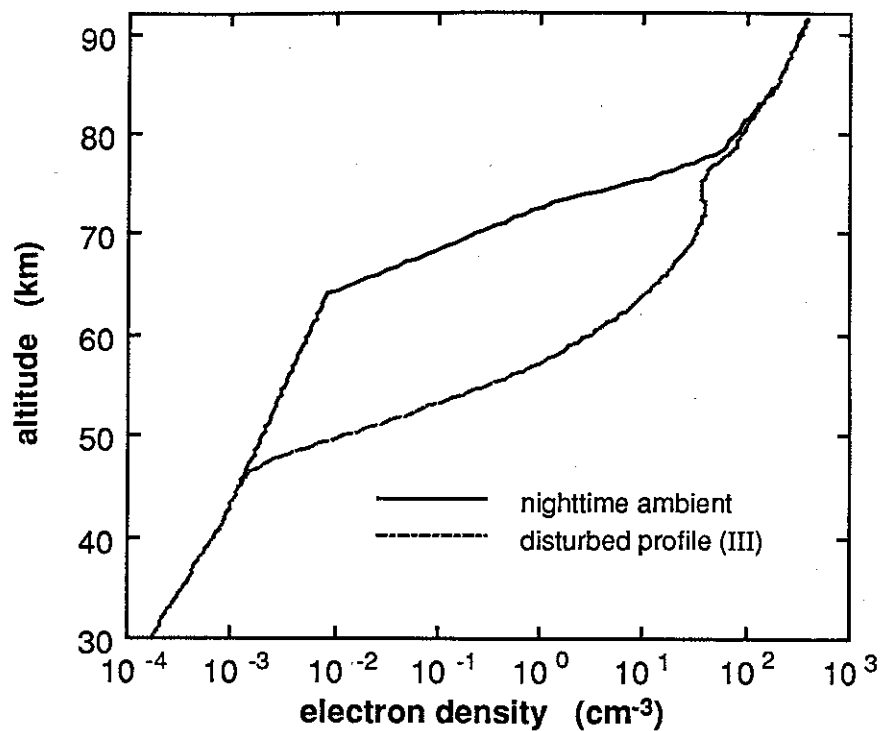


Figure 6.1: Plot of the electron density distribution versus altitude at the center of a disturbance produced by an LEP event induced by whistlers propagating at $L \sim 2.0$. A typical value of 200 ms for the duration of the lightning discharge and subsequent LEP burst and a precipitated electron flux of 5×10^{-3} ergs $\text{cm}^{-2} \text{s}^{-1}$ has been assumed in the profile generation. The ambient density profile used in the study is also shown.

words, that any variations in the ionospheric or ground properties are gradual and small over distances of $\sim 1\lambda$ in the horizontal directions.)

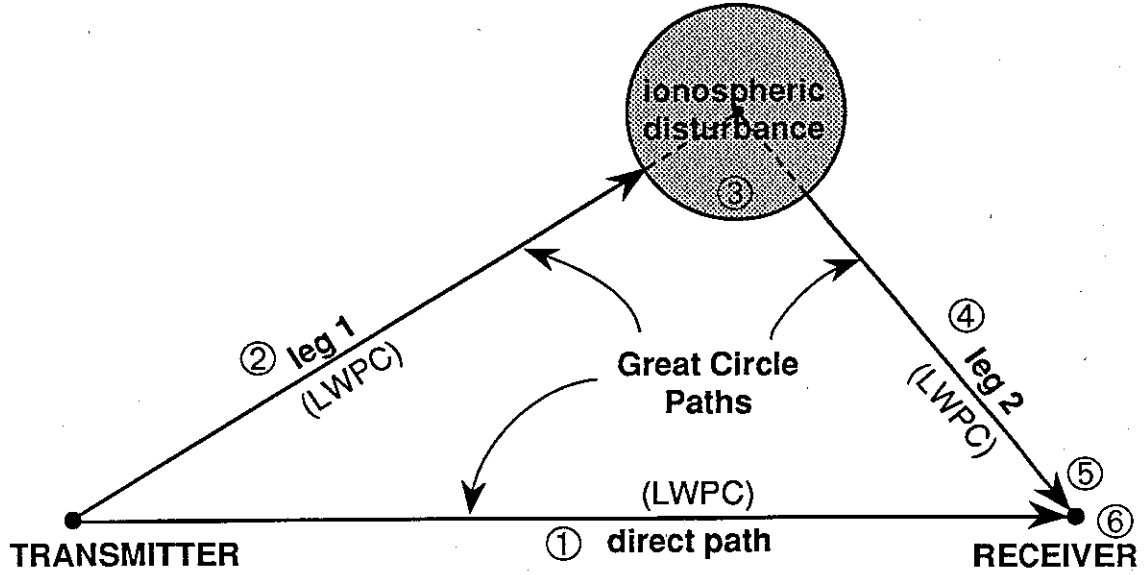


Figure 6.2: A depiction of the methodology used to calculate the total perturbed value of the electric field observed at the receiver. The numbers correspond to the numbered items given in the text of section 6.2.3. The Long Wave Propagation Capability (LWPC) is used along the three great circle paths shown, and the single-mode 3-D methodology explained in *Poulsen et al. [1990]* is used on a mode-by-mode basis within the ionospheric perturbation region. See text.

The single mode formulation described in the previous chapter can be extended to apply to the case of multiple mode propagation and scattering by combining Equations 2.3 and 4.4 to write

$$E_{total} \simeq \sum_n A_n^{T,R} [e_n^o + e_n^s] = \sum_n A_n^{T,R} e_n^o + \sum_n A_n^{T,R} e_n^s \quad (6.1)$$

where

$$e_n^o \simeq \frac{e^{-ik_o S_n^o d}}{\sqrt{|\sin(d/R_E)|}} \quad (6.2)$$

and

$$e_n^s = \left(\frac{-ik_o^2}{4} \right) \iint_p [S_n^2(x', y') - (S_n^o)^2] e_n(x', y') H_0^{(2)}(k_o S_n^o R') dx' dy' \quad (6.3)$$

as before. Now if instead we make the same substitutions as were made in Chapter 4, in particular, using the Born approximation (i.e., substituting e_n^o for e_n in the integrand) and substituting Equations 4.6 and 4.8 for e_n^o and $H_0^{(2)}$ respectively, we can write

$$E_{total} \simeq \sum_n A_n^{T,R} \frac{K e^{-ik_o S_n^o d}}{\sqrt{d}} + \sum_n A_n^{T,R} \left(\frac{-ik_o^2}{4} \right) \iint_p [S_n^2(x', y') - (S_n^o)^2] \times \left\{ \frac{K e^{-ik_o S_n^o R_o}}{\sqrt{R_o}} \right\} \left\{ \left(\frac{2i}{\pi k_o S_n^o} \right)^{\frac{1}{2}} \frac{e^{-ik_o S_n^o R'}}{\sqrt{R'}} \right\} dx' dy' \quad (6.4)$$

where all the variables have been previously defined.

6.2.1 Cylindrical Spreading on a Spherical Surface and the LWPC Code

Equation 4.6 (i.e., $e_n^o \simeq K e^{-ik_o S_n^o d} / \sqrt{d}$) represents a far-field approximation for a cylindrically spreading wave. It does not, however, account for the fact that on the Earth the wave is cylindrically spreading over a spherically curved surface. Equation 6.2 is a more accurate representation of the wave's spreading with propagation distance on the surface of the Earth [Wait, 1970; Ferguson and Snyder, 1980]. If we equate Equations 4.6 and 6.2 and use the small angle approximation $\sin x \simeq x$ for $x \ll 1$, then we find that $K = \sqrt{R_E}$ for $d \ll R_E$.

The LWPC code calculates the electric field versus distance using Equation 6.2 which is a more accurate representation of Equation 4.6. Since we use the LWPC code to calculate the propagating field components along the three propagation paths illustrated in Figure 6.2, we need to account for the discrepancy between the two representations for e_n^o in the final formulation of the scattered field integral. Thus, we define

$$e_n^{LWPC}(x) \equiv A_n^{T,R} \frac{K e^{-ik_o S_n^o x}}{\sqrt{|\sin(x/R_E)|}} \quad (6.5)$$

and then using $K = \sqrt{R_E}$, we make the following substitution:

$$A_n^{T,R} \frac{K e^{-ik_o S_n^o x}}{\sqrt{x}} \longleftrightarrow e_n^{LWPC}(x). \quad (6.6)$$

Using this substitution in Equation 6.4 (and rearranging), we find

$$E_{total} \simeq \sum_n e_n^{LWPC}(d) + \sum_n \left(\frac{-ik_o^2}{4} \right) \left(\frac{2i}{\pi k_o S_n^o} \right)^{\frac{1}{2}} \times \iint_p [S_n^2(x', y') - (S_n^o)^2] \{e_n^{LWPC}(R_o)\} \left\{ \frac{e^{-ik_o S_n^o R'}}{\sqrt{R'}} \right\} dx' dy' \quad (6.7)$$

The Hankel function term in the integrand of Equation 4.4 essentially represents the re-radiation of each modal field towards the receiver over a flat Earth by each infinitesimal area element of the disturbance being integrated by the double integral. The double integral then is “summing” the contributions to the scattered signal of all the infinitesimal radiators making up the disturbed region. We can extend the $e^{-ik_o S_n R'}/\sqrt{R'}$ portion of the asymptotic expansion of the Hankel function term to account for the sphericity of the Earth’s surface again by using Equation 6.5. This means that we can take advantage of the LWPC code to calculate the propagation of the scattered signal from the disturbance to the receiver location *and* account for the spherical surface over which it propagates. Equation 6.7 can thus be rewritten as

$$E_{total} \simeq \sum_n e_n^{LWPC}(d) + \sum_n c_n \times \iint_p [S_n^2(x', y') - (S_n^o)^2] \{e_n^{LWPC}(R_o)\} \left\{ \frac{e_n^{LWPC}(R')}{A_n^{T,R} K} \right\} dx' dy' \quad (6.8)$$

where

$$K = \sqrt{R_E}$$

and

$$c_n = \left(\frac{-ik_o^2}{4} \right) \left(\frac{2i}{\pi k_o S_n^o} \right)^{\frac{1}{2}}. \quad (6.9)$$

6.2.2 Simplifying Computational Approximations

Given enough computer time and patience, Equation 6.8 can be used as written to calculate the total perturbed electric field caused by a lower ionospheric disturbance taking into

account multiple mode propagation and mode coupling over a real Earth but neglecting mode conversion within the disturbed region. However, the LWPC code must then be run to and from each infinitesimal area element of the double integration (\mathcal{P}). In order to reduce the very large amount of computer time required to do so, we assume that the spatial variation of the underlying ground conductivity along all paths going from the transmitter to all points within the disturbance region are the same. We further assume the same to be true for all paths leading from all the points within the disturbance region to the receiver, and choose the paths leading to (i.e., R_{oc} in Figure 6.3), and from (i.e., R'_c), the center of the disturbed region as the representative paths. Thus, the ground conductivity along any radius within one of the two sectors shown in Figure 6.3 is assumed to be identical to that along the center radius of that sector, respectively. This is a reasonable approximation because the angles subtended by such sectors are usually very small (typically $< 5^\circ$) for longer paths, and for short paths, the wave does not propagate far enough to be significantly affected by any large changes in ground conductivity between the disturbance and the transmitter (or receiver). In the rare instances that the boundary between two regions of significantly different conductivity is nearly parallel to the centerline of the sector, and lies under the sector area in question, this approximation would break down. The distance from the transmitter to the center of the disturbance is denoted R_{oc} and the distance from the center of the disturbance to the receiver is denoted R'_c as shown in Figure 6.3. Another simplifying approximation that we adopt is to assume the ground conductivity under the center point of the disturbance to be equal to the ground conductivity underneath the entire disturbed region. This assumption is required by the WKB approximation used in our model, and is reasonable in view of the results of section 4.3.1 indicating that the scattering caused by a disturbance is insensitive to differences in the conductivity of the Earth surface underneath the disturbed region (except in ice cap regions).

Since the transverse dimensions of disturbance regions studied are larger than a wavelength, the phase of each modal signal can vary significantly across the disturbance region. Thus, a geometrical factor $\mathcal{F}_n(x', y')$ which accounts for the phase difference (and signal attenuation) of each modal field arriving at each infinitesimal area element across the disturbance region (\mathcal{P}) with respect to the modal field phase (and amplitude) arriving at

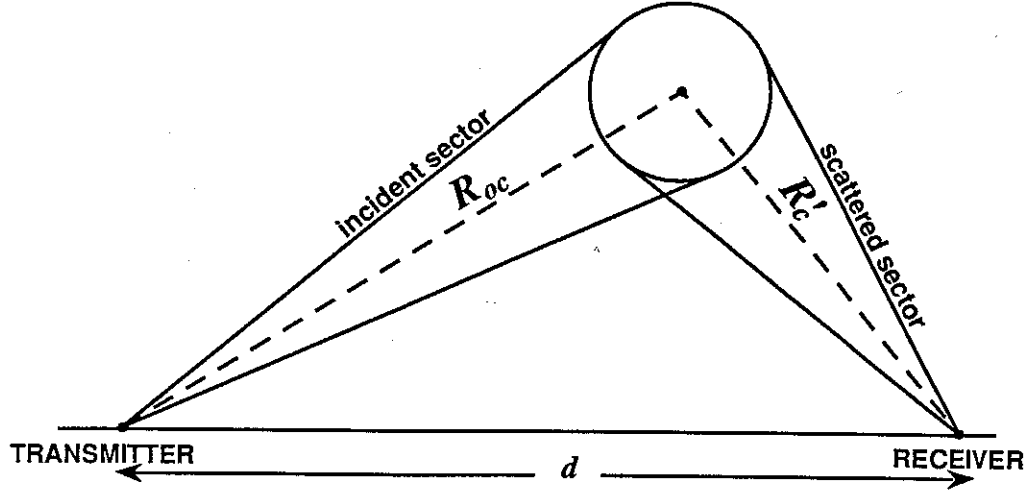


Figure 6.3: The 'incident sector' and 'scattered sector' within which lie all propagation paths from the transmitter to each infinitesimal area element and from each area element to the receiver, respectively.

the center point of the region \mathcal{P} must be included in the integrand. This factor is such that

$$e_n^{LWPC}(R_o)e_n^{LWPC}(R') = \mathcal{F}_n(x', y')e_n^{LWPC}(R_{oc})e_n^{LWPC}(R'_c) \quad (6.10)$$

where R_o and R' , as defined in Chapter 4, are functions of x' and y' , but R_{oc} and R'_c , as defined above, are constants and can be moved outside the double integral. If we substitute Equation 6.5 into Equation 6.10 and solve for $\mathcal{F}_n(x', y')$ we find that

$$\mathcal{F}_n(x', y') = \sqrt{\left| \frac{\sin(R_{oc}/R_E) \sin(R'_c/R_E)}{\sin(R_o/R_E) \sin(R'/R_E)} \right|} e^{-ik_o S_n^o[(R_o+R')-(R_{oc}+R'_c)]} \quad (6.11)$$

where the variables are as previously defined.

Substituting Equation 6.11 in Equation 6.8 we obtain the final formulation that we use to describe the total electric field at the receiver in the general case of multiple mode 3-D scattering method from a disturbance region \mathcal{P} :

$$E_{total} \simeq E^{LWPC}(d) + \sum_n e_n^{LWPC}(R_{oc}) \frac{e_n^{LWPC}(R'_c)}{K A_n^{T,R}} c_n \iint_{\mathcal{P}} [S_n^2(x', y') - (S_n^o)^2] \mathcal{F}_n(x', y') dx' dy' \quad (6.12)$$

where

$E^{LWPC}(d) = \sum_n^\infty e_n^{LWPC}(d)$, which is the electric field that is obtained using the standard LWPC code along the direct transmitter–receiver path in the absence of any disturbances,

$e_n^{LWPC}(R_{oc})$ is the electric field for mode n calculated with the LWPC code along ‘leg 1’ (Figure 6.2) from the transmitter to the center point of the disturbance,

$e_n^{LWPC}(R'_c)/KA_n^{T,R}$ is the electric field, also for mode n , calculated using the LWPC code along ‘leg 2’ from the center point of the disturbance to the receiver, but with the transmitter and receiver antennae height-gain and initial excitation factors removed from the LWPC calculations. ($A_n^{T,R}$ is calculated by LWPC when evaluating $e_n^{LWPC}(R_{oc})$ and only needs to be included once in the transmitter–scatterer–receiver propagation path calculation.) The factor K is a result of the geometrical spreading factor substitution explained in the previous subsection.

The other variables have been previously defined.

The summation in Equation 6.12 is in principle over an infinite number of modes, but beyond a finite number N the modes become negligible in magnitude.

6.2.3 The Methodology

The methodology of our multiple-mode scattering formulation, based on Equation 6.12, can now be summarized as follows where steps 1–6 correspond to the label numbers in Figure 6.2:

1. LWPC is used along the GCP from the transmitter to the receiver to find the total electric field arriving along the ‘direct path’ (E_{direct}).
2. LWPC is used along ‘leg 1’ from the transmitter to the disturbance to find the value of the electric field for each mode n arriving at the center of the disturbance region

- (e_n). This calculation includes the effects of both the transmitter, and the receiver at which the scattered signal will eventually arrive.
3. A factor representing the signal strength scattered by the entire disturbance towards the receiver is calculated for each mode n , one mode at a time.
 4. LWPC is used along 'leg 2' from the center of the disturbed region to the receiver, but renormalized to account for only the propagation effects on each mode in travelling from the disturbance to the receiver. (The usual antenna excitation values for both the transmitter *and* the receiver have already been calculated in step 2.)
 5. The results of steps 2, 3, and 4 are combined to find the total electric field scattered by the disturbance which arrives at the receiver ($E_{scattered}$).
 6. The direct and scattered electric fields are summed to obtain the total perturbed value of the electric field ($E_{total} = E_{direct} + E_{scattered}$).
 7. The total perturbed value of the electric field at the receiver E_{total} is compared to the total ambient electric field at the receiver E_{direct} to calculate the change in amplitude ΔA and change in phase $\Delta\phi$ caused by the disturbance. The latter quantities are directly measured in experimental data when a localized disturbance suddenly appears, for example due to a burst of precipitating energetic electrons.

6.3 Example of the Use of the 3-D Multiple Mode Model

An example of the application of the 3-D methodology (including the effects of ground variation along the propagation paths) is presented in Figures 6.4 and 6.5 for the propagation path between the NSS transmitter (Annapolis, Maryland, $f = 21.4$ kHz) and Stanford University and a particular example of an ionospheric disturbance. The center of the disturbed region for this case was assumed to have the disturbed density profile shown in Figure 6.1, and the density enhancement was assumed to decrease with radial distance from the center and merge back to the ambient density proportional to a gaussian function (as described in section 4.2) to produce a cylindrically symmetric transverse

profile with ~ 100 km effective radius. The center of the disturbance is taken to be 100 km in the transverse direction away from a point 3000 km along the GCP from the NSS transmitter, and on the northerly side of the NSS–Stanford path. Figure 6.4 shows the amplitude and phase plots along the three propagation paths (‘legs’) of Figure 6.2. The signal propagation along ‘leg 1’ and the direct path is similar to those previously discussed in connection with Figure 3.6, and in fact the amplitude variation along ‘leg 1’ is the same as that along the first ~ 1000 km of the direct path. We note that along the scattered path (‘leg 2’), a larger number of modes of comparable amplitude (beginning at the scatterer) result in a complicated amplitude variation that is quite different from that of the final megameter of the direct path. It should also be noted that the amplitude scale for ‘leg 2’ is different than for the other two legs since the field scattered towards the receiver is generally much smaller than the field incident on the disturbance.

Further insight into the propagation along the different path segments and the scattering can be gained upon examination of Figure 6.5. Here we show the relative signal strength and phase for each of the strongest propagating waveguide modes at various points along the three paths of propagation for the specific example described in the previous paragraph. The units of vector length for each phasor diagram are in $\mu\text{V/m}$, assuming a total radiated transmitter power of 1 kW. (We note here that this is simply a normalization for the purpose of discussing relative magnitudes. The typical radiated power levels for operational VLF transmitters are 10 kW to 1 MW and the NSS transmitter nominally radiates ~ 250 kW.) As was noted in the previous paragraph, the phasor diagrams show generally larger amplitudes of higher-order modes being scattered by the disturbance that subsequently propagate along ‘leg 2’. Even at the receiver, there are substantial amounts of these higher-order modes still present. It is interesting, for example, that mode QTE_2 has a larger magnitude than modes QTE_3 or QTE_4 incident on the disturbance (at the end of ‘leg 1’), but that upon scattering, mode QTE_4 has a larger magnitude than either of modes QTE_3 or QTE_2 , with mode QTE_2 now having the smallest magnitude of the three and mode QTE_4 having a magnitude nearly comparable to that of mode QTM_2 (one of the two ‘dominant’ modes). Mode QTE_4 is still the third largest mode of the scattered signal that arrives at the receiver (end of ‘leg 2’), but plays a minor role in the signal that arrives at the receiver along the ‘direct path’. For this

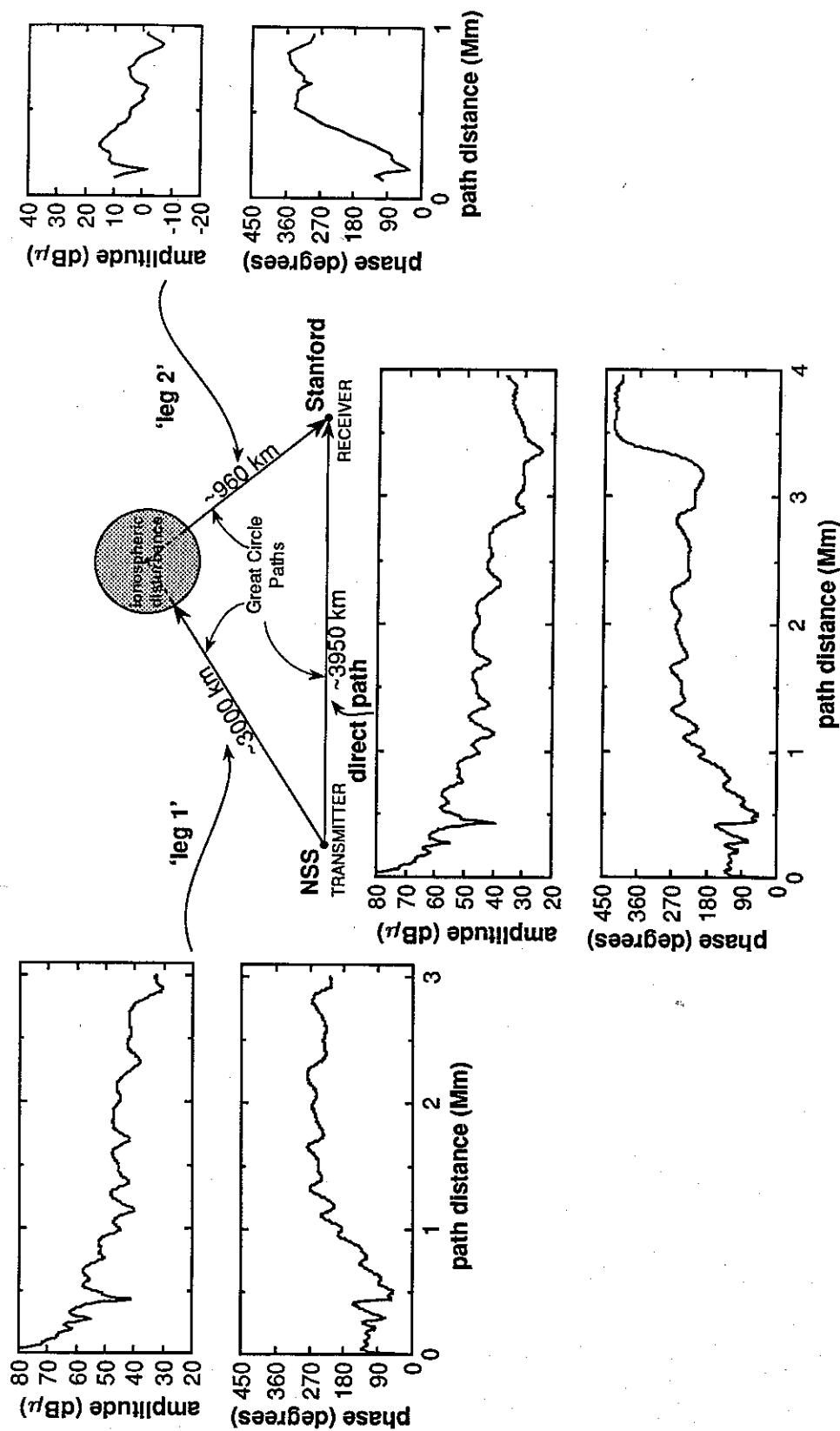


Figure 6.4: Amplitude and phase plots of a signal propagating along the three great circle paths shown for one particular example of a disturbed situation. The effective radius of the disturbance in this case is ~ 100 km and the center of the disturbance is located 3000 km along the great circle path from NSS to Stanford and 100 km away from this 'direct path' on its north side. The lengths of the three paths are given in the center part of the figure (Note: not drawn to scale).

example the calculated change in total received amplitude ΔA of the signal is ~ 0.05 dB, accompanied by a phase change $\Delta\phi$ of ~ 0.6 degrees. These values are in the range of amplitude and phase changes that have been observed on the NSS signal at Stanford during LEP events [Wolf, 1990; Wolf and Inan, 1990].

This procedure (as outlined in the previous subsection) can be employed repeatedly to obtain values for ΔA and $\Delta\phi$ as the location of the disturbance is moved over the region between NSS and Stanford along the GCP, and on both sides of the GCP out to transverse distances where the effect of the disturbance becomes negligible (as discussed in section 4.3.2). Thus, one could obtain a contour map of ΔA and $\Delta\phi$ due to this particular disturbance similar to that shown for the single mode case (Figure 5.2), except that it would show predicted values for an actual path, accounting for the effects of the changing terrain that occurs across mid-North America. Given sufficient computer time, one could produce a “database” of calculated values of ΔA and $\Delta\phi$ for a variety of disturbance sizes and disturbed electron density profiles for every transmitter–receiver path of interest. The database of theoretical values could then be used in conjunction with actual experimental measurements of signal perturbations on those paths to make a first order prediction of the possible locations, sizes, and disturbed electron density profiles of the disturbances believed to have caused those signal perturbations.

6.4 Some Results Obtained with the Multiple Mode Model

In the following sections, the 3-D multiple mode model is used to investigate the physics of VLF wave propagation in the Earth-ionosphere waveguide in the presence of the type of lower ionosphere electron density enhancement disturbances described in the previous chapters. In order to concentrate on the effects on propagation of ionospheric variations and spatial parameters (i.e., distance between transmitter and receiver, location and site of disturbance), we limit the Earth surface parameters (conductivity and relative dielectric constant) to being homogenous over the entire region underlying the propagation paths. Note that the assumption of an electrically homogeneous Earth is made simply for the purpose of clarity and is not necessary for the use of the 3-D model. Indeed, the

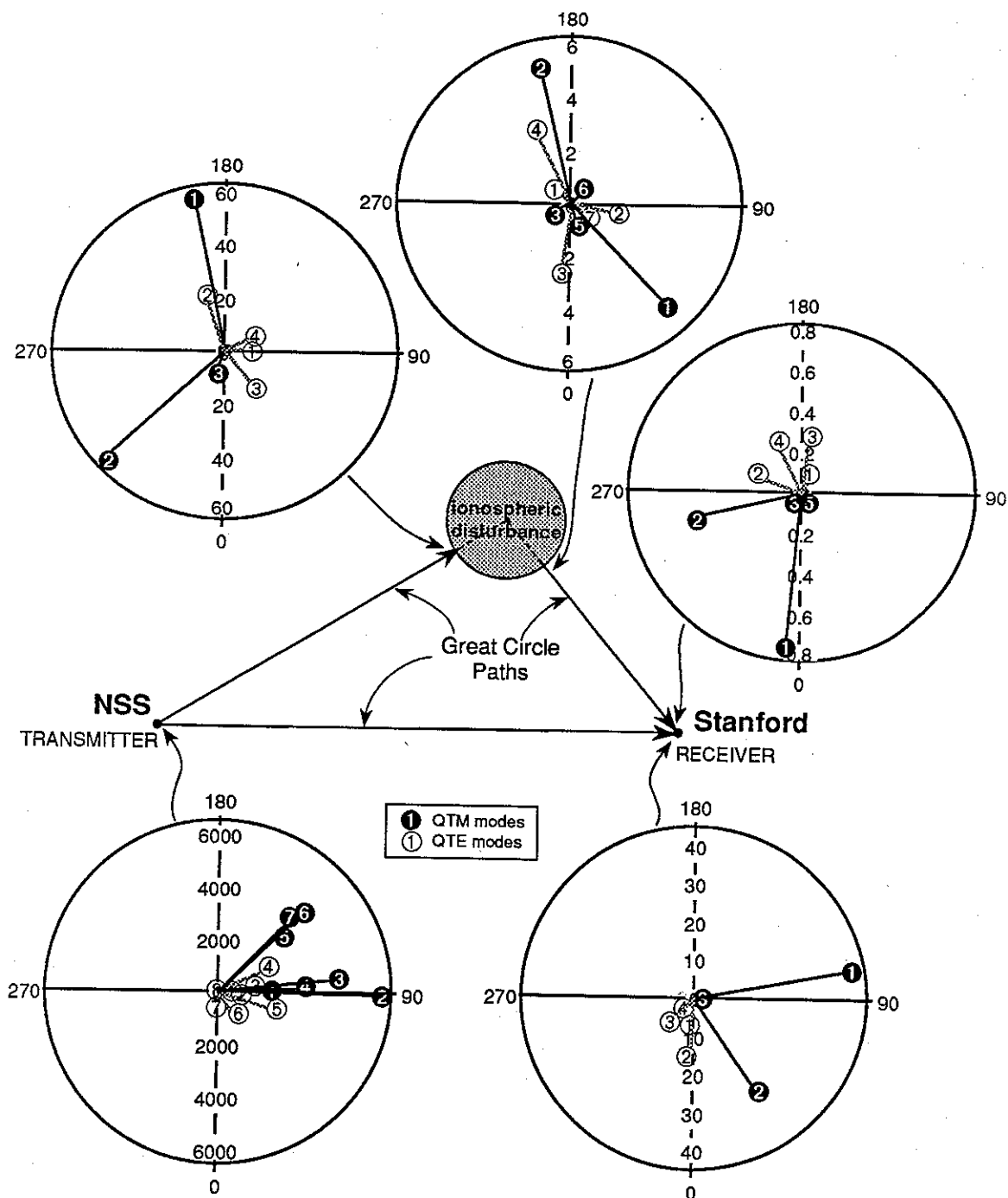


Figure 6.5: Phasor diagrams of the relative signal strength and phase of each mode of the propagating signal located at the points indicated by an arrow along the three propagation paths for the example described in Figure 6.4. The units of vector length indicated in each phasor diagram are in $\mu\text{V/m}$.

NSS-Stanford example discussed in the previous section was based on a realistic Earth conductivity map.

6.4.1 The Effect of Disturbed Density Profile Variation on Received Signal Perturbations

Figure 6.6 shows one set of examples of the effect that differences in the altitude profile of electron density within a disturbance can have on the received signal perturbations caused by that disturbance. The four disturbed density profiles shown in Figure 6.6a are the same as the correspondingly labelled profiles of Figure 4.3, and each was used as the density profile at the center of a disturbance of effective radius $a = 150$ km centered at the midpoint of a 6000 km path with ground conductivity $\sigma = 4$ S/m and $\epsilon_r = 15$ along the entire path. The change in amplitude ΔA and change in phase $\Delta\phi$ of a 25 kHz signal caused by this disturbance were calculated for each of the four disturbed density profiles. The results of these calculations are displayed in Figures 6.6b and c.

We note that some disturbed profiles cause relatively larger changes in amplitude ΔA than other profiles accompanied by relatively smaller changes in phase $\Delta\phi$. This illustrates the sensitive dependence of scattering caused by a disturbance to differences in the vertical electron density profile within the disturbed region. For example, profiles I and II causes a larger ΔA than profile IV, while profile IV causes a larger $\Delta\phi$ than either profile I or II. (The use of the terminology "profile X 'caused' a ΔA " is a shorthand notation to refer to the change in the received signal amplitude ΔA caused by a disturbance of the type described in section 4.2 having a vertical electron density profile at its center given by profile X.) However, we note that profile III causes both the largest ΔA and $\Delta\phi$, even though it represents an electron density enhancement which does not penetrate as deeply into the atmosphere as does that represented by profile IV. An investigation of the amplitude and phase changes produced by these same profiles for different ground conductivities σ and effective disturbance radii a showed that the scattered signal represented by ΔA and $\Delta\phi$ was always largest for a disturbance having the disturbed density profile III. Figure 6.7 shows the resulting ΔA and $\Delta\phi$ for the same conditions as in Figure 6.6 except for the ground parameters which were assumed to be $\sigma = 10^{-3}$

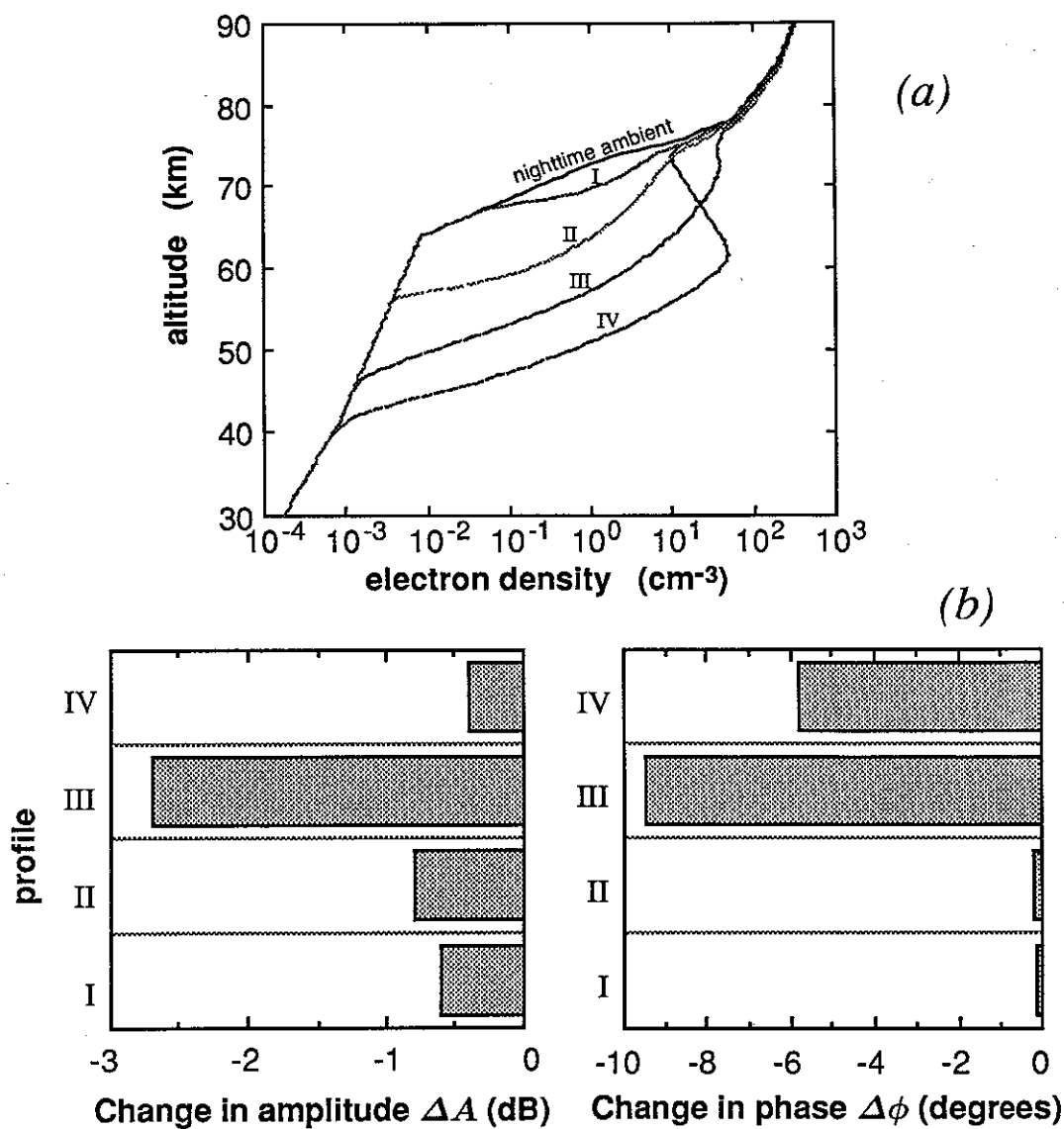


Figure 6.6: (a) Reproduction of four of the five disturbed electron density profiles from Figure 4.3. (b) Change in the received amplitude and phase caused by a lower ionospheric disturbance for each of the four disturbed density profiles shown in Figure 6.6a (for $f = 25$ kHz and a disturbance having effective radius $a = 150$ km centered at the midpoint of a homogeneous 6000 km $\sigma = 4$ S/m Earth surface).

S/m and $\epsilon_r = 15$. While the ΔA for profile IV is larger in magnitude than for profile III, the $\Delta\phi$ for profile III is larger than that for profile IV and calculations indicate that the magnitude of the total signal scattered towards the receiver by a disturbance having disturbed profile III is only 4.3 dB lower than the direct signal, while the magnitude for that having profile IV is 5.9 dB lower than the direct signal. Thus, a disturbance with profile III scatters a stronger signal than do disturbances having profiles I, II, or IV.

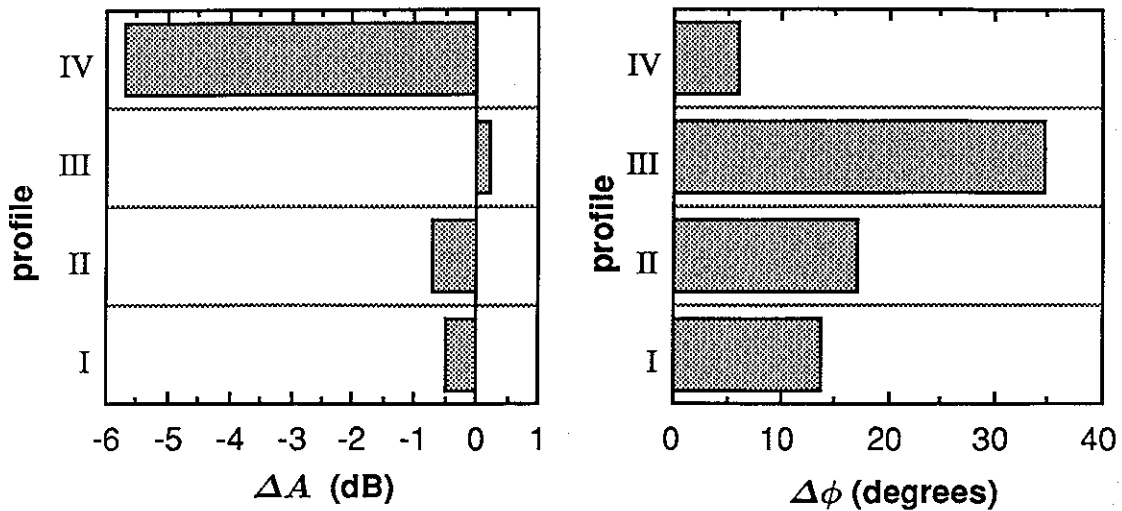


Figure 6.7: Change in the received amplitude and phase caused by a lower ionospheric disturbance versus the four disturbed density profiles shown in Figure 6.6a for the same conditions as in Figure 6.6 except that $\sigma = 10^{-3}$ S/m.

The physical reason for the results of Figures 6.6 and 6.7 become clear upon examination of the eigenangle solutions (as is shown in Figure 6.8 for a 25 kHz signal and $\sigma = 4$ S/m) for two of the profiles of Figure 6.6. We see that most of the mode solutions for profile III are much further away from the corresponding ambient mode solutions than are those for profile IV, particularly for the QTM 'branch' of solution angles. As explained in section 4.3.1, this indicates that most of the modes are scattered more strongly by a disturbance having profile III than by one having profile IV. The separation between the disturbed and ambient mode solutions for profile III are also larger than for profiles I

and II. The same result is found when the corresponding calculations and comparisons are made for frequencies of 15 kHz and 50 kHz.

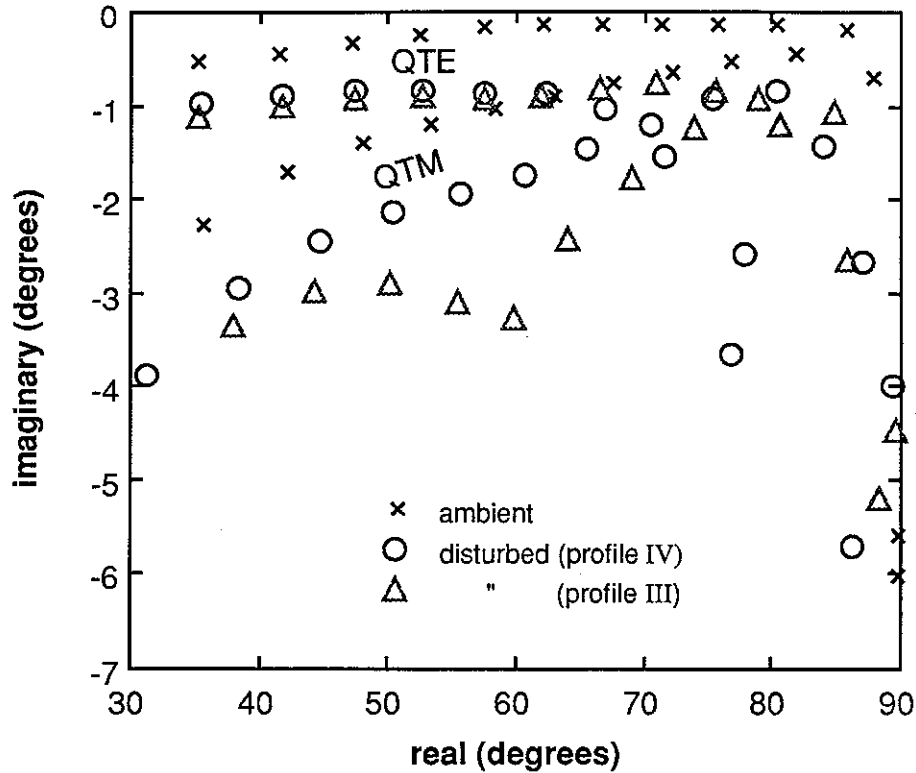


Figure 6.8: Eigenangle solutions for $f = 25$ kHz and $\sigma = 4$ S/m for vertical electron density profiles III and IV of Figure 6.6a.

Further insight can be gained by examining the altitude pattern of the electric field shown in Figure 6.9 for two representative waveguide modes (QTE_7 and QTM_7) for the 25 kHz case for disturbances represented by profiles III and IV. When compared with the ambient electric field patterns for the same modes shown in Figure 2.9, the patterns of Figure 6.9 illustrate the modification of the modal field component structures as a result of the disturbances. In particular, the QTM_7 field components are significantly different from the ambient for both the profile II and IV cases. For example, the e_x component for QTM_7 is larger at all altitudes than the e_y component as compared to the ambient component fields. And in the case of profile III, the QTM_7 field structure undergoes

dramatic change from the ambient field structure. We note in particular that the QTM₇ field structure appears to undergo the greatest change from the ambient structure in the ~ 50–80 km altitude region for profile IV, while the maximum modification with respect to the ambient for the case of profile III is near 70 km in altitude.

To better understand the differences in ΔA and $\Delta\phi$ perturbations resulting from the disturbances represented by profiles I through IV, and in particular, the fact that ΔA and $\Delta\phi$ for profile III are generally larger than those for profile IV, despite the deeper penetration of the electron enhancement for the case of profile IV, we examine the electrical conductivity of the ionosphere as shown in Figure 6.10. At low altitudes where $\nu > \omega_{He}$ (and ω_{He} is the electron gyrofrequency), the ionosphere can be regarded [Budden, 1961] as a medium with dielectric constant

$$\epsilon_{ionosphere} = 1 - \frac{X}{1 + Z^2} \quad (6.13)$$

and conductivity

$$\sigma_{ionosphere} = \frac{\epsilon_0 X \nu_e}{1 + Z^2} \quad (6.14)$$

where

$$X = \frac{N_e e^2}{\epsilon_0 m_e \omega^2} \quad (6.15)$$

$$Z = \frac{\nu_e}{\omega} \quad (6.16)$$

and

ϵ_0 is the permittivity of free space,

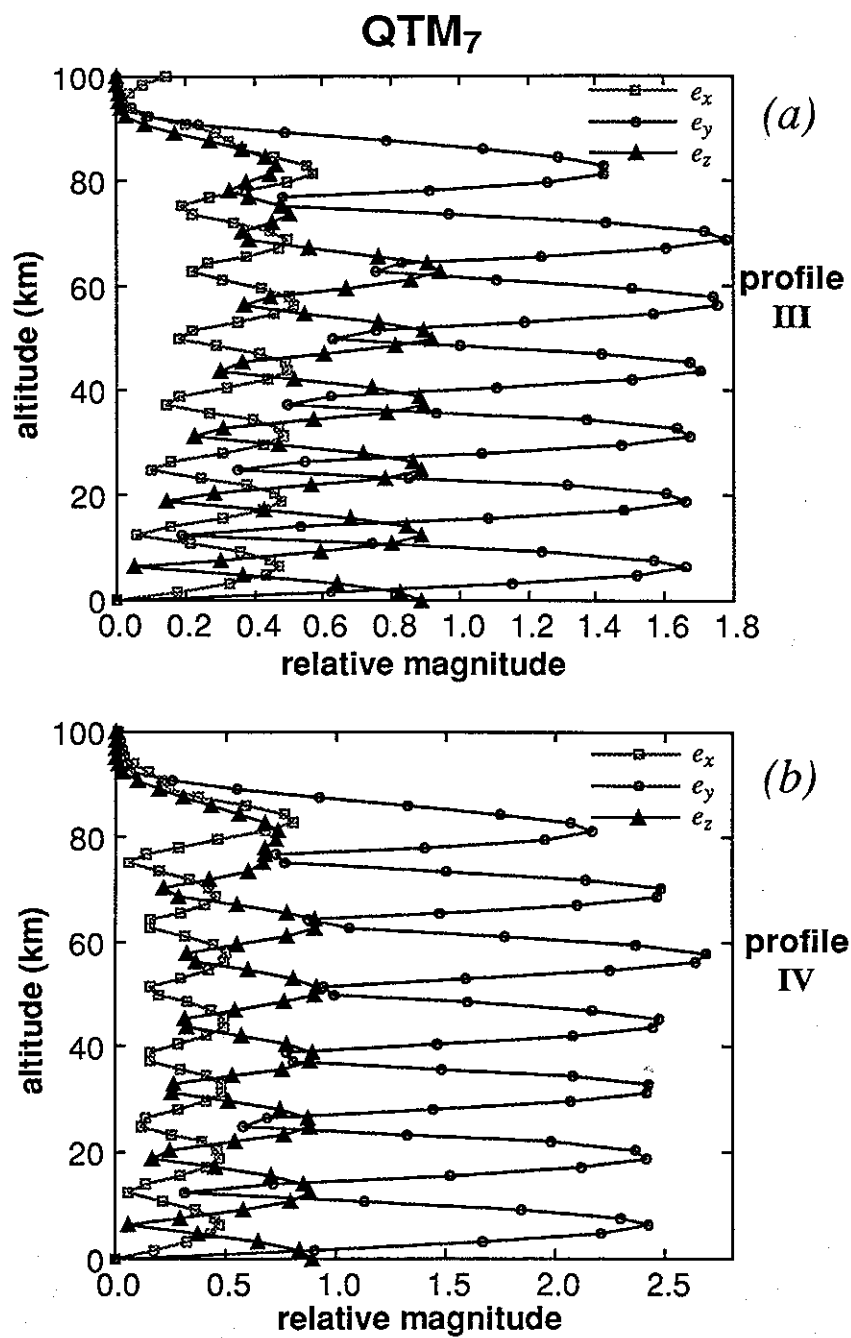
ν_e is the electron-neutral particle collision frequency,

e is the charge of an electron,

N_e is the number of electrons per unit volume,

m_e is the mass of an electron,

and ω is the wave frequency in radians per second.



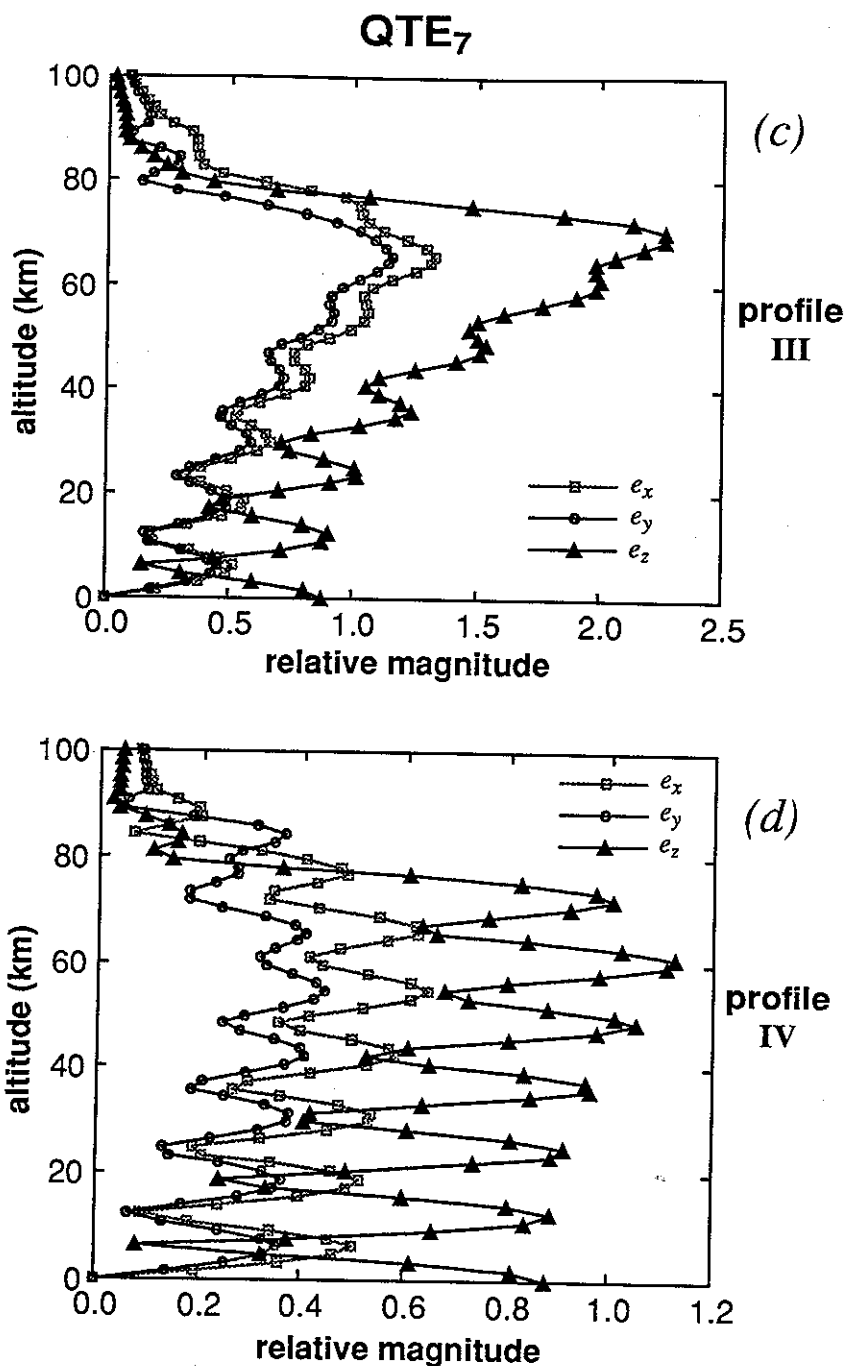


Figure 6.9: Component vertical electric field structure of modes QTM₇ (a) and (b), and QTE₇ (c) and (d) of a 25 kHz signal for $\sigma = 4$ S/m and ionospheric electron density profiles III and IV of Figure 6.6a. See Figure 2.9a and c for field structures for undisturbed ambient ionospheric conditions.

Figure 6.10 shows plots of $\sigma_{ionosphere}$ versus altitude corresponding to the electron density profiles shown in Figure 4.3 for a wave frequency of 25 kHz and for the effective collision frequency profile specified in Chapter 3.

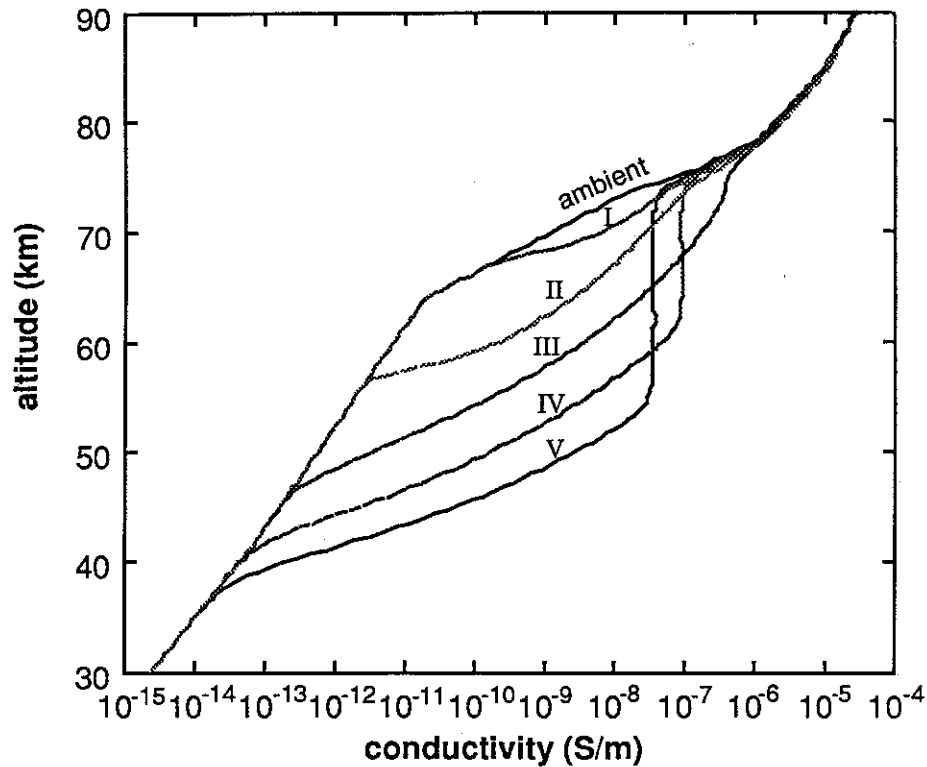


Figure 6.10: Plots of $\sigma_{ionosphere}$ versus altitude corresponding to the density profiles shown in Figure 4.3 for a 25 kHz wave.

We note that the largest increase in conductivity (with respect to the ambient) of any of the profiles occurs for profile III, and lies in the $\sim 68\text{--}75$ km altitude region, which is the same region where we see the greatest change in the field structure of the profile III QTM₇ mode shown in Figure 6.9. The largest increase in conductivity for profile IV occurs in the $\sim 50\text{--}75$ km altitude region, which is the same altitude range where the greatest change in the field structure of the profile IV QTM₇ mode occurs. Thus, it appears that the scattering caused by a given ionospheric disturbance is sensitive to modifications in the altitude profile of the ionospheric ‘conductivity’ within the disturbed region rather

than just to differences in the altitude profile of the electron density. Furthermore, for a given disturbance and for each waveguide mode, larger electrical conductivity changes with respect to the ambient lead to larger scattered field magnitudes.

6.4.2 Dependence of Perturbations in the Received Signal on the Receiver Location

While the results shown in Figures 6.4 and 6.5 are for one particular size and location of the disturbance, the amplitude and phase changes seen at the receiver also depend strongly on the location of the receiver, as well as on the location, size, and makeup of the disturbed region [Tolstoy, 1983; Tolstoy *et al.*, 1986; Poulsen *et al.*, 1990]. This dependence on receiver location was described for the case of a 2-D disturbance in section 3.5. In Figure 3.7*c* and *d* of that chapter, the calculated amplitude and phase of a 21.4 kHz signal propagating from NSS to Stanford was shown for the ambient case, and for the case of a 2-D disturbance located approximately midway along the GCP. Both the amplitude and phase of the signal in the presence of the disturbance changed considerably from the undisturbed ambient values at some location beyond the disturbance, while at other locations little to no change in amplitude and phase occurred. Thus, if the receiver were moved along the GCP beyond the disturbance, the measured change in amplitude and/or phase, ΔA and $\Delta\phi$, would vary from $\Delta A = 0$ dB or $\Delta\phi = 0^\circ$ to $|\Delta A| > 10$ dB or $|\Delta\phi| > 30^\circ$. We obtain analogous results when using the multiple mode 3-D model.

Figure 6.11*a* shows a plot of the calculated amplitude of a 25 kHz signal propagating over a homogeneous, $\sigma = 10^{-3}$ S/m, $\epsilon_r = 15$, ground surface. A cylindrically symmetric (3-D) disturbance with effective radius $a = 50$ km is centered directly over the GCP at a point 3000 km away from the transmitter. The electron density profile at the center of the disturbance was taken to be that of profile III of Figure 6.1. The receiver location is then varied along the GCP from a point just beyond the disturbance out to ~ 6000 km away from the transmitter (or 3000 km away from the center of the disturbance). Figures 6.11*b* and *c* show the changes in amplitude (ΔA) and in phase ($\Delta\phi$) that would be measured at the receiver due to the disturbance as a function of the receiver location. We note that ΔA and $\Delta\phi$ vary in both magnitude and sign as a function of the receiver location along

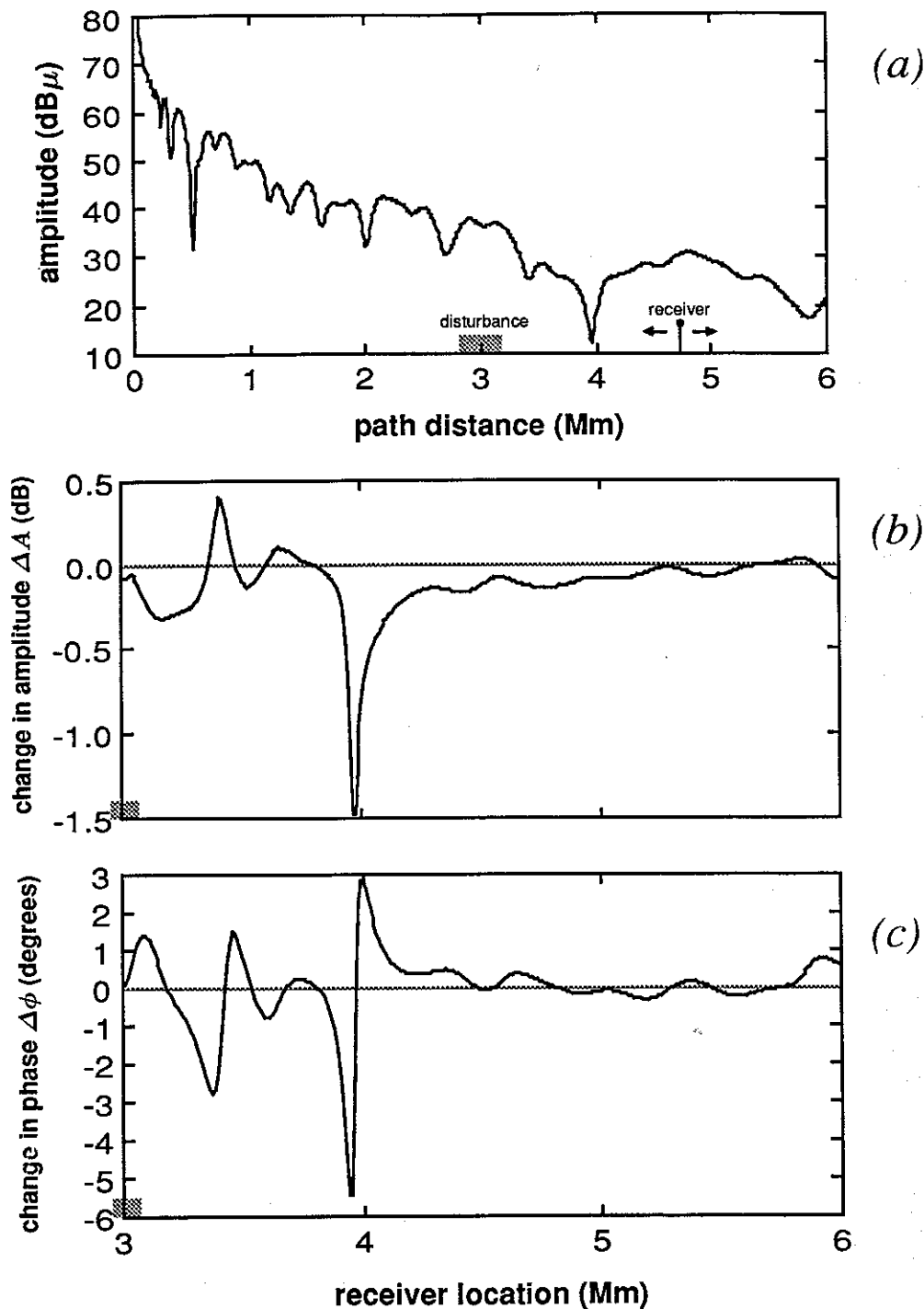


Figure 6.11: (a) Undisturbed electric field strength versus propagation path distance of a 25 kHz signal over a homogeneous $\sigma = 10^{-3}$ S/m surface. (b) Change in the received amplitude of Figure 6.11a versus receiver location due to a 3-D disturbance with effective radius $a = 50$ km centered directly over the GCP at a distance 3000 km away from the transmitter. (c) Change in the received phase corresponding to Figure 6.11b.

the GCP away from the disturbance. An interesting difference from the single mode behavior that is evident from Figures 6.11*b* and *c* is that, although each waveguide mode component suffers a reduction in amplitude and an advance in phase due to disturbances centered on the GCP (i.e., ΔA_n is negative and $\Delta \phi_n$ is positive for each mode n), the total vector sum of the modes may produce overall changes in the received signal amplitude and phase, ΔA and $\Delta \phi$, of both polarities. The largest magnitudes of ΔA and $\Delta \phi$ occur when the receiver is located in the deep null in the ambient signal strength located just before the 4000 km point along the GCP (see Figure 6.11*a*). The reason for this result is the fact that small changes in the mode structure of the wave at this location will produce large changes in the amplitude and phase relative to the small signal level at this point [Tolstoy, 1983; Tolstoy *et al.*, 1986; Barr *et al.*, 1985]. In terms of interpretation of experimental data and the design of new experiments, this result is important since, for a given signal-to-noise environment, the sensitivity to small ionospheric changes is greatly enhanced by locating the receiver near a null in the signal amplitude.

6.4.3 Dependence of the Signal Strength versus Distance Pattern on the “Ambient” Ionospheric Density Profile

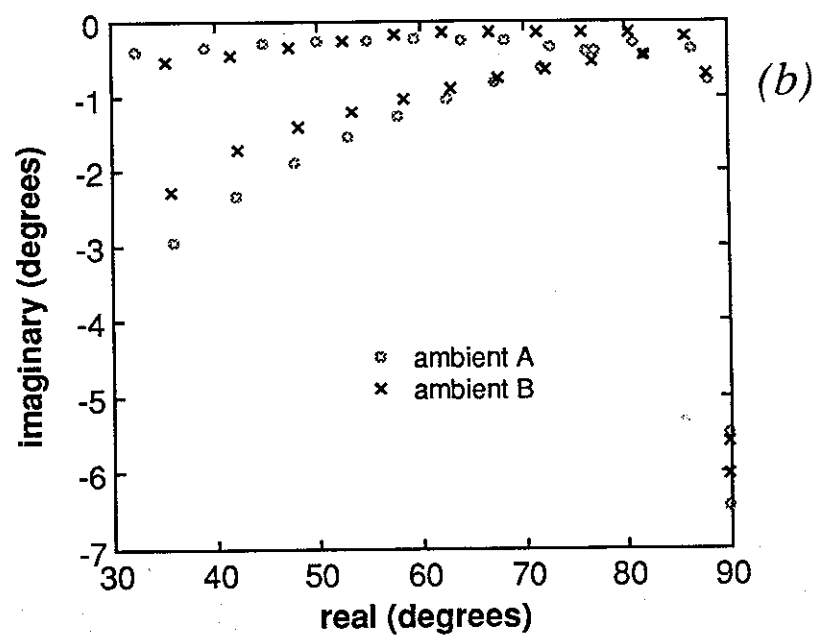
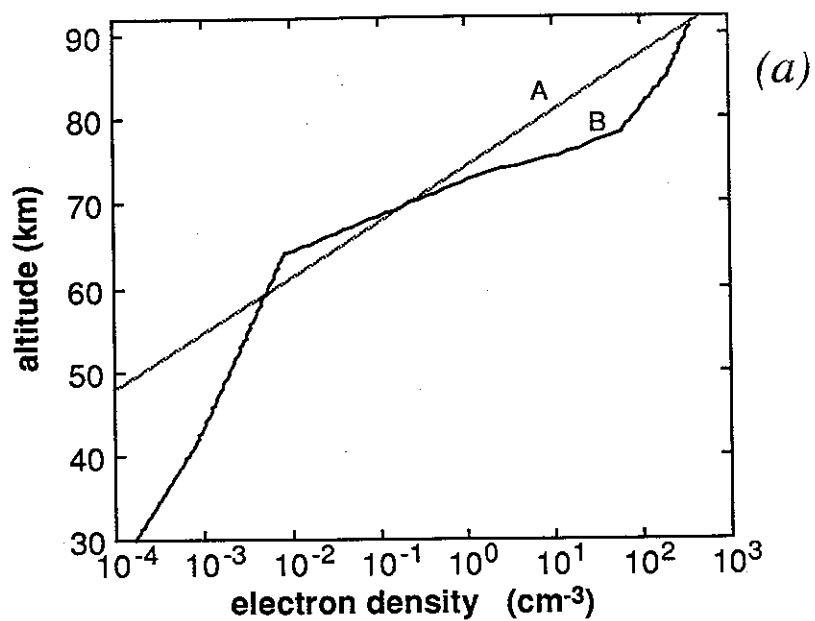
The potential importance of the result described in the previous section raises the question of the dependence of the ambient null locations on the ionospheric conditions. Figure 6.12 shows that differences in the ambient (undisturbed) ionospheric electron density profile significantly affect or alter the undisturbed signal strength versus distance ‘pattern’ and hence the location of the nulls. Figure 6.12*a* shows two different “ambient” lower ionospheric electron density profiles used for purposes of comparison. Profile A is the simple exponential profile given by Equation 3.1 for a nighttime *D* region ionosphere where $\beta = 0.5 \text{ km}^{-1}$ and $h' = 85 \text{ km}$. Profile B is the ambient nighttime profile used for all the example in this dissertation (see Figure 1.3 and section 4.2). Figure 6.12*b* shows a plot of the eigenangle solutions of a 25 kHz wave for both profiles of Figure 6.12*a* and a sea-water ($\sigma = 4 \text{ S/m}$, $\epsilon_r = 81$) Earth surface. We note that almost none of the eigenangle solutions of corresponding modes are identical or even close to one another in the complex plane. Figure 6.12*c* shows the signal strength versus distance corresponding to both sets

of mode solutions shown in Figure 6.12b for homogeneous waveguide conditions. We note that the location, multiplicity, and depth of the nulls in the field strength are quite different for the two ambient ionospheric density profiles. For example, there is a null at a distance of approximately 2200 km from the transmitter for profile A whereas there is a relative maximum in the field strength at the same location for profile B.

The sensitive dependence of the ΔA and $\Delta\phi$ to be received at a fixed location on the ambient ionospheric conditions underscores the need to use a quantitative model, such as that presented here, in interpreting experimental data. In doing so, and in view of the general lack of knowledge of the lower ionospheric ambient density [Forbes, 1989; Ferguson *et al.*, 1989], it is important that careful measurements of the signal under ambient conditions be made and compared with the model predictions to assess the ambient ionospheric profile. Once this is done, amplitude and phase changes due to transient disturbances can be properly interpreted.

Note on the Dominance of a “Dominant” Mode

Again referring to Figure 6.12c, we note that a deep null (an approximately 20 dB drop in signal level) occurs near the 4000 km point (for either of the two cases) even though the signal has propagated a relatively long distance over an all-sea path and in such cases we expect [Inan and Carpenter, 1987] that one, or maybe two, modes are “dominant”. Indeed, in the case shown in Figure 6.12c, the strongest mode at the 4000 km point is the QTM₂ mode while the QTE₂ mode is just ~5 dB smaller in magnitude. Even if these two modes are exactly opposite in phase, their destructive interference would produce a drop in total signal amplitude of only ~7 dB. However, at the 4000 km point there are three other modes, QTM₁, QTM₃, and QTE₃, whose amplitudes are 15, 12, and 12 dB smaller, respectively, than the amplitude of the “dominant” QTM₂ mode. These three modes could, in tandem, combine to destructively interfere with the QTM₂ mode and cause an ~10 dB drop in the total signal amplitude. Thus, these “minor” modes, together with the QTE₂ mode, can (and do) sometimes combine together in phase to “gang up on” the dominant mode to produce a 20 dB drop in total signal level at large propagation distances. Even if there were one “dominant” mode and the next three smaller modes



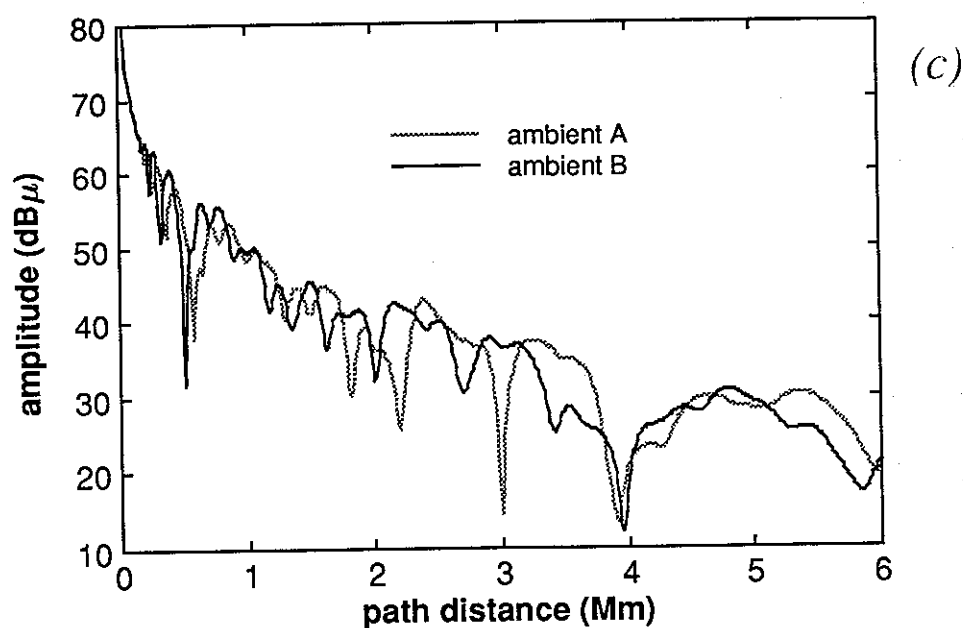


Figure 6.12: (a) Electron density versus altitude for two different “ambient” ionospheres. (b) Eigenangle solutions of a 25 kHz signal for both “ambient” profiles of Figure 6.12a and a sea-water surface. (c) Electric field strength versus distance corresponding to both sets of mode solutions shown in Figure 6.12b for homogeneous waveguide conditions.

were all 10 dB lower in amplitude, if they were in phase with each other and in opposite phase with the dominant mode, they could theoretically cause a 26 dB drop in the total signal level. Thus, care must be taken in deciding if a “dominant” mode is truly dominant at every point—the relative levels of all the other non-negligible modes must be taken into account.

6.5 Conclusions

In summary, a three-dimensional methodology to account for the effect of localized, lower ionosphere electron density disturbances on propagating subionospheric VLF waves has been developed. It utilizes the LWPC software developed by the Naval Ocean Systems Center and the 3-D VLF scattering formulation of *Poulsen et al.* [1990]. Results of the model were found to be in agreement with observations of lightning-induced electron precipitation (LEP) event effects along typical paths. The model is applicable to a wide range of disturbance types in the lower ionosphere that can be modeled by a vertical density profile and that satisfy the WKB and Born approximations. The use of this new model allows the investigation of the physics underlying the connections between the Earth-ionosphere waveguide characteristics and the individual waveguide modes that comprise the propagating wave. The results described here give a better understanding of the physics behind the type of disturbances thought to be created by LEP events as described in Chapter 1.

Chapter 7

Summary & Suggestions for Future Work

7.1 Summary and Contributions

The purpose of this research was to formulate a three-dimensional numerical model of VLF wave propagation in the Earth-ionosphere waveguide in order to study the effect on these waves of transient, localized disturbances in the electron density of the lower ionosphere. The basic motivation for this effort, as described in Chapter 1, is the need to quantitatively interpret a class of transient, localized ionospheric disturbances caused by lightning-induced electron precipitation (LEP) and which lead to characteristic perturbations, often referred to as "Trimpi" events, observed in the amplitude and phase of subionospherically propagating VLF signals. Experimental evidence indicates that the disturbances thought to cause these perturbations are of finite horizontal extent necessitating a 3-D model to interpret their effects rather than the 2-D models used in previous VLF propagation studies. The model formulated in this study uses as its basic components the sophisticated, full-wave, two-dimensional VLF waveguide mode propagation software "LWPC" developed by the Naval Ocean Systems Center (NOSC) [Morfitt and Shellman, 1976; Ferguson and Snyder, 1980; Ferguson *et al.*, 1989] and a perturbation formulation developed by Wait [1961, 1962, 1964*a, b, c*] that gives the modal fields scattered by a localized disturbance in the lower ionosphere in terms of their complex refractive indices within the ambient ionosphere and the disturbed region of the ionosphere. We incorporated as much realism as possible by using typical ranges of values for all

the geophysical parameters that describe the characteristics of both the Earth surface and ionospheric 'boundaries' (both ambient and disturbed) of the Earth-ionosphere waveguide as well as of the VLF wave propagating within this waveguide. Because the LWPC program performs full-wave integrations through the ionosphere in obtaining reflection coefficients for the waveguide boundaries, we were able to model the lower ionosphere realistically as a continuous density distribution of electrons with altitude rather than simply as an abrupt reflection height boundary as has been done in other work [Dowden and Adams, 1990]. We were able to incorporate realistic values for the refractive indices required by the *Wait* formulation using the modal eigenangle solutions provided by the LWPC program.

Although Tolstoy [1983] made an effort to model realistic disturbances in the lower ionosphere using Vondrak-Rees disturbed electron density profiles [Rees, 1963; 1964], her model assumed arbitrarily chosen fluxes of monoenergetic electrons, and because it was a 2-D model, disturbances were incorporated into the model as introduced "slabs" (as described in section 3.5) whose characteristics are abruptly encountered by the wave propagating along the GCP and which are of infinite extent in the direction transverse to the GCP. In our work, we have estimated the altitude profile of ionization within the lightning-induced disturbance based on the energy spectrum of precipitation that would be expected from actual whistler-wave-induced electron scattering at the geomagnetic equator on magnetic field lines (L -shells) in regions where LEP effects are observed (as was described in section 4.2). A number of disturbed electron density profiles expected to be typical for LEP effects over a range of L -shells were then used to investigate the effects of our model disturbances on VLF waves propagating in a model Earth-ionosphere waveguide.

One of the VLF scattering properties of these type of disturbances that was revealed in our analysis was that the magnitude of the scattered modal field is relatively insensitive to differences in the electrical properties of the Earth surface underneath the disturbed region, be it sea-water or soil, except for the case of ice cap or ice shelf regions (as was described in section 4.3.1).

Section 4.3.2 describes another important VLF scattering property of density enhancement disturbances determined by the use of our model. We found that over the range of frequencies, horizontal extent of the disturbances, disturbed density profiles, and Earth surface conductivities considered, the type of disturbance described in section 4.2 scatters most of the wave energy within a fairly small angular range about the forward scatter direction for all non-negligible modes (for disturbances whose effective radius $a \geq 50$ km, the angular pattern is within 50 dB of maximum over the range $\pm 20^\circ$). The angular pattern for all the non-negligible modes for every case studied was found to be very similar, with differences among the modes being only in the overall relative magnitude of the pattern. An important implication of this result is that for typical path lengths, the effects of localized disturbances located at transverse distances $> \sim 200$ km from the propagation path are generally negligible.

The full wave modal eigenangle solutions provided by the LWPC program and the WKB-based scattering formulation of Wait [1964a, b, c] were combined to first formulate a simple, 3-D, single mode propagation model of the effect on the received signal of the type of disturbances described in section 4.2. Results of the single mode model were compared with measurements of Trimpf events on a transmitter-receiver path where single mode analysis may be applicable such as the case of 10–25 kHz waves over a long, all-sea-based path. For example, one such path is the 23.4 kHz NPM signal transmitted from Hawaii and observed at Palmer Station, Antarctica. Chapter 5 describes several interesting results found for the single mode case. One result was that disturbances centered on the GCP itself produce advances in phase (positive $\Delta\phi$) and/or reductions in amplitude (negative ΔA) of the received signal. However, for disturbances located off the GCP, various combinations of positive or negative ΔA and $\Delta\phi$ were found to be possible for the single mode case depending on the disturbance location with respect to the transmitter or receiver, and to the GCP. In accordance with the angular scattered radiation patterns of typical disturbances, as discussed above, single mode analysis showed that the magnitude of the scattered modal field $|e_n^s|$ continuously decreases with distance transverse to the GCP, becoming insignificant (relative to the direct signal) beyond ~ 20 wavelengths. We found that the magnitude of the scattered modal field depends on the magnitude of the difference between the disturbed mode refractive index and the ambient mode refractive

index, and to the horizontal extent of the disturbed region—i.e., all else being equal, disturbances having larger effective radii generally produce larger total perturbations in the received signal.

The single mode analysis also showed that the specific details of the altitude profile of electron density within the disturbance have a significant effect on the magnitude of the perturbed signal seen at the receiver, and particularly on the ratio of amplitude changes to phase changes ($\Delta A/\Delta\phi$) caused by such a disturbance. For example, we found that the disturbed profile produced by a precipitation burst corresponding to a lower L -shell (involving higher energy precipitating electrons and thus enhanced ionization at lower altitudes) produces a higher $|\Delta A/\Delta\phi|$ ratio, than does a profile produced by precipitation corresponding to higher L -shells. This result underscored the fact that it can be physically misleading to model waveguide disturbances in terms of effective reflection height changes rather than by means of the more realistic disturbed electron density profiles whose calculated “effective reflection heights” may be quite similar even if the profiles are not. In comparing our model results with experimental data, we found that the range of ΔA and $\Delta\phi$ values estimated with the single mode model were consistent with LEP events measured on the NPM signal at Palmer Station, Antarctica for typical values of the geophysical parameters that correspond to those of the NPM–Palmer propagation path.

In Chapter 6 we presented a 3-D multiple waveguide mode formulation for modeling the effects of VLF wave scattering caused by localized electron enhancement disturbances in the lower ionosphere on VLF waves propagating on arbitrary transmitter–receiver paths. This formulation takes into account mode conversion among all the non-negligible modes along the three inhomogeneous propagation paths that are involved in a three-dimensional analysis of the problem, and also accounts for all the non-negligible modes that arrive at, and are scattered by, the disturbances. Application of this model to typical disturbances expected for lightning-induced disturbances clearly illustrated that the altitude profile of electron density within the disturbances sensitively affected the received signal perturbations ΔA and $\Delta\phi$. Furthermore, we presented evidence that this sensitivity is due more

to the effect of differences in the ionospheric ‘conductivity’ profile $\sigma_{\text{ionosphere}}(z)$ within the disturbed region than just to differences in the disturbance electron density profile.

Application of the 3-D model also showed the sensitivity of the amplitude and phase changes of a received signal to the location of the receiver (especially with respect to deep nulls in the signal strength along the path) as well as to the location of the disturbance that caused the signal perturbations. A comparison of the significant differences that occur in the calculated signal strength pattern along the propagation path due to two different model “ambient” nighttime electron density profiles showed that a more accurate and complete model of the *D* region electron density is needed in order to more accurately model VLF wave propagation along actual transmitter–receiver paths. Finally, we presented some results of using the complete 3-D multiple mode model to calculate the modal fields of a VLF signal propagating along a typical path, the effects they incur upon encountering a localized disturbance in the lower ionosphere, and the resulting perturbation in the amplitude and phase of the signal seen at the receiver. These were found to be in agreement with observations of LEP event effects seen in signals measured along such paths. Thus, we conclude that this model is very useful for modeling VLF propagation along actual paths in the presence of LEP event disturbances and in investigating the physical nature of such disturbances. Additionally, even though we concentrated on the effects of electron density enhancement disturbances, the model is applicable to other types of waveguide disturbances; i.e., to localized perturbations in other properties of the Earth-ionosphere waveguide, such as localized changes in the ionospheric collision frequencies for example (as occur in radio wave heating of the lower ionosphere by VLF transmitters or lightning discharge radiation [Inan, 1990; Inan *et al.*, 1991]).

7.2 Suggestions for Future Work

As with any search for the solution to a problem, the answer almost always is such that one has more new questions than were answered in the first place, and this research was no different. The suggestions for areas of future work can be divided into two general groups: 1) further uses of the model, and 2) improvements to the model.

7.2.1 Areas of Possible Further Study

Several areas where the model could be used to further investigate the nature of the VLF waveguide disturbance problem suggested themselves over the course of this work. For example, we limited our study to an investigation of the effects on propagating VLF waves of waveguide disturbances consisting of an increase in the electron density in localized regions of the lower ionosphere. It would be interesting to study the effects of localized changes in the various electron and ion collision frequencies on subionospherically propagating VLF signals. Another type of effect suggested for future study would be that of localized, heavy rainfall storms (such as those associated with frontal systems) that move under or near signal propagation paths of interest. Continuous rainfall over an altitude region of several km would, in effect, be a change in the effective conductivity of the Earth surface boundary of the waveguide over a localized region and could be therefore be modeled as a "disturbance" in the the lower waveguide boundary.

Further study of the differences in the effect of disturbances on individual modes is also of interest, particularly for the ~ 50 kHz frequency range where calculations indicate that there are three distinct ranges of significant, non-negligible modes, particularly for short (≤ 1000 km) paths. These are the low order QTM₃/QTE₃ through QTM₆/QTE₆ modes, the "medium order" QTM₁₀/QTE₁₀ through QTM₁₅/QTE₁₅ modes, and the "high order" QTM₂₀/QTE₂₀ through QTM₂₂/QTE₂₂ modes.) A study of this combined with a study of the individual mode behavior of the eigenangle solutions of a disturbed region as its excess electrons recombine and the region returns to the ambient condition would be important in investigating the temporal nature of LEP events as the ionosphere recovers with time. A related area of interest would be to compare the differences between ΔA and $\Delta\phi$ seen on long paths versus that seen on short paths for the same disturbance, again particularly at the higher (~ 50 kHz) frequencies.

Since the behavior of waves in the Earth-ionosphere waveguide is not the same over the entire VLF/LF frequency range, it would be interesting to investigate the differences, if any, in the effects of different disturbed profiles, individual mode behavior, ΔA and $\Delta\phi$ at the receiver, and other characteristics over a larger range of frequencies than was

done in this study (for example, at the following frequencies: 1 kHz, 3 kHz, 10 kHz, 25 kHz, 50 kHz, and 100 kHz).

In order to more clearly understand the nature of the effects of disturbed electron density profiles on a propagating wave, it would be useful to investigate more thoroughly the role that the electron density and collision frequency have on the modal components of the wave at each of a number of small altitude ranges comprising the entire D region.

Finally, in comparing theoretical results with experimental data, it would be useful to know how constant over time (on the order of days, weeks, or months) are some of the lower ionospheric characteristics, such as the ambient electron density, the electron and ion collision frequencies, and the electron flux and energies at a given L -shell that produce the disturbances—particularly for those parameters to which we showed the propagating signal to be most sensitive.

7.2.2 Improvements to the Model

Several improvements that could be made to the model became apparent as this work progressed. One is to incorporate a better model of the Earth surface waveguide boundary than that used in the LWPC model. In particular, a model of the conductivity and relative dielectric constant as a function of depth and of frequency, in some cases, would be most useful in improving the accuracy of modeling actual propagation paths. Also, some way of accounting for the changing altitude of the ground surface, especially in mountainous regions, is important because of possible mode conversion and reflection that occurs in such regions [Thomson, 1985; 1989] and also because many mountain ranges are a significant fraction of a wavelength in height (e.g., Mt. Everest—8.8 km, Cerro Aconcagua—7.0 km, Denali—6.2 km, Kilimanjaro—5.9 km, Vinson Massif—5.1 km, Mont Blanc—4.8 km, Mt. Whitney—4.4 km, Mt. Cook—3.8 km [National Geographic Society, 1990]).

Future work would certainly be expected in the area of extending the model to eventually remove the approximations used, such as the WKB and Born approximations. The

model would then become useful for investigating disturbances for which these approximations break down, such as very small disturbances ($a < \lambda$), more abrupt disturbances than the gaussian shaped ones described in section 4.2, and more intense density enhancements and disturbances of other types where mode conversion would be expected to occur within the disturbed region.

Finally, we suggest the use of a different numerical method such as the moment method (MM) [Stutzman and Thiele, chapter 7, 1981; Kraus, chapter 9, 1988; Richmond, 1965; Harrington, 1968] to calculate the scattering effect of the type of disturbance studied in this work in order to independently check the validity of our approximations and in possibly attaining a more accurate and general model.

Appendix A

A.1 Approximate Analytic Expression for the Scattered Field

According to *Wait* [1964a], the approximate normalized wave field for each mode scattered by a lower ionospheric disturbance of arbitrary horizontal extent can be expressed by the relation (the mode subscript n has been dropped in the following)

$$\frac{e^s}{e^o} = -(i)^{\frac{3}{2}} \frac{k_o \alpha}{\sqrt{\pi}} [S(0, 0) - S^o] I \quad (\text{A.1})$$

where

$$I = \iint_{\mathcal{P}} f(x, y) e^{-i\alpha^2 y^2} dx dy \quad (\text{A.2})$$

$$f(x, y) = \frac{S(x, y) - S^o}{S(0, 0) - S^o} \quad (\text{A.3})$$

$$\alpha = \left[k_o S^o \frac{d}{2x_T x_R} \right]^{\frac{1}{2}} \quad (\text{A.4})$$

and where x and y are defined in Figure 4.1 and the remaining variables are defined in Chapter 4.

If we assume that the ionospheric density perturbation has a cylindrically symmetric Gaussian distribution in the horizontal plane, then according to Equation 4.10 we can express Equation A.3 in the form

$$f(x, y) = e^{-[(x-x_o)^2 + (y-y_o)^2]/a^2} \quad (\text{A.5})$$

where the position (x_o, y_o) represents the point of maximum perturbation. In order to integrate Equation A.2 we will make use of the following identity from *Gradshteyn and Ryzhik* [1965]:

$$\sqrt{\frac{\pi}{q}} = \int_{-\infty}^{\infty} e^{-qp^2} dp \quad (\text{A.6})$$

where the real part of q is positive definite. Substituting Equation A.5 into Equation A.2 and using Equation A.6 we obtain the expression

$$I = a\sqrt{\pi} \int_{-\infty}^{\infty} e^{-(y-y_o)^2/a^2} e^{-i\alpha^2 y^2} dy \quad (\text{A.7})$$

In order to integrate Equation A.7, we first make the change of variable

$$z = y - \frac{y_o}{(1 + i\alpha^2 a^2)} \quad (\text{A.8})$$

With this variable change, Equation A.7 becomes

$$I = a\sqrt{\pi} e^{-i\gamma} \int_{-\infty+i\epsilon}^{\infty+i\epsilon} e^{-(1+i\alpha^2 a^2)z^2/a^2} dz \quad (\text{A.9})$$

where

$$\epsilon = \frac{\alpha^2 a^2 y_o}{1 + \alpha^4 a^4} \quad (\text{A.10})$$

and

$$\gamma = \frac{\alpha^2 y_o^2}{1 + i\alpha^2 a^2} \quad (\text{A.11})$$

Since the integrand in Equation A.9 is analytic everywhere in the finite complex z plane and vanishes at the endpoints, the integration contour can be moved to the real z axis without changing the value of the integral.

In this case, we can again make use of Equation A.6 to evaluate Equation A.9 and obtain

$$I = \frac{a\pi}{\sqrt{1 + i\alpha^2 a^2}} e^{i\gamma} \quad (\text{A.12})$$

Substituting Equation A.12 into Equation A.1, we arrive at the following analytical expression:

$$\frac{e^s}{e^o} = -(i)^{\frac{3}{2}} \sqrt{\pi} \frac{k_o \alpha a^2 [S(0,0) - S^o]}{\sqrt{1 + i\alpha^2 a^2}} e^{-\eta \alpha^2 y_o^2} e^{-i\eta y_o^2/a^2} \quad (\text{A.13})$$

where $\eta = \alpha^2 a^2 / (1 + \alpha^4 a^4)$.

According to Equation A.13 the magnitude of the scattered field has the form:

$$\left| \frac{e^s}{e^o} \right| = \frac{k_o \alpha a^2 |S(0, 0) - S^o|}{(1 + \alpha^4 a^4)^{\frac{1}{4}}} e^{-\eta \alpha^2 y_o^2} \quad (\text{A.14})$$

Thus, the magnitude of the scattered field always decreases exponentially as a function of the distance of the disturbance from the GCP.

The development above can be generalized to the case in which the ionospheric disturbance has an elliptical cross-section for which

$$f(x, y) = e^{-[(x-x_o)^2/a_1^2 + (y-y_o)^2/a^2]} \quad (\text{A.15})$$

If Equation A.15 is used in Equation A.1, the development follows similar lines to yield

$$\frac{e^s}{e^o} = -(i)^{\frac{3}{2}} \sqrt{\pi} \frac{k_o \alpha a_1 a [S(0, 0) - S^o]}{\sqrt{1 + i \alpha^2 a^2}} e^{-\eta \alpha^2 y_o^2} e^{-i \eta y_o^2 / a^2} \quad (\text{A.16})$$

where η is the same as given above. Since the quantity a_1 is a measure of the disturbance length parallel to the GCP, Equation A.16 shows that the strength of the scattered field is linearly proportional to this length. To obtain the results of 2-D theory, let $a \rightarrow \infty$ to produce a disturbance strip of width a_1 along the GCP and which extends to infinity perpendicular to the GCP. For this case:

$$\frac{e^s}{e^o} = -i \sqrt{\pi} k_o a_1 [S(0, 0) - S^o] \quad (\text{A.17})$$

which is identical to Wait's result [1964a] for the 2-D strip disturbance.

Bibliography

- Abramowitz, M., and I. A. Stegun (Eds.), *Handbook of Mathematical Functions*, National Bureau of Standards, Washington, D.C., 1964.
- Adams, C. D. D., Perturbations in subionospheric propagation at VLF, Ph.D. thesis, Univ. of Otago, Dunedin, N. Zealand, 1990.
- Arfken, G., *Mathematical Methods for Physicists*, Academic Press, New York, 1970.
- Barr, R., The propagation of ELF and VLF radio waves beneath an inhomogeneous anisotropic ionosphere, *J. Atmos. Terr. Phys.*, **33**, 343, 1971.
- Barr, R., M. T. Rietveld, H. Kopka, and P. Stubbe, Effect of a heated patch of auroral ionosphere on VLF-radio wave propagation, *Nature*, **309**, 534, 1984.
- Barr, R., M. T. Rietveld, P. Stubbe, and H. Kopka, The diffraction of VLF radio waves by a patch of ionosphere illuminated by a powerful HF transmitter, *J. Geophys. Res.*, **90**, 2861, 1985.
- Barrington, R. E., E. V. Thane, and B. Bjelland, Diurnal and seasonal variations in D-region electron densities derived from observations of cross modulation, *Can. J. Phys.*, **41**, 271, 1963.
- Belrose, J. S., and M. J. Burke, Study of the lower ionosphere using partial reflection, *J. Geophys. Res.*, **69**, 2799, 1964.
- Beyer, W. H., (Ed.), *CRC Standard Mathematical Tables*, CRC Press, Boca Raton, 1981.
- Bohren, C. F., and D. R. Huffman, *Absorption and Scattering of Light by Small Particles*, John Wiley & Sons, New York, 1983.

- Born, M., and E. Wolf, *Principles of Optics*, Pergamon Press, New York, 1965.
- Brace, L. H., and R. F. Theis, The behavior of the plasmapause at mid-latitudes: ISIS-1 Langmuir probe measurements, *J. Geophys. Res.*, 79, 1871, 1974.
- Budden, K. G., The numerical solution of differential equations governing reflexion of long radio waves from the ionosphere, *Proc. R. Soc. London, Ser. A*, 227, 516, 1955.
- Budden, K. G., *Radio Waves in the Ionosphere*, Cambridge University Press, Cambridge, 1961.
- Budden, K. G., *The Wave-guide Mode Theory of Wave Propagation*, Prentice-Hall, Englewood Cliffs, N.J., 1961.
- Budden, K. G., *The Propagation of Radio Waves*, Cambridge University Press, Cambridge, 1985.
- Burgess, W. C., and U. S. Inan, Simultaneous disturbance of conjugate ionospheric regions in association with individual lightning flashes, *Geophys. Res. Lett.*, 17, 259, 1990.
- Carpenter, D. L., and J. W. LaBelle, A study of whistlers correlated with bursts of electron precipitation near $L = 2$, *J. Geophys. Res.*, 87, 4427, 1982.
- Carpenter, D. L., and U. S. Inan, Seasonal, latitudinal and diurnal distributions of whistler-induced precipitation events, *J. Geophys. Res.*, 92, 3429, 1987.
- Carpenter, D. L., U. S. Inan, M. L. Trimpi, R. A. Helliwell, and J. P. Katsufakis, Perturbations of subionospheric LF and MF signals due to whistler-induced electron precipitation bursts, *J. Geophys. Res.*, 89, 9857, 1984.
- Carpenter, D. L., U. S. Inan, E. W. Paschal, and A. J. Smith, A new VLF method for studying burst precipitation near the plasmapause, *J. Geophys. Res.*, 90, 4383, 1985.

- Chang, H. C., and U. S. Inan, Lightning induced energetic electron precipitation from the magnetosphere, *J. Geophys. Res.*, 90, 1531, 1985.
- Chilton, C. J., J. P. Conner, and F. K. Steele, A comparison between solar x-ray emission and VLF sudden phase anomalies, *Proc. of the IEEE*, 53, 2018, 1965.
- Crombie, D. D., The effects of a small local change in phase velocity on the propagation of a VLF radio signal, *J. Res. Natl. Bur. Sect. D*, 68D, 709, 1964.
- Cotton, P. D., A study of Antarctic subionospheric VLF propagation at frequencies below 10 kHz, Ph.D. thesis, Univ. of Sheffield, Sheffield, U. K., 1989.
- Davies, K., *Ionospheric Radio Propagation*, Dover Publications, New York, 1966.
- Dawson, J., and C. Oberman, Oscillations of a finite cold plasma in a strong magnetic field, *Physics of Fluids*, 2, No. 2, 103, 1959.
- Dingle, B., Burst precipitation of energetic electrons from the magnetosphere, Ph.D. dissertation, Stanford Univ., Stanford, Calif., 1977.
- Dowden, R. L., and C. D. D. Adams, Phase and amplitude perturbations on subionospheric signals explained in terms of echoes from lightning-induced electron precipitation ionization patches, *J. Geophys. Res.*, 93, 11543, 1988.
- Dowden, R. L., and C. D. D. Adams, Phase and amplitude perturbations on the NWC signal at Dunedin from lightning-induced electron precipitation, *J. Geophys. Res.*, 94, 497, 1989a.
- Dowden, R. L., and C. D. D. Adams, Modal effects on amplitude perturbations on subionospheric signals (trimpis) deduced from two-frequency measurements, *J. Geophys. Res.*, 94, 1515, 1989b.
- Dowden, R. L., and C. D. D. Adams, Location of lightning-induced electron precipitation from measurement of VLF phase and amplitude perturbations on spaced antennas and on two frequencies, *J. Geophys. Res.*, 95, 4135, 1990.

- Ferguson, J. A., Ionospheric profiles for prediction nighttime VLF/LF propagation, *Tech. Rep. 530*, Naval Ocean Systems Center, San Diego, Calif., 1980.
- Ferguson, J. A., and L. R. Hitney, WAVFLD: A program to compute ionospheric height gain functions and field strengths at VLF, *Tech. Doc. 1192*, Naval Ocean Systems Center, San Diego, Calif., 1987.
- Ferguson, J. A., and F. P. Snyder, Approximate VLF/LF waveguide mode conversion model, *Tech. Doc. 400*, Naval Ocean Systems Center, San Diego, Calif., 1980.
- Ferguson, J. A., and F. P. Snyder, The segmented waveguide program for long wavelength propagation calculations, *Tech. Doc. 1071*, Naval Ocean Systems Center, San Diego, Calif., 1987.
- Ferguson, J. A., L. R. Hitney, and C. H. Shellman, Algorithm for search area definition in MODESRCH, *Tech. Note 1416*, Naval Ocean Systems Center, San Diego, Calif., 1985.
- Ferguson, J. A., F. P. Snyder, D. G. Morfitt, and C. H. Shellman, Long-wave propagation capability and documentation, *Tech. Doc. 1518*, Naval Ocean Systems Center, San Diego, Calif., 1989.
- Field, E. C., Jr., The ion mass and ion-neutral collision frequency in long wave propagation calculations, *Tech. Rep. 1977*, Defense Nuclear Agency, Alexandria, Virginia, 1990.
- Field, E. C., and R. D. Engel, The detection of daytime nuclear bursts below 150 km by prompt VLF phase anomalies, *Proc. of the IEEE*, 53, 2009, 1965.
- Forbes, J. M., The lower thermosphere coupling study of CEDAR and WITS programs, an attempt to better understand the "ignorosphere", *Eos*, 70, 905, 1989.
- Galejs, J., Propagation of ELF and VLF waves below a generally anisotropic ionosphere, *Radio Sci.*, 3, 781, 1968.

- Galejs, J., VLF propagation across discontinuous daytime to nighttime transitions in anisotropic terrestrial waveguide, *IEEE Trans. Ant. Prop.*, AP-19, 756, 1971.
- Galejs, *Terrestrial Propagation of Long Electromagnetic Waves*, Pergamon Press, Oxford, 1972.
- Gradshteyn, I. S., and I. M. Ryzhik, *Table of Integrals, Series, and Products*, Academic, San Diego, Calif., 1965.
- Harrington, R. F., *Field Computation by Moment Methods*, Macmillan, New York, 1968.
- Hauser, J. P., W. E. Garner, and F. J. Rhoads, A VLF effective ground conductivity map of Canada and Greenland with revisions derived from propagation data, *NRL Report 6893*, March 1969.
- Hayakawa, M., and S. Shimakura, On the mechanism of reflection of ELF-LF radio waves from the lower ionosphere, *Trans. of the IECE of Japan*, E61, No. 1, 15, 1978.
- Helliwell, R. A., *Whistlers and Related Ionospheric Phenomena*, Stanford University Press, Stanford, Calif., 1965.
- Helliwell, R. A., and J. P. Katsufakis, VLF wave injection into the magnetosphere from Siple Station, Antarctica, *J. Geophys. Res.*, 79, 2511, 1974.
- Helliwell, R. A., J. P. Katsufakis, and M. L. Trimpi, Whistler-induced amplitude perturbation in VLF propagation, *J. Geophys. Res.*, 78, 4679, 1973.
- Hilton, H. H., *L* parameter, A new approximation, *J. Geophys. Res.*, 76, 6952, 1971.
- Hurren, P. J., A. J. Smith, D. L. Carpenter, and U. S. Inan, Burst precipitation induced perturbations on multiple VLF propagation paths in Antarctica, *Ann. Geophys.*, 4, 311, 1986.
- Inan, U. S., VLF heating of the lower ionosphere, *Geophys. Res. Lett.*, 17, 729, 1990.

- Inan, U. S., and D. L. Carpenter, On the correlation of whistlers and associated subionospheric VLF/LF perturbations, *J. Geophys. Res.*, 91, 3106, 1986.
- Inan, U. S., and D. L. Carpenter, Lightning-induced electron precipitation events observed at $L \sim 2.4$ as phase and amplitude perturbations on subionospheric VLF signals, *J. Geophys. Res.*, 92, 3293, 1987.
- Inan, U. S., H. C. Chang, and R. A. Helliwell, Electron precipitation zones around major ground-based VLF signal sources, *J. Geophys. Res.*, 89, 2891, 1984.
- Inan, U. S., D. L. Carpenter, R. A. Helliwell, and J. P. Katsufakis, Subionospheric VLF/LF phase perturbations produced by lightning-whistler induced particle precipitation, *J. Geophys. Res.*, 90, 7457, 1985.
- Inan, U. S., W. C. Burgess, T. G. Wolf, D. C. Shafer, and R. E. Orville, Lightning-associated precipitation of MeV electrons from the inner radiation belt, *Geophys. Res. Lett.*, 15, 172, 1988a.
- Inan, U. S., T. G. Wolf, and D. L. Carpenter, Geographic distribution of lightning-induced electron precipitation observed as VLF/LF perturbation events, *J. Geophys. Res.*, 93, 9841, 1988b.
- Inan, U. S., D. C. Shafer, W. Y. Yip, and R. E. Orville, Subionospheric VLF signatures of nighttime D region perturbations in the vicinity of lightning discharges, *J. Geophys. Res.*, 93, 11455, 1988c.
- Inan, U. S., F. A. Knifsend, and J. Oh, Subionospheric VLF "imaging" of lightning-induced electron precipitation from the magnetosphere, *J. Geophys. Res.*, 95, 17217, 1990.
- Inan, U. S., T. F. Bell, and J. V. Rodriguez, Heating and ionization of the lower ionosphere by lightning, *Geophys. Res. Lett.*, 18, 705, 1991.
- Jean, A. G., and D. D. Crombie, Detection of high altitude nuclear detonations using the VLF phase shift technique, *IEEE Trans. on Nucl. Sci.*, 242, 1963.

- Kelley, M. C., and R. A. Heelis, *The Earth's Ionosphere: Plasma Physics and Electrodynamics*, Academic Press, San Diego, Calif., 1989.
- Kikuchi, T., and D. S. Evans, Quantitative study of substorm associated VLF phase anomalies and precipitating electrons on November 13, 1979, *J. Geophys. Res.*, 88, 871, 1983.
- Kraus, J. D., *Antennas*, McGraw-Hill, New York, 1988.
- Lohrey, B., and A. B. Kaiser, Whistler-induced anomalies in VLF propagation, *J. Geophys. Res.*, 84, 5121, 1979.
- Maxwell, J. C., *A Treatise on Electricity and Magnetism*, Vols. I and II, Oxford, 1873.
- McIlwain, C. E., Magnetic coordinates, *Space Sci. Rev.*, 5, 585, 1966.
- Morfitt, D. G., Effective electron density distributions describing VLF/LF propagation data, *Tech. Doc. 141*, Naval Ocean Systems Center, San Diego, Calif., 1977.
- Morfitt, D. G., and V. E. Hildebrand, Concepts for the use of multimode propagation theory in VLF coverage predictions, *Tech. Publ. 4983*, Naval Weapons Center, China Lake, Calif., 1970.
- Morfitt, D. G., and C. H. Shellman, 'MODESRCH', an improved computer program for obtaining ELF/VLF/LF mode constants in an Earth-ionosphere waveguide, *Interim Rep. 77T*, Naval Electronics Laboratory Center, San Diego, Calif., 1976.
- National Geographic Society (U.S.), Cartographic Division, *National Geographic Atlas of the World*, 6th ed., National Geographic Society, Washington, D.C., 1990.
- Nielsen, E. D., Scattering by a cylindrical post of complex permittivity in a waveguide, *IEEE Trans. Microwave Theory and Technique*, MTT-17, No. 3, 148, 1969.
- Orville, R. E., R. W. Henderson, and L. F. Besalt, An east coast lightning detection network, *Bulletin of Amer. Meteor. Soc.*, 64, 1029, 1983.

- Orville, R. E., R. A. Weisman, R. B. Pyle, R. W. Henderson, and R. E. Orville, Jr., Cloud-to-ground lightning flash characteristics from June 1984 through May 1985, *J. Geophys. Res.*, 92, 5640, 1987.
- Pappert, R. A., J. A. Ferguson, VLF/LF mode conversion model calculations for air to air transmission in the Earth-ionosphere waveguide, *Radio Sci.*, 21,, 551, 1986.
- Pappert, R. A., and L. R. Hitney, A program to compute ELF/VLF Earth-ionosphere modal height gains via WKB methods up to satellite altitudes, *Tech. Rep. 724*, Naval Ocean Systems Center, San Diego, Calif., 1981.
- Pappert, R. A., and L. R. Hitney, Direction-of-arrival calculations at VLF/LF, *Tech. Doc. 1602*, Naval Ocean Systems Center, San Diego, Calif., 1989.
- Pappert, R. A., and D. G. Morfitt, Theoretical and experimental sunrise mode conversion results at VLF, *Radio Sci.*, 10, 537, 1975.
- Pappert, R. A., and L. R. Shockey, WKB mode summing program for VLF/ELF antennas of arbitrary length, shape and elevation, *Interim Rep. 713*, Naval Electronics Laboratory Center, San Diego, Calif., 1971.
- Pappert, R. A., and L. R. Shockey, Mode conversion program for an inhomogeneous anisotropic ionosphere, *Interim Rep. 722*, Naval Electronics Laboratory Center, San Diego, Calif., 1972.
- Pappert, R. A., and R. R. Smith, Orthogonality of height-gains in the earth-ionosphere waveguide, *Radio Sci.*, 7, 275, 1972.
- Pappert, R. A., and F. P. Snyder, Some results of a mode-conversion program for VLF, *Radio Sci.*, 7, 913, 1972.
- Pappert, R. A., E. E. Gossard, and I. J. Rothmuller, A numerical investigation of classical approximations used in VLF propagation, *Radio Sci.*, 2, 387, 1967.
- Park, and D. L. Carpenter, Very low frequency radio waves in the magnetosphere, Paper 4 in *Upper Atmosphere Research in Antarctica*, *Antarctic Research Series Vol. 29*,

- L. J. Lanzerotti and C. G. Park (Eds.), American Geophysical Union, Washington, D.C., 1978.
- Park, C. G., D. L. Carpenter, and D. B. Wiggin, Electron density in the plasmasphere: whistler data on solar cycle, annual, diurnal variations, *J. Geophys. Res.*, 83, 3137, 1978.
- Parrot, M., World map of ELF/VLF emissions as observed by a low-orbiting satellite, *Annales Geophysicae*, 8, 135, 1990.
- Potemra, T. A., and T. J. Rosenberg, VLF propagation disturbance and electron precipitation at mid-latitudes, *J. Geophys. Res.*, 78, 1572, 1973.
- Poulsen, W. L., T. F. Bell, and U. S. Inan, Three-dimensional modeling of subionospheric VLF propagation in the presence of localized *D* region perturbations associated with lightning, *J. Geophys. Res.*, 95, 2355, 1990a.
- Poulsen, W. L., T. F. Bell, and U. S. Inan, 3-D modeling of subionospheric VLF propagation in the presence of localized D-region perturbations associated with lightning, *The Effects of the Ionosphere on Radiowave Signals and System Performance*, Proc. of Ionospheric Effects Symposium '90, 515, 1990b.
- Raghuram, R., R. L. Smith, and T. F. Bell, VLF Antarctic antenna: Impedance and efficiency, *IEEE Trans. Ant & Prop.*, AP-22, 334, 1974.
- Ramo, S., J. R. Whinnery, and T. Van Duzer, *Fields and Waves in Communication Electronics*, John Wiley & Sons, New York, 1984.
- Ratcliffe, J. A., *The Magneto-Ionic Theory and its Application to the Ionosphere*, Cambridge University Press, Cambridge, 1959.
- Ratcliffe, J. A., *An Introduction to the Ionosphere and Magnetosphere*, Cambridge University Press, Cambridge, 1972.
- Rawer, K., D. Bilitza, and S. Ramakrishnan, Goals and status of the International Reference Ionosphere, *Rev. Geophys.*, 16, 177, 1978.

- Reagan, J. B., R. E. Meyerott, R. C. Gunton, W. L. Imhof, E. E. Gaines, and T. R. Larsen, Modeling of the ambient and disturbed ionospheric media pertinent to ELF/VLF propagation, *Proc. of NATO-AGARD meeting on medium, long, and very long wave propagation*, Brussels, Belgium, September 1981.
- Rees, M. H., Auroral ionization by incident energetic electrons, *Planet. Sp. Sci.*, 11, 1209, 1963.
- Rees, M. H., Note on the penetration of energetic electrons into the Earth's atmosphere, *Planet. Sp. Sci.*, 12, 722, 1964.
- Rees, M. H., Auroral electrons, *Space Sci. Rev.*, 10, 413, 1969.
- Richmond, J. H., Digital computer solutions of the rigorous equations for scattering problems, *Proc. of the IEEE*, 53, 1965.
- Rishbeth, H., and O. K. Garriott, *Introduction to Ionospheric Physics*, Academic Press, New York, 1969.
- Sheddy, C. H., A general analytic solution for reflection from a sharply bounded anisotropic ionosphere, *Radio Sci.*, 3, 792, 1968.
- Shellman, C. H., A new version of MODESRCH using interpolated values of the magnetoionic reflection coefficients, *Tech. Rep. 1143*, Naval Ocean Systems Center, San Diego, Calif., 1986.
- Smith, R. A., Approximate mode conversion coefficients in the earth-ionosphere waveguide for VLF propagation below an anisotropic ionosphere, *J. Atmos. Terr. Phys.*, 36, 1683, 1974.
- Snyder, F. P., and R. A. Pappert, A parametric study of VLF modes below anisotropic ionospheres, *Radio Sci.*, 4, 213, 1969.
- Stutzman, W. L. and G. A. Thiele, *Antenna Theory and Design*, John Wiley & Sons, New York, 1981.

- Svennesson, J., and S. Westerlund, Stellar x-ray effects on VLF radio-wave propagation, *J. Atmos. Terr. Phys.*, 41, 361, 1979.
- Svennesson, J., F. Reder, and J. Crouchley, Effect of x-ray stars on VLF signal phase, *J. Atmos. Terr. Phys.*, 34, 49, 1972.
- Thomson, N. R., Reflection of VLF radio waves from distant mountain ranges, *J. Atmos. Terr. Phys.*, 47, 353, 1985.
- Thomson, N. R., Re-radiation of VLF waves from mountain ranges, *J. Atmos. Terr. Phys.*, 51, 339, 1989.
- Tolstoy, A., The influence of localized precipitation-induced *D* region ionization enhancements on subionospheric VLF propagation, Ph.D. dissertation, Univ. of Maryland, College Park, 1983.
- Tolstoy, A., and T. J. Rosenberg, A quasi three-dimensional propagation model for subionospherically propagating VLF radio waves, *Radio Sci.*, 20, 535, 1985.
- Tolstoy, A., T. J. Rosenberg, and D. L. Carpenter, The influence of localized precipitation-induced *D*-region ionization enhancements on subionospheric VLF propagation, *Geophys. Res. Lett.*, 9, 563, 1982.
- Tolstoy, A., T. J. Rosenberg, U. S. Inan, and D. L. Carpenter, Model predictions of subionospheric VLF signal perturbations resulting from localized, electron precipitation-induced ionization enhancement regions, *J. Geophys. Res.*, 91, 13473, 1986.
- Voss, H. D., W. L. Imhof, M. Walt, J. Mobilia, E. E. Gaines, J. B. Reagan, U. S. Inan, R. A. Helliwell, D. L. Carpenter, J. P. Katsufakis, and H. C. Chang, Lightning-induced electron precipitation, *Nature*, 312, 740, 1984.
- Wait, J. R., Expected influence of a localized change of ionosphere height on VLF propagation, *J. Geophys. Res.*, 66, 3119, 1961.
- Wait, J. R., An analysis of VLF mode propagation for a variable ionosphere height, *J. Res. Natl. Bur. Stand., Sect. D*, 66, 453, 1962.

- Wait, J. R., Calculated diffraction effects at VLF from a localized ionospheric depression, *Tech. Note 208*, National Bureau of Standards, Boulder, Colo., 1964a.
- Wait, J. R., On phase changes in very-low-frequency propagation induced by an ionospheric depression of finite extent, *J. Geophys. Res.*, 69, 441, 1964b.
- Wait, J. R., Influence of a circular ionospheric depression on VLF propagation, *J. Res. Natl. Bur. Stand., Sect. D*, 68, 907, 1964c.
- Wait, J. R., Mode conversion and refraction effects in the Earth-ionosphere waveguide for VLF radio waves, *J. Geophys. Res.*, 73, 3537, 1968.
- Wait, *Electromagnetic Waves in Stratified Media*, Pergamon Press, Oxford, 1970.
- Wait, J. R., EM scattering from a vertical column of ionization in the Earth-ionosphere waveguide, *IEEE Trans. Ant. Prop.*, 39, 1051, 1991.
- Wait, J. R., and K. P. Spies, Characteristics of the Earth-ionosphere waveguide for VLF radio waves, *Tech. Note 300*, National Bureau of Standards, Washington, D.C., 1964.
- Wait, J. R., and K. P. Spies, On the calculation of mode conversion at a graded height change in the Earth-ionosphere waveguide at VLF, *Radio Sci.*, 3, 787, 1968.
- Watt, A. D., *VLF Radio Engineering*, Pergamon Press, New York, 1967.
- Wolf, T. G., Remote sensing of ionospheric effects associated with lightning using very low frequency radio signals, Ph.D. dissertation, Stanford Univ., Stanford, Calif., 1990.
- Wolf, T.G., and U. S. Inan, Path-dependent properties of subionospheric VLF amplitude and phase perturbations associated with lightning, *J. Geophys. Res.*, 95, 20997, 1990.
- Yip, W.-Y., U. S. Inan, and R. E. Orville, On the spatial relationship between lightning discharges and propagation paths of perturbed subionospheric VLF/LF signals, *J. Geophys. Res.*, 96, 249, 1991.